The Role of Transport Phenomena in Whispering Gallery Mode Optical Biosensor Performance

Thesis by

Jason Gamba

In Partial Fulfillment of the Requirements

for the Degree of

Doctor of Philosophy

California Institute of Technology

Pasadena, California

2012

(Defended June 3, 2011)

For Ashley, my wife and friend. Everything changed when I met you.

Acknowledgements

The fact that a single name appears on the title page of a dissertation can be quite misleading. Neither this document, nor the research behind it, could have been completed without the help of a great number of people.

I would first like to thank my advisor, Professor Rick Flagan, who has given me the opportunity to work on a project I truly enjoy. I came to him at the end of my third year of graduate school seeking help from the Executive Officer of Chemical Engineering with finding a new research home on campus. I was looking for a project in a research lab that could support me while I completely rebooted my graduate career, and hoped Professor Flagan could advise me on how to go about my search. After listening to me describe my situation for nearly an hour, he politely asked if I would be interested in hearing about a project available in his own group involving an extraordinary optical biosensor. Within days I was a Flagan Lab member, eager to return to my roots as a chemical engineer by applying the field's core disciplines to the analysis of what was essentially a physicst's toy. Professor Flagan has taught me a great deal about instrument development and validation, and working in his lab has been an excellent education as a researcher.

I am also very grateful to Professor Andrea Armani, who has been a valuable mentor and friend to me since we began working together in 2008. It was her work as a Clare Boothe Luce Postdoctoral Fellow that began the collaboration between the Flagan, Vahala, and Fraser laboratories at Caltech, of which I have been a part. I was fortunate enough to learn this field from her, and benefit from the extraordinary care and patience she put into developing the procedures she used for her experiments. Even after Professor Armani accepted her faculty position at the University of Southern California, she continued to offer her time to answer my (seemingly endless) questions. I cannot express how helpful this was for a researcher trying to learn a field outside his expertise. Working with her and getting to know her has truly been one of the most rewarding pieces of my graduate career.

I would like to thank Professors Scott Fraser and Mark Davis as well for all of their helpful suggestions and guidance as members of my thesis committee. Of course, my work would not have been possible at all if not for the much-appreciated funding from the Jacobs Institute for Molecular Engineering for Medicine at the California Institute of Technology.

I have also been fortunate to work alongside a wonderful group of researchers in the Flagan/Seinfeld Laboratory. The person who has most affected my own research is Xerxes Lopez-Yglesias. He is a resource of incalculable value to the group, with nearly everyone relying on his broad expertise at one point or another during their tenure. He and I conducted a thorough analysis of the physics involved in sensing a single biomolecule with a whispering gallery mode sensor, debating the value of previous methods and the interpretation of reference texts for hours on end. This intense academic endeavor led us to two main conclusions: (i) that theoretical modeling comes entirely down to how you justify the shortcuts you took in order to preserve your sanity, and (ii) that the selection of Pasadena dining establishments open at 3 am is sadly limited.

Andy Downard is another fine groupmate to whom I am indebted. In addition to being a good friend, Andy was of particular help with my efforts to model the fluid flow around sensors. He contributed even more to the daily operations of the lab by generously providing organizational advice and encouraging a multidisciplinary spirit that is too often absent in research environments. Our research group often posed unique challenges, as everyone must quickly develop a broad range of abilities in order to make any progress. I am grateful, however, to *all* the members of the Flagan and Seinfeld groups for creating a cooperative and friendly atmosphere, which should never be taken for granted. You all conduct your research (and yourselves) with class in the face of overwhelming pressure to succeed at any cost.

I would also like to thank two outstanding collaborators, Jacob Sendowksi and Naresh Satyan, for their friendship, help, and patience during our work to integrate a tunable laser source of their creation into the nascent sensor apparatus described in the chapters that follow here. Along with the help of other members of the Yariv Laboratory in Applied Physics and Electrical Engingeering, especially Scott Steger and Arseny Vasilyev, we began what I hope is a long and productive research partnership for our groups. From the many, many hours I spent working with Jacob and Naresh, I can say that both represent the finest that Caltech has to offer. They are excellent scientists and just truly fun people to be around, both of which only made the grueling frustration of troubleshooting a relatively untested experimental setup that much more pleasant.

Though they get too little credit for the impact they have on student life and graduate research, the various staff at Caltech also deserve a great deal of gratitude. Chemical Engineering administrative assistants like Kathy Bubash, Laura King, Anne Hormann, Marcy Fowler, Martha Hepworth, Karen Baumgartner, and Yvette Grant play a huge role in making sure students have access to their advisors and that the academic machinery continues to run smoothly for everyone. Additionally, a great systems administrator like Suresh Gupta is pivotal in a research environement like Caltech where computation and data storage/transfer are so important. Technical staff, including machinists like Mike Roy, Steve Olsen, and Mike Vondrus as well as glassblowers like Rick Gerhart, are also valuable resources that allow students to push the envelope of their field by creating new equipment and techniques. It also helps that they are all so friendly, welcoming, and generous with their time. I would like to thank all of these fine Caltech staff members for all of the tasks, large and small, they have helped me with since I started here. I would especially like to thank Mike Roy for teaching me so much about machining and for being such a great friend to me through all of my frustrations. He is a bright and inquisitive man who perfectly embodies the spirit of Caltech's ingenuity and curiosity.

I also want to point out the contributions that another staff member, Dr. Mike Vicic, has made to my graduate career. He is a truly gifted educator who cares deeply about helping his students learn *and remember* as much of the mountain of information that the Chemical Engineering curriculum presents to them as possible. I TAed courses administered by Mike three times, and I may have learned more TAing his undergraduate courses than I did during my own undergraduate career. I want to thank him for all of the conversations and guidance he has given me as my friend and unofficial mentor. I cannot overstate his value to the Chemistry and Chemical Engineering Division, or to the many students that get the chance to interact with him.

One of the most important reasons I chose to come to Caltech for graduate school was the altogether wonderful people that I would get to study with in Chemical Engineering. Though the majority of them graduated (well) before me, I consider myself fortunate to have worked with such a fine group as them. I am truly lucky to have met and learned from people like Brendan Mack, Nick Brunelli, Yoshie Narui, Chris Alabi, Jim Van Deventer, Chase Beisel, and John McKeen. Thank you all for making Caltech such a wonderful place to be and learn.

These and many other friends enriched my life and helped me make it through the more difficult times in graduate school. Matt Jacob-Mitos and I left Rensselaer Polytechnic Institute as best friends, which is probably why he followed me out to the West Coast for school (albeit to a different university). I shudder to put this in writing lest he never let me live it down, but he is one of the brightest people I have ever met and he makes things fun. I owe him a great deal for supporting and continually encouraging my pursuit of a Ph.D. Additionally, Charlotte Mack has been a constant source of fun since I met her many years ago. She is a voice of comfort and inspiration, and her love of life and learning is contagious. I am so very grateful to her and her husband, Brendan, for all of their support through graduate school, my ongoing job search, and life in general. Other brilliant and wonderful friends like Sara Broadhead, Rick Tabor, Chris and Jessica Hansen, and Jackie Kopcsak have all helped me keep a healthy perspective by letting me think and talk about something other than science during all of the fun times we have gotten to spend together. To all of these great friends I give my love, admiration, and thanks.

I want to thank my wonderful family for their extraordinary support. My parents, David and Eileen, have always fostered my curiosity and joy for learning, but their love and encouragement has meant a great deal to me. They have worked so hard to make sure every possible educational opportunity was available to their children, from pre-kindergarten to this day. They have always given me the freedom to pursue my interests, even when that carried me 3000 miles away for graduate school. I am truly fortunate to have such caring and giving parents. I could not have accomplished any of this without their sacrifice and love. I want to thank them for all of this, and for raising me a Red Sox fan.

My entire family has helped me get to this point in my life. I want to thank, in particular, all of my grandparents for being such wonderful examples of how people should treat each other and approach their lives and their work. They are and were passionate individuals, and I love them very much.

Thank you, also, to my brother, David, for always backing me up and helping me to persevere through his encouragement and love. You are the best big brother and friend anybody could have.

Finally, I want to thank my wonderful wife, Ashley. Everything in my life improved when I met you. There is no way I can thank you enough for the sacrifices you have made or the lengths to which you have gone to help me on this (regrettably) long road to graduation. You are an extraordinary woman who volunteered to live the lavish life of a graduate student's wife. I still do not understand what saintly feat I must have accomplished to deserve you, but I am grateful everyday because chance sat me next to you on that airplane. Thank you so very much.

Abstract

Whispering gallery mode (WGM) optical resonator sensors have emerged as promising tools for label-free detection of biomolecules in solution. These devices have even demonstrated single-molecule limits of detection in complex biological fluids. This extraordinary sensitivity makes them ideal for low-concentration analytical and diagnostic measurements, but a great deal of work must be done toward understanding and optimizing their performance before they are capable of reliable quantitative measurents. The present work explores the physical processes behind this extreme sensitivity and how to best take advantage of them for practical applications of this technology.

I begin by examining the nature of the interaction between the intense electromagnetic fields that build up in the optical biosensor and the biomolecules that bind to its surface. This work addresses the need for a coherent and thorough physical model that can be used to predict sensor behavior for a range of experimenal parameters. While this knowledge will prove critical for the development of this technology, it has also shone a light on nonlinear thermo-optical and optical phenomena that these devices are uniquely suited to probing.

The surprisingly rapid transient response of toroidal WGM biosensors despite sub-femtomolar analyte concentrations is also addressed. The development of asymmetric boundary layers around these devices under flow is revealed to enhance the capture rate of proteins from solution compared to the spherical sensors used previously. These lessons will guide the design of flow systems to minimize measurement time and consumption of precious sample, a key factor in any medically relevant assay.

Finally, experimental results suggesting that WGM biosensors could be used to improve the quantitative detection of small-molecule biomarkers in exhaled breath condensate demonstrate how their exceptional sensitivity and transient response can enable the use of this noninvasive method to probe respiratory distress.

WGM bioensors are unlike any other analytical tool, and the work presented here focuses on answering engineering questions surrounding their performance and potential.

Contents

List of Figures

List of Tables

Chapter 1

Introduction

1.1 History and Context

The present work represents the first foray into the field of whispering gallery mode sensing, or any biosensing technology, on the part of the Flagan Research Group. During her graduate and post-doctoral research, Dr. Andrea Armani began applying the microtoroidal resonators first created in the Vahala laboratory in Applied Physics to chemical and biological sensing. When the interpretation of these experiments demanded an expertise in biology and heat transfer, Professors Scott Fraser and Rick Flagan were consulted and a collaboration was born that later produced a publication in the journal *Science* [1].

I joined the Flagan Group in January 2008 after it became necessary to find a new laboratory and research project to finish my doctoral work. From January until August I had the privilege to learn from Dr. Armani the methods and theory that she developed in her work with microtoroidal whispering gallery mode (WGM) biosensors. She ordered components and oversaw my construction of a new experimental setup to mimic the one she used in the Vahala laboratory and another being built concurrently in the Fraser laboratory. I was trained on the finer points of pulling tapered optical fiber waveguides, using a CO_2 laser to reflow silica disks into toroids, coupling light into the toroidal cavity, and, finally, performing a sensing experiment in an acqueous environment.

My intentions when I joined the Flagan Group were to bring a chemical engineer's perspective to the evaluation of the nascent WGM biosensor. The single-molecule sensitivity observed by Dr. Armani begged more questions than it answered—especially when it comes to evaluating the future of this technology. How the sensitivity scales with molecular size, laser scanning rate, wavelength, and fluid flow rate all matter when optimizing operating conditions. Additionally, it becomes important to determine the advantages and disadvantages of single-molecule sensitivity when a slightly worse sensitivity is still orders of magnitude better than alternative technologies but does not require as much effort for data analysis.

There was doubt expressed concerning the results in the *Science* paper beginning shortly after its publication, but it did not develop until a recent publication attempted to reconcile the proposed physical model with current models and to address the extraordinary sensitivity. While no evidence has been presented to doubt the validity of the experimental observations, it became clear that fundamental questions remain unanswered concerning the basic interactions between the electromagnetic fields in the resonator and the biomolecules that adsorb to the surface. It was at this point that I began the work in Chapter 4 concerning a full description of the heat transfer that would be a part of the thermo-optical model of WGM sensor performance. My progress was limited by my lack of familiarirty with the theory concerning electomagnetic fields and waves, and I began collaborating with labmate Xerxes Lopez-Yglesias to form a complete model that would allow us to compare Dr. Armani's results to a more thorough theoretical prediction. The problem turned out to be monstrously complex, and so we instead crafted a roadmap to guide future work that itself provided new insight and corrected mistakes propagated in the previous literature.

I continued running WGM biosensing experiments in an effort to demonstrate how these devices could be used to detect pollen fragments that play a role in asthma exacerbation. Unfortunately that project was sidetracked by poor luck; the New Focus Velocity$^{\text{TM}}$tunable laser source at the heart of the WGM sensing experiment was broken when we received it and, after being returned to us 6 months later, immediately began to degrade in performance and cause artifacts in the data until it was no longer functional. I turned my focus back to modeling the effects of mass transport on WGM biosensor performance, yielding the work in Chapter 5. This work has only begun addressing the many interesting problems involved when extraordinarily intense light is present during an equilibrium surface reaction.

The present work is intended to serve as a foundation on which future research into the many physical processes involved in WGM biosensing may build. My original research plans involved expanding the applications for these devices; however, that changed when when I saw opportunities to improve our understanding of WGM biosensors behavior and have a greater impact on the field by modeling the transport phenomena that, until now, have received little attention. This work ultimately addresses fundamental questions that would otherwise hinder the evolution of this technology toward a viable instrument, and, in doing so, presents methods that may be used to address some of the remaining challenges.

1.2 Thesis Structure

This thesis is arranged to serve as a primer for those who hope to conduct WGM biosensing experiments in the future. Chapter 2 introduces the field of biosensors and, more generally, the specific molecular recognition events that go into a successful bioassay. I describe sample preparation and useful surface chemistries, and review some of the current label-free biosensing technologies that one might encounter in the literature. Chapter 3 continues the introduction by focusing on WGM resontors and sensors. Topics in this chapter include fabricating, characterizing, comparing, and modeling these devices.

Chapter 4 explores the significance of fluid flow and mass transfer on the transient data observed using a variety of WGM biosensor geometries. Specifically, that work explores how the asymmetric concentration boundary layers that form around the sensor in the WGM biosensor flow cell enhance the transient early portion of the transient response, giving rise to the surprisingly fast binding time observed by Dr. Armani that had, until now, puzzled those who work with these devices. Chapter 5 includes the work done in collaboration with Xerxes Lopez-Yglesias to model the relevant physical processes involved in WGM sensing of single molecules. As mentioned above, it is a guide for those interested in modeling the entire, complicated process including nonlinear thermal and optical effects. In Chapter 6, I describe experimental work that seeks to advance WGM biosensors toward medically relevant applications for which they pose a unique solution. In particular, I detect a small molecule biomarker for oxidative stress in the respiratory system that can be found at low concentrations in exhaled breath condensate. Establishing that the WGM biosensor outperforms other analytical techniques for this measurement may make help expand into lower-concentration regimes the working library of biomarkers available for use in diagnostic medicine.

Finally, Chapter 7 concludes this document by reviewing findings and discussing the many interesting places this research may lead. I truly hope that those who read this document see the promise in this type of biosensor technology, but also realize that a great deal of work must be done before it can be used in practical analytical or diagnostic applications.

Chapter 2

Biosensors

2.1 Overview

The recent trend toward integrated and automated instruments based on bioassays has had an extraordinary impact on the speed and efficiency with which analytical and diagnostic measurements can be made. Bioassays are methods by which one may determine the absolute or relative concentration of a specific biomolecule in a sample; the target molecule is called the *analyte*. The researcher attempting to measure how well a new drug works, the medical laboratory technician testing a patient's blood for disease, and even the biology graduate student manipulating genes in an effort to understand a fundamental cellular function relies on a bioassay to get his or her answer.

Each bioassay is characterized by a method that translates the quantity of analyte present in the sample into a measureable signal. Any device that can uses biomolecular interactions at its surface to report this signal while rejecting unintended, nonspecific signal is called a *biosensor*. It is indeed discouraging to observe in the literature the variety of meanings given to these words; the definitions chosen here are based on those used by the International Union of Pure and Applied Chemistry (IUPAC) [4].

My work focuses on one variety of biosensor–the whispering gallery mode (WGM) optical resonator. I describe the details of this type of device, as well as its fabrication, in Chapter 3. WGM optical resonators have only been used for biosensing applications for less than a decade [5, 6] and the performance and limitations of the technology are still being characterized and debated. It is clear already, however, that these devices exhibit extraordinary sensitivity and show great promise as a future analytical or diagnostic instrument. This process by which a technology is built into an integrated instrument is slow and laborious, however, and requires an understanding of the many factors that contribute to its performance. The results presented in Chapters 4 through 6 aim to advance this understanding and, hopefully, inform the development of an instrument.

This chapter describes the features common to all biosensors and introduces a range of example technologies: (i) a method for detecting biomolecules, (ii) a method for ensuring only specific detection, and (iii) a method for introducing sample. With these in mind, I introduce the biosensor technologies in use today and explore their advantages and disadvantages. Finally, I discuss what researchers in the WGM biosensing field can learn from these alternatives, and what challenges must be addressed in the ongoing effort to develop a WGM biosensor instrument.

2.2 Specific Detection

A key function of a biosensor is the ability to either ignore signal from molecules other than the analyte or to actively stifle all interactions other than those with the species of interest. Though the latter is the far easier option in nearly all cases, it would be misleading to suggest that either option is, by any means, simple. To reject all interactions other than those with the analyte, the surface of the sensor may be functionalized with a targeting species that will interact only with the analyte.

The interaction between two species that have a particularly high and exclusive affinity for one another is called *specific binding*, and it is due to a variety of factors. It is often depicted as a simple geometric match, with one molecule possessing a "binding pocket" shaped perfectly for its ligand. While this is often the case, a more complete model must take into account the balance between attractive and repulsive forces as well as the overall energy of the bound and unbound systems. The more common type of interaction is called *nonspecific binding*, and it implies only that there is an affinity between two species.

The best example of nonspecific binding is highlighted by the work of Leo Vroman, who spent much of his career as a hematologist studying how proteins in blood plasma adsorb to surfaces. There is no specific interaction between a protein, such as fibrinogen, and a surface like glass, but it adorbs to a microscope slide nevertheless because the protein is not rigid. Its tertiary structure bends and stretches, sampling a range of conformations. The hydrophobic residues that are typically hidden in the center of the protein to limit their exposure to the polar water molecules in the solvent can induce a restructuring with two effects: (i) these hydrophobic residues can be pressed against the surface (typically less polar than water) to further decrease the strength of their interaction with the solvent and (ii) more of the hydrophilic residues can interact with water due to the higher surface area-to-volume ratio of the pancake-like bound protein [7]. Any generic interaction, including a pure Coulombic one that might draw all positively or all negatively charged species to the sensor surface, can be considered non-specific. Rejecting all signals due to the many possible nonspecific binding methods is, indeed, a challenge.

A popular method to reject this type of undesired adsorption in favor of specific interactions is to simply coat the sensor surface with the targeting species, such that there is no remaining space for other species to occupy. Attaining such high surface coverage is very difficult because of steric effects. An alternative approach is to fill the space between targeting species molecules with a material that actively rejects nonspecific adsorption, e.g., polyethylene glycol (PEG) [8, 9]. It is believed that the high density of hydroxyl groups in PEG produce a structured and stable water layer that would be disrupted (a significant enthalpic penalty) by nonspecific adsorption by other species. A variety of surface treatments have been developed toward a similar purpose [10]. Several have even been incorporated into a molecular architecture that includes the targeting agent [11, 12, 13].

Reversible binding of the analyte to the targeting species can be described using a simple Langmuir kinetic model where [A] is the concentration of analyte, [T] is the surface concentration of unbound targeting species, [C] is the surface concentration of the bound complex, and $[\mathrm{T}]_0$ is the total concentration fo the targeting species. The adsorption/desorption reaction

$$\mathrm{A} + \mathrm{T} \rightleftharpoons \mathrm{C}$$

proceeds at a forward (adsorption) rate,

$$\text{rate}_{ads} = k_{ads}[\text{A}][\text{T}], \tag{2.1}$$

and a reverse (desorption) rate,

$$\text{rate}_{des} = k_{des}[\text{C}]. \tag{2.2}$$

The rate of change of the free analyte concentration is

$$\frac{d[\text{A}]}{dt} = -k_{ads}[\text{A}][\text{T}] + k_{des}[\text{C}]. \tag{2.3}$$

At equilibrium, $\frac{d[\text{A}]}{dt} = 0$, and

$$\frac{k_{des}}{k_{ads}} = K_D = \frac{[\text{A}][\text{T}]}{[\text{C}]} \tag{2.4}$$

is the equilibrium dissociation constant. The total concentration of tageting sites [T] is conserves, so the concentration of available sites is $[\text{T}] = [\text{T}]_0 - [\text{C}]$. Therefore, the bound analyte concentration varies with time as

$$\frac{d[\text{C}]}{dt} = k_{ads}[\text{A}]([\text{T}]_0 - [\text{C}]) - k_{des}[\text{C}], \tag{2.5}$$

and asymptotically approaches the steady-state (or “equilibrium") value of

$$[\text{C}]_{\text{eq}} = \frac{[\text{A}][\text{T}]_0}{\text{K}_\text{D} + [\text{A}]}. \tag{2.6}$$

It is simple to show that half of all binding sites are occupied when $[\text{A}]=K_D$. The sensor response as a function of [A] enables measurement of K_D as illustrated in Figure 2.1 for the protein Interleukin-2 [14].

It is worth pointing out that interaction between an analyte and its targeting species can be a delicate function of experimental conditions. Not only is the affinity (K_D) a function of temperature due to the effect of thermal fluctations (or lack thereof) on the probability that two species will be able to bind to one

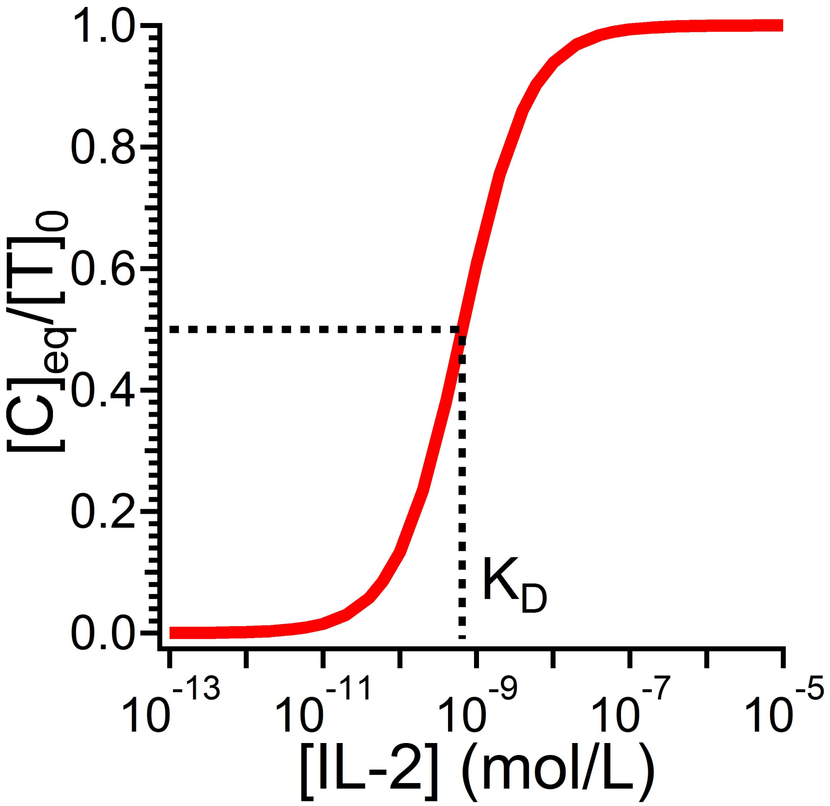

Figure 2.1: An equilibrium binding curve for Interleukin-2 with its T Lymphocyte receptor according to Eq. (2.6). Note the sigmoidal shape whose slope approaches zero in the limit of both high and low analyte concentrations. At low [A], the large relative changes in concetration are still too small in terms of total analyte molocules bound. In contrast, the sensor surface is saturated at high [A] and changes in concentration make little affect little change in sensor signal. K_D is marked at 6.5×10^{-10} M.

another, but the very structure of the species involved often changes with pH, salt concentration, ambient light, and temperature. One should always keep in mind when using biomolecules that they (for the most part) did not evolve for the sole purpose of a bioassay in a research laboratory. They can be unstable, fickle, and uncooperative when it comes to varying experimental conditions.

Targeting Species

The challenge of finding a species to serve as the targeting agent on a biosensor surface has, thankfully, been addressed by the slow and methodical process of evolution. Biomolecules comprise a vast array of species that exist within organisms, including nucleic acids, proteins, and fatty acids. Each species serves a particular purpose in an organism, and must interact with other biomolecules in order to accomplish it. The problem of finding a targeting species for a given analyte often comes down to finding the complimentary molecule that evolved to interact with it. Consider nucleic acids, which consist of two chains of repeated units called nucleotides. Deoxyribonucleic acids (DNAs) feature the well-known double helix structure in which the two opposing chains form bonds with one another much like the steps in a ladder. There are only four varieties of nucleotides in DNA; the double helix cannot form unless each nucleotide in the sequence is paired with its one complimentary nucleotide on the the opposing strand. Immobilizing a short, single strand of DNA on the surface of the sensor allows only complimentary strands to bind on the device surface with appreciable stability [15]. Much like with a long zipper with only a single tooth unzipped, however, a long target strand could possibly bind a slightly mismatched sequence because the energetic favorability of the bonds that form outweighs the entropic penalty of immobilization.

The principle of complimentary nucleic acid sequences extends beyond this simple example, though. Aptamers can be used where biology has not produced a tailor-made targeting species, even though it provides the architecture to do so. These oligonucleotides are designed with a sequence that will envelop and bind to a particular species [16, 17, 18]. Methods have been established by which a researcher can evolve an aptamer for an arbitrary analyte [19]. Their capability to encode adaptable molecular recognition has even made them appealing tools for gene-regulation platforms [20]. Though the binding affinitiy of aptamers for their analytes varies greatly [21], they can attain K_D values as low as 1 nM.

Perhaps the most popular targeting species for biosensing applications is the antibody. These proteins, also called immunoglobulins, are a part of the body's immune response and feature K_D values of $0.1-100$ nM for their antigens. They consist of four polypeptide chains—two heavy chains and two light chains—connected to one another via sulfide bonds (see Fig. 2.2). As with all proteins, the variations among antibodies that allow analyte-specific interactions are due to the order in which the 20 available amino acids are arranged, and the tertiary structure to which this sequence leads. Figure 2.2 shows the coarse anatomy of an antibody, which features a stem (the "$\mathrm{F_C}$" region) and two arms (the "$\mathrm{F_{AB}}$" regions). At the end of each $\mathrm{F_{AB}}$ region is a complementarity-determining region (CDR) that accounts for the source of variation from one antibody

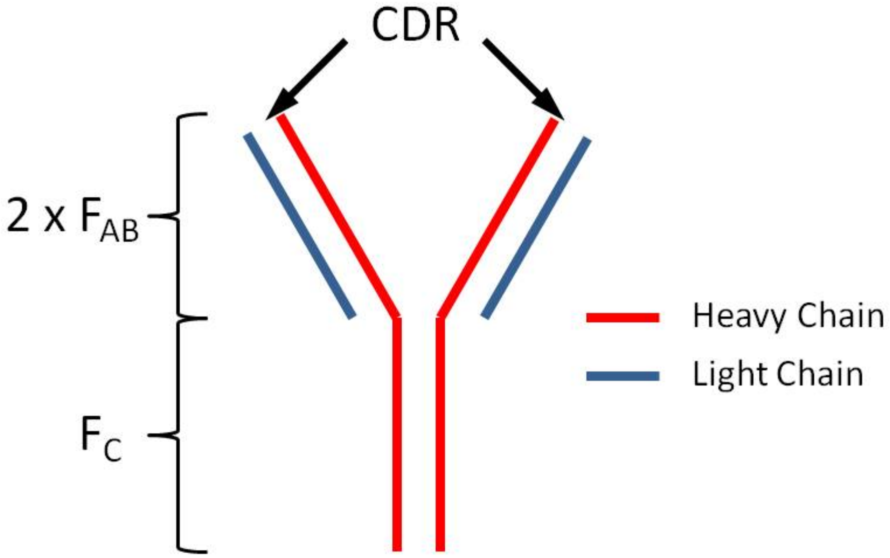

Figure 2.2: This antibody features four polypeptides: two heavy chain (red) and two light chain (blue). Note also the "stem-and-arms" configuration, with one F_C and two F_{AB} regions. The two complementarity-determining regions (CDRs), where analyte binding occurs, are noted at the end of the two F_{AB} regions.

to another and binds to the analyte.

Antibodies exist in *monoclonal* and *polyclonal* varieties. The former refers to antibodies produced when an organism seeks to increase production of a single variant of the antibody by cloning cells that produce only that one type, while the latter refers to a spectrum of antibody variants from a group of cells from different lines. For this reason, monoclonal antibodies are often preferred for sensing applications due to their uniform properties.

Sensor Functionalization Methods

The task of coating a surface with the targeting species of choice is called functionalization. There is a dichotomy among the methods for this purpose: covalent or non-covalent functionalization. The former benefits from stability and the guarantee that your targeting species surface concentration remains constant during an experiment, which makes it possible to use species conservation equations to determine the reaction kinetics of binding and/or desorption. However, covalent functionalization alters the surface chemistry of the sensor and could possibly affect its performance. Non-covalent functionalization methods are less permanent, but often simpler to implement and less likely to interfere with sensor function. Nonetheless, a covalent method is desirable because it gives control over the orientation of the targeting species not often found in covalent functionalization methods.

Directly attaching the targeting species to the sensor surface, although sometimes possible, is usually unwise because newly formed chemical linkages can affect the molecule's affinity for the analyte. A bifunctional linker molecule is commonly used, one end of which has a moiety to anchor to the sensor surface, and the other has a carefully chosen functional group chosen to react with the targeting species without damaging it. For the gold surface presented by surface plasmon resonance chips (see Section 2.5 below) this linker is often an alkane with a thiol anchor group to react with the gold surface; a maleimide group at the other end of the linker reacts with available cysteine residues on the antibody [22]. The type of coating that results is often referred to as a self-assembling monolayer (SAM) [23].

For the silica WGM biosensor we deal with here, the linker can be an alkane similar to that for a gold surface, replacing the thiol with a trichloro, trimethoxy, or triethoxy silane group that reacts well with acid-treated silica. This type of linker is particularly useful because of the high vapor pressure of the silane, which makes it possible to bind the linker to the silica by vapor deposition, thereby avoiding the damage to and contamination of the ultrasmooth surface of WGM sensors that often accompanies the use of a more harsh liquid-phase environment for functionalization [24]. The bioconjugation chemistry literature provides details of these and other covalent functionalization techniques [12, 13, 11, 25, 26].

Non-covalent techniques rely on physisorption of an anchor molecule, to which either a linker or the targeting species itself may be conjugated. This physisorption, often the result of hydrophobicity of the surface and the anchor molecule, can be exploited to great effect using polymer layers [27, 28], but is not orientation-specific. One elegant, albeit unstable, example is the use of Protein G [29], a protein capable of non-specifically adsorbing to some bare surfaces and maintining its function of binding to the $\mathrm{F_C}$ region of any IgG antibody. Figure 2.3 depicts a Protein G-anchored functionalization architecture, including the technique's two main drawbacks: (i) local surface density variations due to the nature of nonspecific adsorption, and (ii) the variability in orientation of the antibodies immobilized by the Protein G molecules.

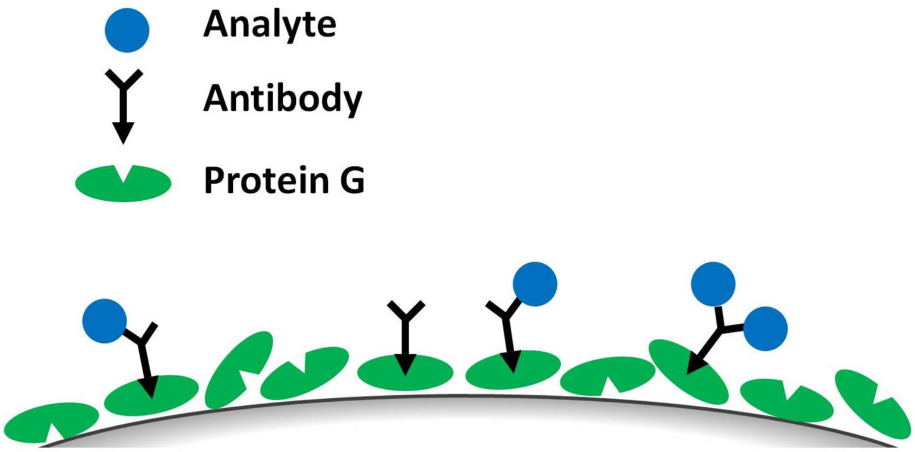

Figure 2.3: The non-covalent functioanlization of a biosensor surface via the non-specific adsorption of Protein G (green) and antibody (black). Exposure to analyte (blue) will lead to binding according to the equilbrium expression in Eqs. (2.1)–(2.4). Note the random orientation of the Protein G molecules as well as the fact that not all such molecules are occcupied by an antibody.

The singular binding orientation available to antibodies that interact with Protein G is an advantage over other surface functionalization methods, some of which result in the highly oriented anchor molecule arrangement but randomly oriented targeting molecules. Nonetheless, sensors using non-covalent functionlization architectures can be unreliable due to the absence of a permanent bond. Fluctuations in solution conditions, temperature, or even just oxidation over time can erode the uniformity of the non-covalent layer.

The covalent and non-covalent methods overlap with the use of the well-known complexation reaction between biotin and tetravalent protein avidin. The former is a small molecule known also as vitamin B7, while the latter is a protein commonly found in chicken and other bird eggs. They bind with a $K_D \sim 10^{-15}$ M, making theirs an extraordinarily strong bond that is, at least technically, non-covalent. This pair is an excellent tool for evaluating and characterizing sensors and other assays because it removes all doubt as to whether the species bound to an appreciable extent. Additionally, the utility of biotin and avidin lies in their ability to be conjugated to other species while maintaining their affinity. As such, enzymes, antibodies, and other proteins are available commercially with conjugated biotin or streptavidin. Methods have been developed to exploit this pair for sensor functionalization to impressive ends [24].

2.3 Sample Delivery Methods

As we discuss in Chapter 5, the methods used to introduce sample to a biosensor can significantly affect the data collected by a biosensor. At the very least, a sample delivery system must ensure that the sensor is efficiently exposed to the sample. Two practical constraints are added when working with valuable or rare sample, a common occurrence in medical diagnostics and analytical biochemistry. The first of these is that the delivery system conserve sample as much as possible by limiting the volume required for a measurement. This includes all flow paths and reaction chambers. The second constraint is that the delivery system must minimize the time necessary for a measurement. This second constraint is related to the first in that both aim to improve sample economy, and they represent different tactics for accomplishing this goal.

Combining these two concepts would suggest a small-volume biosensor flow cell as the optimal delivery system. Diffusion alone is an inefficient delivery method for the analyte to the micro- and nanoscale sensors we discuss below if the flow cell is considerable larger than the sensor. Microfluidic devices are a practical solution because they can be repeatably made from conveniently adaptable materials (e.g., polydimethylsiloxane, also called PDMS) with small overall dimensions and micron-scale precision using soft lithography techniques. Their behavior is well characterized [30, 31], partly due to the fact that flow in such small channels with width and height typically less than 500 μm is always laminar. To enter the turbulent flow regime, which is far more difficult to describe analytically, would require impossibly high fluid velocities. In light of the laminar restrictions, mixing of two streams in a microfluidic device is a challenging but realizable feat [32].

Microfluidic devices suffer the drawback of cumbersome pumping systems, high pressures due to the small flow channels, and what can be a slow, serial fabrication procedure. Other, simpler options are available, although they usually do not isolate the system from ambient changes as well as microfluidic devices. For example, extremely sensitive measurements have been made using an open flow cell comprising a substrate for the bottom of the cell, a glass coverslip as the top, and a single wall to connect the two. One or many flow inlets and outlets may be inserted in the absence of walls, and the fluid (typically aqueous) is held in place by capillary forces. The tempation to use a material that avoids the depleting effects nonspecific adsorption onto the flow cell walls, specifically Teflon, is unwise due to the hydrophobicity of that material

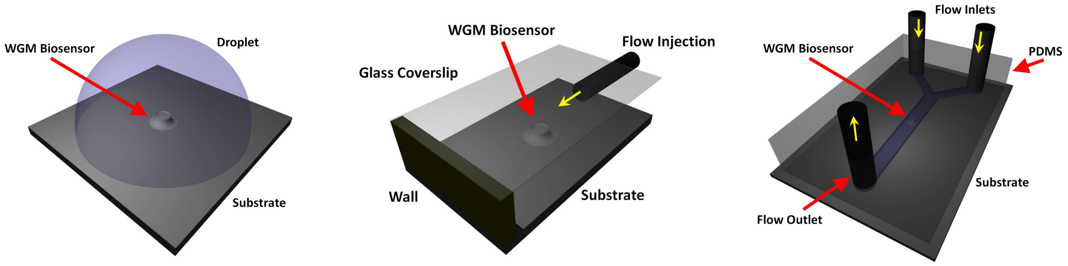

(a) Droplet (b) Open Flow Cell (c) Microfluidic Device

Figure 2.4: Methods for delivering sample to a biosensor. (a) The simple batch method, wherein a droplet of solution is placed onto a planar sensor and diffusion delivers sample to the device surface. (b) The open flow cell with flow injection, featuring a substrate and glass coverslip to form the top and bottom. Surface tension prevents the water from draining, requiring that either the top and bottom surfaces be sufficiently wettable *or* the gap sufficiently small. (c) The microfluidic flow cell, a subset of the closed flow cells. These devices are typically made using soft lithography techniques, and their microscale features ensure laminar flow and very little mixing.

and its inability to trap water in the cell. Silica and stainless steel are suitably wettable, however. This sample delivery system, as well as others, is depticted in Figure 2.4. The simplest sample delivery system is the addition of a droplet to engulf a substrate-bound microscale biosensor [33]. The droplet will experience increased evaporation compared to enclosed flow cells, however, and the resulting change in concentration and temperature would likely complicate the interpretation of experimental results.

2.4 Biosensor Performance Metrics

In order to appreciate the strengths and weaknesses of a biosensing technology, one must have a way of comparing it to other technologies. An ideal biosensor would of course be inexpensive, simple to use, and effective. Though cost and ease of use depend greatly on instrument-level design features, one can often get an idea of whether these factors are likely to pose problems in the future. The effectiveness is the most useful tool for comparison of technologies in their developmental stages, however. I will, therefore, focus on the primary figures of merit used in the biosensing community when evaluating device effectiveness: limit of detection (LOD) and dynamic range (DR).

Biosensors may be designed to produce two types of data—transient ("kinetic") data, and endpoint ("equilibrium") data. Transient data shows how the sensor response changes over time and, with careful considerations of mass transfer, can be used to measure the kinetic characteristics of the surface binding reaction (Eqs. (2.1)-(2.4)). Endpoint data records a single point for each experiment to reflect the sensor response after a certain amount of time or after a particular event has occurred. For the most part, this event is when the system reaches a steady-state, which reflects an equilibrium or saturation in the surface reaction occurring at the surface of the biosensor.

The LOD is an intuitive quantity that describes the lowest concentraton at which a biosensor can produce a signal clearly distinguishable from the noise in the measurement. For present purposes, a clearly distinguishable signal is one that has a signal-to-noise ratio (SNR) greater than 1. A SNR value less than 1 implies that the noise overwhelms the magnitude of the signal. A biosensor with a SNR 1 at a concentration of 10 fM can quantatively measure the concentration of sample down to this value, although variability from experiment to experiment may push the LOD higher. For this reason, one must always use multiple trials to demonstrate the true limit of detection for a sensor. Both transient and endpoint data are used to determine the LOD.

The dynamic range of a sensor describes the range of concentrations over which the device can reliably report a concentration perturbation. A plot of the endpoint sensor response (see Figure 2.1) can be used to determine the dynamic range of a sensor with signal X by examining $\frac{dX}{d[\mathrm{A}]}$, an expression formally referred to as the *sensitivity.* The sensor is limited at low [A] by its LOD; at high concentrations the sensor surface may be saturated so that no binding sites remain for adsorption of analyte. In both of these limits, $\left|\frac{dX}{d[\mathrm{A}]}\right| \ll 1$, and even large perturbations in [A] cannot be resolved by the sensor. The signal can change greatly due to such a perturbation if $[\mathrm{A}] \approx K_D$, however. The dynamic range is defined by the concetration window from $[\mathrm{A}]_{lower}$ to $[\mathrm{A}]_{upper}$ inside which a perturbation $\delta[\mathrm{A}]$ produces a sensor response that is distinguishable above the noise σ_{noise}, or where $\delta[\mathrm{A}]\left|\frac{dX}{d[\mathrm{A}]}\right| > \sigma_{noise}$.

An additional consideration is sample economy. As previously mentioned, the sample delivery method often controls sample size, but the physical dimensions of the sensor also play an important role. Small sensors that minimize sample volume are generally preferred in practical applications like medical diagnostics. As

I metion above (see Section 2.3), this is often limited by the sample delivery method, but the actual size of the sensor also plays an important role. Smaller sensors that require less sample are always preferred in practical applications like medical diagnostics. Just imagine a doctor telling you he or she has a test that can tell with 100% certainty whether you have cancer, but that it requires 2 L of your blood. Therefore, it is wise to keep in mind both the size of the device and its ease of integration into a low-volume flow cell when evaluating a biosensor technology.

2.5 Biosensor Technologies

The diverse field of biosensors can be most conveniently organized according to the physical process by which the device translates the adsorption of material into a measureable signal. According to this scheme, there are four predominant categories of sensor: electrical, mechanical, magnetic, and optical biosensors. The discussion that follows will highlight some of the more successful and promising implementations of these technologies. Sensing technologies may be further divided between those that require the analyte or targeting species to be labeled with a particular chemical group or object in order to amplify its interaction with the device and those in which an unlabeled analyte can be detected directly from its interaction with the sensor. For many sensing methods, the detection limit is insufficient without such amplification, but labels may also be needed to distinguish the analyte from other species present in the sample. "Label-free" sensing methods are the focus of much of the research on biosensors because the species of interest very rarely possesses a useful tag naturally. Chemically attaching a label to the analyte in a sample is difficult, costly, and often impractical because of the specificity required in the reaction, especially when the sample is a complex fluid like blood and unintended conjugation reactions are all but unavoidable.

Electrical Biosensors

Biosensors that measure how electrical properties of a system change due proximity or contact with analyte have become widespread and enjoy the convenience of using a raw electrical signal, such as current or impedance, that can be processed directly. This well-represented class of sensors is summarized elsewhere [34, 35]. The most promising among these devices is the nanowire field effect transistors (FET). FETs are devices that monitor the current between two electrical terminals, called the source and drain, embedded in a semiconductor. A second electric field can be applied across two terminals oriented orthogonal to the source to change the concentration of charge carriers (electrons or electron holes) in the semiconductor and gate the current that reaches the drain. Figure 2.5a illustrates this principle.

A FET biosensor is composed of a semiconductor connecting the source and drain electrodes. Charged biomolecules that adsorb to the semiconductor sensor produce an electric field that acts as the gate and changes the charge carrier density within the device. The resulting drain current can be conveniently measured as a reporter for sensing applications. This type of device has been widely applied [34]. Its LOD is generally greater than 1 nM for most biomolecules because the electric field from the bound species only penetrates to a limited depth within the conduction channel. This problem is partly overcome by the use of nanoscale objects to bridge the source and drain such as carbon nanotubes [36, 37] or lithographically defined nanowires [38, 39]. The increased surface area-to-volume ratio for these structures allows the electric field due to adsorbed material to perturb a larger portion of the conduction channel, yielding an LOD low enough to allow for the detection of single virus particles [40]. Figure 2.5b depicts a generic nanowire FET biosensor.

In addition to being a sensitive label-free technology,nanowire FET biosensors can be produced relatively cheaply in parallel with traditional microfabrication techniques that are common in the semiconductor industry. These devices are well suited for incorporation into microfluidic flow cells, and they are sufficiently small to require only microliters of sample for a measurement. While the small sensor size affords a number of advantages, it also poses challenges when integrated in microfluidic systems. Sensing requires molecular interaction with the surface where, in the laminar flow of a microfluidic channel, the velocity is zero. Moreover, the high pressure drop in small channels limits the velocity of the flow and, thereby, the transient response of the sensing system.

The performance of most nanowire FET biosensors decays in the presence of salts. Most biomolecules

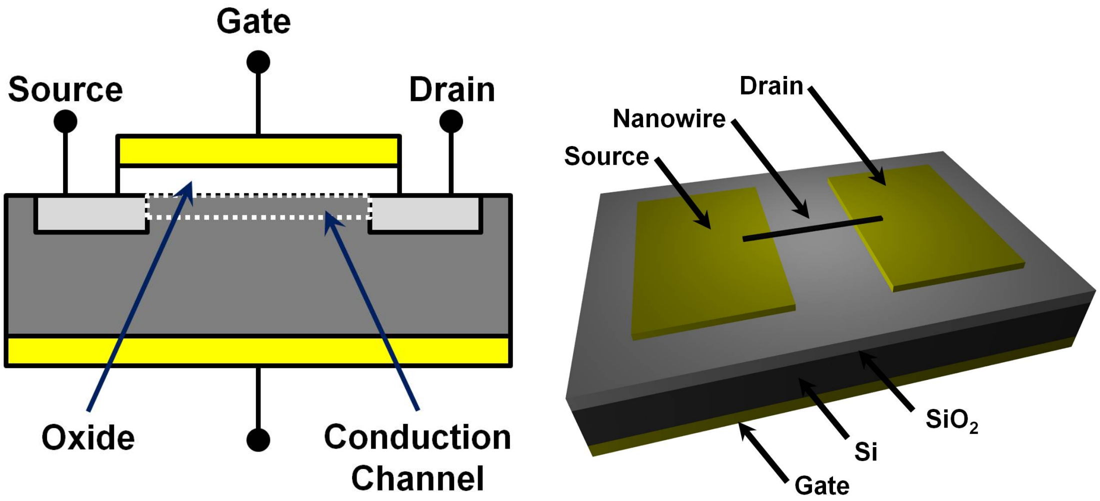

(a) FET

(b) Nanowire FET

Figure 2.5: Field effect transistors (FETs). (a) A generic FET, including the source and drain with conduction channel between the two. A field applied using the gate can control the density of charge carriers in the conduction channel and change the current measured at the drain. (b) A nanowire field effect transistor (FET) sensor. Biomolecules bound to the surface of the nanowire have a localized electric field that can distort the charge carrier density in the nanowire. Changes in the drain current are used to track how much material has adsorbed to the device.

require a buffered environment to screen interactions that would cause the molecules to precipitate and to stabilize their structure, so a pH-buffered salt solution is often used to dissolve samples of known analyte. Even biofluids like blood or saliva have their own salts and buffering agents for this purpose. These salts screen the electric field of the biomolcule, reducing its effect on the charge carrier population in the conductor [41], thereby limiting the sensitivity in biologically relevant fluids. This negates the field effect provided by the adsorbed material and limits the sensitivity in biologically relevant fluids.

The surface-bound molecular recognition species that enable specific sensing can also diminish the performance of nanowire FET biosensors due to screening effects. Such surface modifications can either promote or retard conduction, depending on the electrical properties of the nanowire. Some functionalization schemes can even modify the charge state of the nanowire permanently [27] and alter the fundamental electrical properties of the device. Identifying methods suitable for nanowire FET sensors remains a challenge.

Recently, however, a clever technique has been used to improve the applicability of these devices [42]. In this method, a two-stage flow system allows the sample to enter a chamber where an immobilized molecular recognition species can remove the analyte of interest through specific binding. The liquid in the chamber is then flushed and replaced with a low-salt buffer, creating an environment that promotes gradual dissociation of the analyte. This resulting solution is then driven into a second chamber where the nanowire FET sensor is located. The analyte is then free to interact with the sensor in the absence of unwanted species that may have been present in the original sample liquid while also removing the need for functionalizing the surface of the biosensor.

Mechanical Biosensors

Some biosensors use mechanical forces and motion to report the amount of analyte present in a sample. One important example of such a device is the microcantilever [43], which may be used in two modes of detection. First, the static deflection of these devices that results from specific adsorption can be used to measure analyte concentration [44]. Alternatively, the microcantilevers oscillate at a characteristic frequency, much like a tuning fork. This frequency is a function of the shape and material properties of the cantilever, and therefore changes upon adsorption of biomolecules. The deflection and the change in oscillation frequency can be monitored by reflecting a laser off the surface and tracking its position, much the same way as in an atomic force microscope. These label-free devices have been used to specifically sense medically relevant species in complex fluids with a limit of detection of ≈ 1 pM [44]. Their sensitivity limits the applicability of microcantilever sensors, but they can be easily produced using semiconductor processing techniques [45] and are easily functionalized by applying a gold or silica coating that also facilitates laser light reflection.

An alternative mechanical sensor is the quartz crystal microbalance (QCM) [46], which relies on the oscillation of a crystal and the change in resonant frequency as material adsorbs. This oscillation is stimulated electronically, but this frequency change occurs due to the mechanical coupling of bound bimolecules and the crystal surface. As with the microcantilevers, QCMs have LODs of > 1 pM. However, crystal microbalances are available as complete commercial products and are easy to integrate into flow devices. Like microcantilevers, QCMs are very well characterized and easily functionalized via their silicon dioxide surface chemistry.

Magnetic Biosensors

Another variety of biosensor uses changes in the magnetic properties of the system to detect a species of interest. For example, functionalized superparamagnetic nanoparticles can bind specifically to an analyte upon exposure to a sample or injection into an organism. Since these nanoparticles have much slower spin-spin relaxation (T_2) times than the biological species present, they create excellent contrast for magnetic resonance techniques like magnetic resonance imaging (MRI). These particles can be designed for polyvalent binding of the analyte, which amplifies the contrast in magnetic properties by promoting aggregation of particles. These devices are also called magnetic relaxation switches [47, 48] due to the immediate change in magnetic properties of the analyte upon binding with the nanoparticle.

Another common type of magnetic biosensor uses materials whose resistivity changes with applied magnetic field [49, 50]. Application of this magnetoresistive effect to the fabrication of devices with ultrathin ferromagnetic films has led to the development of magnetic random access memory (MRAM), read heads, and other highly sensitive magnetic nanostructures. These devices feature a multilayered architecture, where one layer is a magnetoresistive material and another is typically a layer that enables surface functionalization. Changes in current across these devices can be measured as analyte molecules labeled with ferromagnetic nanoparticles specifically adsorb to the sensor surface and introduce magnetic fields.

One drawback of these technologies is that they require labeled analyte be present in the sample. With exception to iron-containing and other metal-cluster proteins, few biological molecules naturally possess magnetic properties that can be exploited in magnetic resonance or magnetoresistive biosensors. Another disadvantage of magnetic biosensors is the nonspecific interactions that can occur between magnetic nanoparticles or between these nanoparticles are other mateirals. Aggregation in solution or adsorption of clusters onto the sensor surface can lead to false-positive measurements or other artifacts in the signal. Minimizing the size of these particles can help reduce aggregation. Despite these drawbacks, fabrication of magnetic biosensors and the molecular labels they require are typically affordable due to their prevalence in magnetic data storage technologies. They can also be incorporated into microfluidic systems with relative ease, making them useful devices for a limited range of measurements.

Optical Biosensors

Optical biosensors use the interaction between light and matter to report the presence of analyte. These technologies may be divided into two classes. The first uses a form of spectroscopy to isolate the signal due to the analyte, including Fourier transform infrared (FTIR) spectroscopy and ultraviolet-visable (uv-vis) specstroscopy. The most common technique in this class is fluorescence [51], which involves absorption of a photon by a molecule and the subsequent emission of a second photon of lower energy. This emission results from an electron relaxing from an excited state to its ground state. Molecules with electronic structures that allow for both efficient excitation and emission of light in the visible to near-infrared spectrum are referred to as *fluorophores*. Species which exhibit minimal fluorescence when exposed to a particular wavelength of light available for the experiment may be labeled with a fluorophore better suited to that wavelength to enable detection based on the intensity and spectrum of emitted light. The fluorescence signal is isolated using optical filters to eliminate background and excitation light, and collected using a detector (e.g., a photodiode, photomultiplier tube, avalanche photodiode, or charge-coupled device).

Though widespread in the literature, fluorescence measurements using fluorescently labeled species suffer two key drawbacks. First, attaching a fluorescent tag to the analyte can interfere with the binding reaction that occurs during specific sensing. This is more common for proteins, whose structures can be significantly perturbed by the inclusion of fluorophores, than it is for small molecule analytes. Second, quantitative fluorescence measurements can be inaccurate in the limits of both high and low concentrations of analyte. At low concentrations, the SNR is no longer the dominant factor in determining the LOD. Instead, light from sources other than the fluorophores (i.e., *background* light) may contribute more to the signal than the analyte. Threfore, the signal-to-background ratio (SBR), and not the SNR, often controls the sensitivity of the measurement at low concentrations. At high concentrations, the space between two freely diffusing fluorescently labeled analyte molecules may be sufficiently small so that an excited fluorophore may transfer its energy to a nearby fluorophore. Though it is often described in terms of an emitted photon exciting another fluorophore, the energy transfer involves no radiation. This process is called Förster resonance energy transfer (FRET) and can be used to report proximity between two fluorophores. High concentrations also lead to frequent interactions between biomolecules present in solution and, for some species, agglomeration. The particles that result may scatter sufficient light to diminish the excitation of fluorophores present or the amount of emitted fluorescence that may reach the detector. Regardless, a deceptively low signal may be recorded for fluorescence measurements at high concentrations.

A common fluorescence technique used for biosensing is the sandwich assay. In this type of experiment, the analyte is selectively bound to a surface by a targeting molecule (such as an antibody), which has been immobilized covalently on the surface of a well or other cell. By labeling the analyte molecule with a fluorescent tag, its surface concentration may be measured via highly sensitive fluorescence spectroscopy. Attaching a fluorophore to the antibody typically affects its affinity for the analyte, however. The sandwich assay avoids this problem by using unlabeled antibody and analyte, and exposing the cell to a fluorescentlylabeled antibody raised specifically for the bound complex. Fluorescence spectroscopy is then used to identify the presence of the antibody-analyte-antibody structure, as shown in Fig. 2.6.

Alternative fluorescence assays range from classical biochemical methods, such as Western blots or ELIZA assays, to new sensor technologies such as total internal reflection fluorescence (TIRF) [52]. In TIRF, one monitors the adsorption of material by measuring the amount of light given off by fluorescent tags attached to the surface-bound analyte molecules. These fluorophores are excited using the evanescent field that results from total internal reflection at the substrate, often a glass prism. Figure 2.6a illustrates this configuration, including the optical path. Fluorophores may only be excited by the evanescent wave, ensuring that only those fluorophores within a short distance (< 100 nm) of the surface will contribute to the emitted fluorescence signal. This technique significantly improves the SBR and, consequently, the sensitivity of the measurement.

The second class of optical biosensor uses changes in the phase of light to report the presence of analyte rather than changes in amplitude (i.e., absorption). A significant benefit of phase shift optical biosensors is that they do not require a label be present in order to detect the resonance. While spectroscopic methods are limited by the weak interaction between light and the analyte (or label) unless a wavelength is used that corresponds to a particular mechanical or electronic resonance which may be excited, phase delay methods

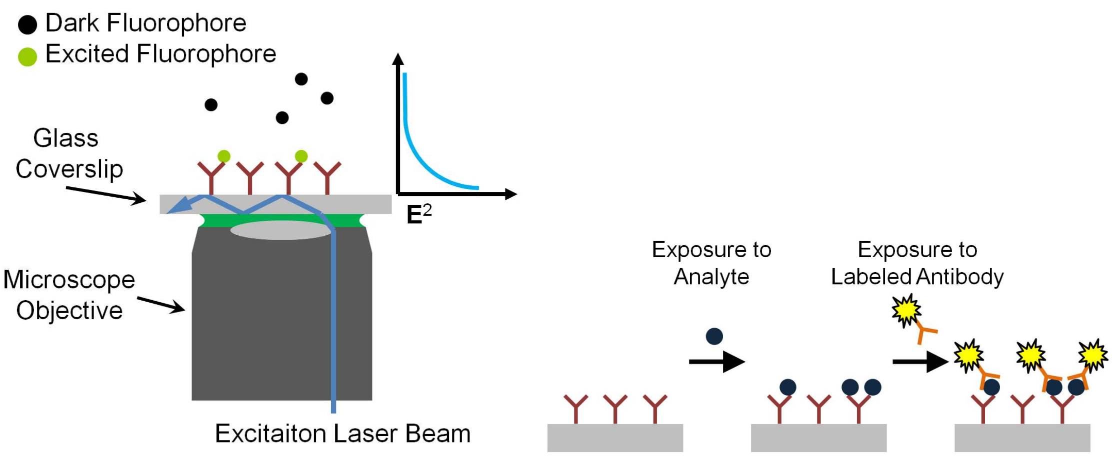

(a) TIRF (b) Sandwich Assay

Figure 2.6: Fluorescence-based biosensor technologies. (a) Total internal reflection fluorescence (TIRF) is characterized by the excitation of fluorescentlytagged species at a surface by an evanescent field that decays exponentially and excites only those fluorophores near the surface. (b) Sandwich assays feature exposure of an antibody-labeled surface to an analyte solution, followed by exposure to a fluorescentlylabeled antibody that binds exclusively to the complex.

require only contrast in the real part of the refractive index, n, to register a change. Moreover, measuring a phase shift is straightforward when using an interferometer, and often significantly reduces the noise of the measurement. Backscatter interferometry exemplifies this strategy [53, 54]. In this method, light is split into two paths; one path is allowed to interact with the sample (the *sample path*) while the other is not (the *reference path*). The two paths are recombined before being sent to a detector. Only when the length of the two paths differ by an integer number of wavelengths will there be constructive interference and the intensity registered by the detector will be equal to that before the split. For any other case, the detector will show a harmonic function in time whose frequency can be related to the difference in path length. Any change to the refractive index along the sample path will cause a phase shift in the light, and backscatter interferometry uses the transient change in frequency that results from combining this phase-shifted light with the reference path light to indicate when analyte is present. This method can detect quantities of material as low as a 30 zeptomoles (30×10^{-21}) [54], however it is ill suited for complex biological samples and requires high concentrations (> 1 pM) of analyte. Regardless, it is still a useful analytical tool as it requires *very* small sample volumes, as low as 3 picoliters, and can easily be incorporated into microfluidic flow cells.

Surface plasmon resonance (SPR) is a phase shift optical biosensor technology that has become a benchmark in the field over the last decade due to its commercial availability in the form of the Biacore$^{\text{TM}}$and other instruments, well-characterized performance, and adaptable functionalization architecture [55, 56]. This type of biosensor involves using a surface-propagating electromagnetic wave to excite an oscillation in the surface conduction electrons of a material. The plasmon-capable material is typically a metal, such as gold or silver, that can be deposited onto a dielectric, such as silica, and has a complex refractive index $= n + i\kappa$, such that $\kappa > n$. Material that adsorbs to this metal surface alters the local refractive index and, consequently, the local wavelength of the light. A surface wave is produced via total internal reflection (TIR), as shown in Fig. 2.7, at an angle that depends on the refractive index experienced by the surface wave and the incident wavelength. By scanning either incident angle or wavelength, the shift in plasmon resonance can be tracked and the surface binding reaction monitored.

Like all phase shift optical sensing technologies, SPR requires no label on the analyte. The technique is well suited to a flat microfluidic channel geometry for which mass transfer is well understood [57]. It has been used to observe analyte concentrations $>$1 pM with unlabeled analyte, although a LOD as low as 1 fM has been achieved by attaching plasmonic tags (e.g., gold nanoparticles) to the analyte [58]. Many of the commercial instruments based on this technology feature integrated flow systems and optional automatic sampling mechanisms to enable automated serial measurements. Commercial implementations also often include another advantageous feature—reference channels. In this case a targeting layer is not deposited on one channel so that its signal may be subtracted from other channels to account for non-specific binding. Most commercial SPR chips are prepared with a polymeric coating that is designed to facilitate surface functionalization.

The most significant shotcomings of this technology are the limited sensitivty while using label-free analytes and the high cost. Commercially available SPR instruments commonly cost in the range of \$100,000-\$300,000. Nonetheless, it is an excellent tool for high-concentration sensing ($>$ 100 fM), and enables the measurement of kinetic rate constants with relative ease. It stands as one of the most reliable and adaptable

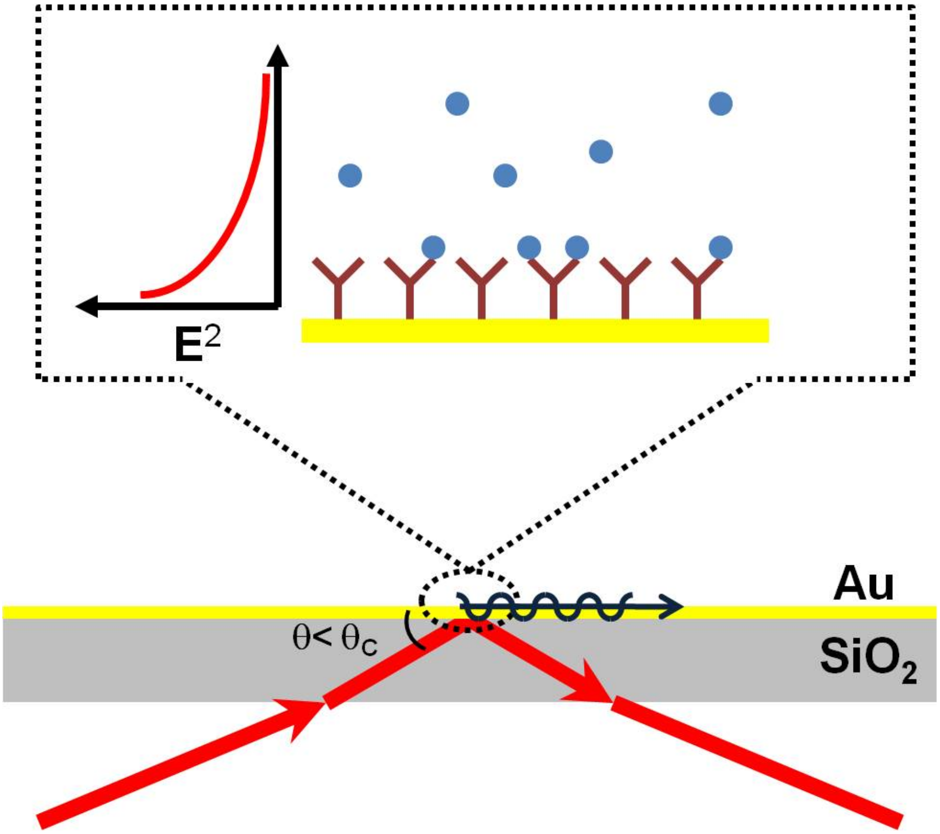

Figure 2.7: Surface plasmon resonance (SPR). Here a surface-propagating wave is generated via total internal reflection in a thin gold film deposited on silica in order to excite a surface plasmon in the metal. Material that adsorbs to the surface shifts the plasmon resonance, which must be compensated for by altering the incident angle of light or the incident wavelength. In this way the surface binding reaction between immobilized targeting species and analyte may be monitored.

tools available today for evaluating biomolecular reaction rates and affinities.

A comprehensive review of label-free optical sensor technologies may be found in Ref. [59]. The work described in this thesis focuses on optical resonators. These devices use resonance to build up intense optical fields and amplify the interaction between light and adsorbing material. The change in refractive index that results from adsorption induces a phase shift in the circulating light and a change in the wavelength required to excite resonance. Description of the fabrication, implementation, and modeling of these devives may be found in subsequent chapters.

Chapter 3

Whispering Gallery Mode Resonators as Biosensors

The previous chapter introduces biosensor technologies according to the physical nature of their signal transduction processes. Optical biosensors are just one category that includes a wide array of novel devices. The present work deals with a technology based on whispering gallery mode (WGM) optical resonators [60, 61]. Understanding how they are fabricated and used is important for appreciating their performance and limitations. This chapter will, therefore, introduce this class of resonator sensors and describe how these devices can be used for specific detection of biomolecules in solution.

WGM optical resonators exhibit tunability and narrow resonance linewidths, and attain extraordinary optical field intensities that originally led to their use in telecommunications as add-drop filters [62, 63], notch filters [64, 65, 66], and lasers [67]. They have since evolved into valuable tools for probing nonlinear optical phenomena [68, 69] and quantum eletrodynamical principles [70]. We are concerned here with the application of WGM optical resonators as chemical sensors, a development that is less than a decade old [5, 6]. In that short time, however, researchers have demonstrated a wide variety of sensing applications. These include, but are not limited to, biochemical assays [71], biomedical assays [72, 73, 74], and molecular biology studies [1, 33]. Their extreme sensitivity (see Chapter 5) in these arenas has generated a great deal of interest in using them to develop analytical and diagnostic instrumentation.

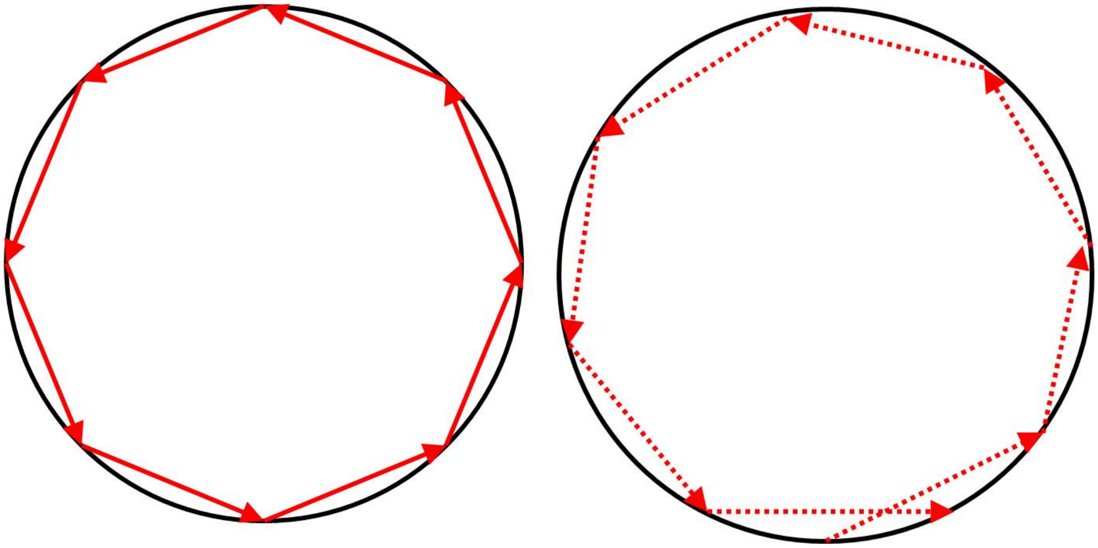
(a) On Resonance (b) Off Resonance

Figure 3.1: Whispering gallery mode resonance in the limit of geometric optics.

3.1 Resonance

Whispering gallery mode resonators derive their name from the path that the resonant light takes as it circulates in the cavity. This path is similar to the one that sound waves took along the curved wall of a circular room studied by Lord Rayleigh [75]. In these whispering galleries, two people standing facing the wall at opposite sides of the room can hear each other even at a whisper. These people would hear not be able to hear each other if either stepped backward toward the center of the room, however. This effect is caused by the smooth, curved walls guiding the sound waves around the periphery of the room with great efficiency. Sound waves taking any other path to the listener are dissipated or scattered en route. WGM optical resonators are dielectric structures capable of trapping light in paths around the periphery similar to those taken by sound waves traveling from one person to another in a whispering gallery. Though Mie [76] and Debye [77] described the resonant eigenfrequencies of dielectric spheres before Lord Rayleigh's work, the name was not applied to this type of optical resonator until much later.

Light that propagates through a dense material may polarize that medium, depending on how the molecules interact with the time-varying electric and magnetic fields. The permittivity of a material, ϵ_m, describes the time delay in the molecular response to the optical fields, and can be expressed in terms of the permittivity of a wave propagating through vacuum, ϵ_0, and a material-dependent relative permittivity, ϵ_r, i.e., $\epsilon_m = epsilon_r \epsilon_0$. It is often more convenient to work in terms of the refractive index, whose real part can be expressed as the ratio of the speed of light in a material $v_m(\lambda, T)$ to that in vacuum c. The complex refractive index at temperature T and wavelength λ is defined as

$$n(\lambda, T) = N(\lambda, T) + i\kappa(\lambda, T) = \frac{c}{v_m(\lambda, T)} + i\kappa(\lambda, T). \tag{3.1}$$

The imaginary part of is related to the loss mechanisms in the material, like absorption or scattering.

The speed of light in the medium is the product of the frequency of the electromagnetic wave, ν, which is independent of the material, and the wavelength in the medium, λ_m. This relationship may be expressed in terms of the speed of light in vacuum, λ_0, as

$$\lambda_m = \lambda_0 \frac{v_m}{c} = \frac{v_m}{\nu} = \frac{\lambda_0}{n}. \tag{3.2}$$

The fields of optical physics and photonics typically describe light according to its frequency because that value does not vary according to the medium, however the biology community has established as convention the practice of using wavelength to characterize light. Since the present work deals with optical biosensors, I will adhere to the practices of the biology community and refer to the wavelength of light. Equation (3.2) and the expression

$$\Delta\nu = -\Delta\lambda \frac{c}{\lambda^2} \tag{3.3}$$

may be used to convert between frequency or changes in frequency and their equivalents in wavelength-space.

WGM resonators typically have circular cross sections that enable light to be trapped as it propagates near the periphery. This circulating light is confined via total internal reflection at the interface between the resonator and the surrounding medium. Light for which a round trip is equal to an integer number of wavelengths, M, returns to the point it was coupled into the resonator in phase with itself, as illustrated in Fig. 3.1. Constructive intereference occurs under these conditions, allowing the circulating intensity to grow until the rate at which light is coupled into the cavity is balanced by the rate at which it is lost. This phenomenon is referred to as *resonance* and the 3-dimensional electromagnetic field profile that describes the path the resonant light takes is called the *mode*.

For a given resonator, many modes are accessible. A particular mode is characterized by its mode number, which can be approximated as the number of wavelengths within the cavity, M, and by the wavelength required to excite that mode, λ_R. It is apparent from the criteria for resonance

$$2\pi n_{mode} R_{mode} \approx M\lambda_R \tag{3.4}$$

that the resonant wavelength is a function of the refractive index encountered by the mode as well as the radius of the mode, where $R_{mode} \approx R_{res}$ and R_{res} is the radius of the resonator. The free spectral range (FSR) is the wavelength interval that separates a mode of order M and its next-highest order mode $(M+1)$. This quantity may be is expressed in terms of the resonator size and the excitation wavelength λ as

$$FSR = \frac{\lambda^2}{2\pi n R_{res}}. \tag{3.5}$$

Within one FSR lies a resonant wavelength corresponding to every accessible mode in the device, although each mode may have a different order for a particular interval. Searching for resonant modes in a WGM resonator over an interval longer than one FSR is unnecessary, as one may simply begin finding higher orders of modes that were identified earlier in the search.

3.2 WGM Mode Structure

The electromagnetic field profile for a given WGM resonator is described by the Helmholtz equation

$$\nabla^2 E + \omega^2 \mu \epsilon_m E = 0. \tag{3.6}$$

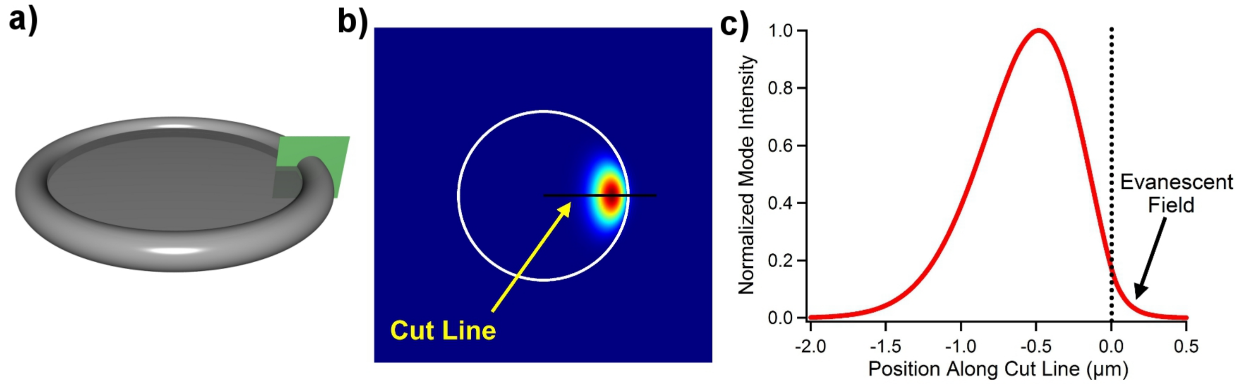

Figure 3.2: (a) A toroidal WGM resonator with a cut plane marked in green. (b) An image of the normalized mode intensity along the cut plane in (a) as calculated using the finite element solver COMSOL Multiphysics. (c) A closer look at the normalized mode structure along the cut line in (b) shows the evanescent field that extends into the water.

Solutions to this equation in spherical and toroidal coordinates are presented (or approximated) elsewhere [78, 79, 80] and describe a feature of WGMs that is critical to their use as sensors. Specifically, the electrical field in the θ-direction (the direction of propagation) can be separated into its contributions in each dimension $E_\theta = \psi_r(r)\psi_\theta(\theta)\psi_\phi(\phi)$. The radial component ψ_r varies with radius r according to

$$\psi_r(r) = \begin{cases} Aj_l(kr) & r < R_{res} \text{ (inside the resonator)} \\ B\exp\left(-\alpha_{EF}(r - R_{res})\right) & r \geq R_{Res} \text{ (outside the resonator)} \end{cases} \tag{3.7}$$

where $j_l(kr)$ is a Bessel function of order l (the angular mode number), $k = \omega\sqrt{\mu\epsilon_m}$ is the wavenumber, A and B are constant coefficients, and α_{EF} is the field decay constant. The exponential decay outside of the resonator is the so-called *evanescent field*, and results from total internal reflection.

As can be seen in Figure 3.2, this evanescent field is available to interact with material that either approaches close to or adsorbs onto the resonator surface. One may substitute the effective refractive index, n_{eff}, into the simplified resonance criteria in Eq. (3.4) to more accurately take into account the distribution in optical intensity that spans both the resonator and the surrounding medium. This gives the updated resonance criteria

$$2\pi n_{eff} R_{mode} \approx M\lambda_R, \tag{3.8}$$

where the effective refractive index is defined as

$$n_{eff} = \frac{\int n(\mathbf{r}) E(\mathbf{r})^2 \, d\mathbf{r}}{\int E(\mathbf{r})^2 \, d\mathbf{r}}. \tag{3.9}$$

These expressions provide the tools to predict how a resonator will respond when material, like the biomolecules involved in sensing experiments, interacts with the mode.

Any change to n_{eff} or R_{mode} will result in a shift $\Delta\lambda_R$ in the resonant wavelength for a particular mode (i.e., constant M). This relationship was expressed by Vollmer and Arnold [81] as

$$\frac{\Delta\lambda_R}{\lambda_R} = \frac{\Delta n_{eff}}{n_{eff}} + \frac{\Delta R_{mode}}{R_{mode}}. \tag{3.10}$$

Thus, any perturbation of the refractive index or cavity path length, including ones that result from changes in the temperature or composition of the surrounding fluid, will produce a change in λ_R. This is illustrated in Fig. 3.3 by the resonance shift that results from changing the medium surrounding a toroidal WGM resonator from pure water to a common biological buffer solution consisting of sodium phosphate and sodium chloride (also called *phosphate buffered saline*, or PBS). Since the PBS buffer contains solutes with refractive indices greater than that of water, the mode experiences an overall increase in n_{eff}. Replacing the PBS with water again restores the resonantor to its previous environment, and the resonant wavelength returns to its original value as expected.

3.3 Quality Factor

The strength of the electromagnetic field available to interact with material that adsorbs to the surface of the resonator is determined by the rate of optical energy coupled into the cavity, P_C, and the rate of loss, P_D. The quality factor Q is the figure of merit used to describe the efficiency with which a resonator contains

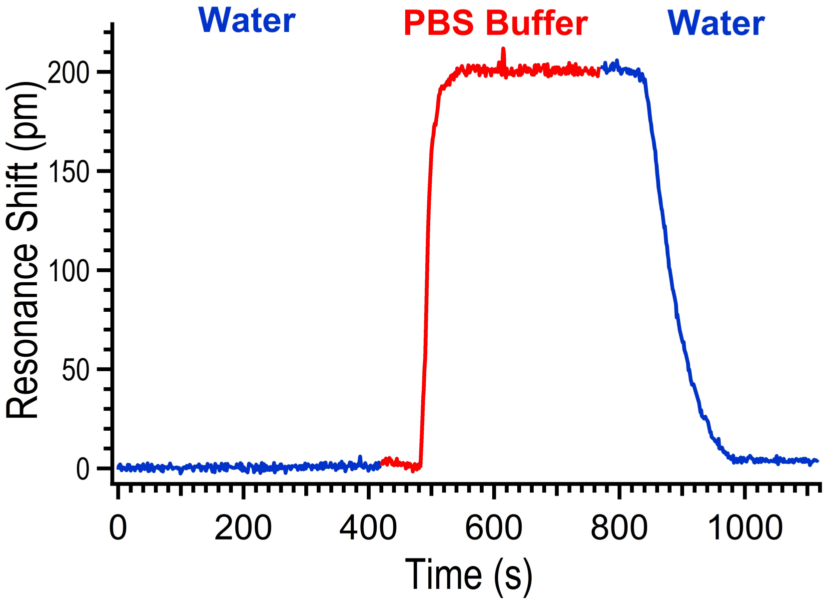

Figure 3.3: Flowing PBS buffer into the flow cell changes the refractive index of the surrounding medium, thereby causing a resonance shift according to Eq. (3.10). This is a basic and non-specific sensing method.

light, and how intense the optical mode is within the cavity. A resonator with a high quality factor loses less light and supports more intense electromagnetic fields than one with a lower Q. The shift in resonant wavelength upon adsorption of material may depend on Q. Though the quality factor can be be interpreted in a variety of ways, what follows are the three most common representations of Q.

1. **Steady-State Energy Balance**

The quality factor may be expressed as the ration of energy stored in the resonator to the energy lost during each optical cycle, where an optical cycle is based on the resonant angular frequency ω_R and $\omega_R = 2\pi v_m/\lambda_R$. The total energy in the resonator may be calculated by integrating the energy densities of the electric ($\tilde{W}_e$) and magnetic ($\tilde{W}_m$) fields over all positions $\mathbf{r}$, $W = \int (w_E + w_M)\, d\mathbf{r}$. At steady-state, the rate of energy lost from the cavity is equal to the rate of energy entering the cavity,

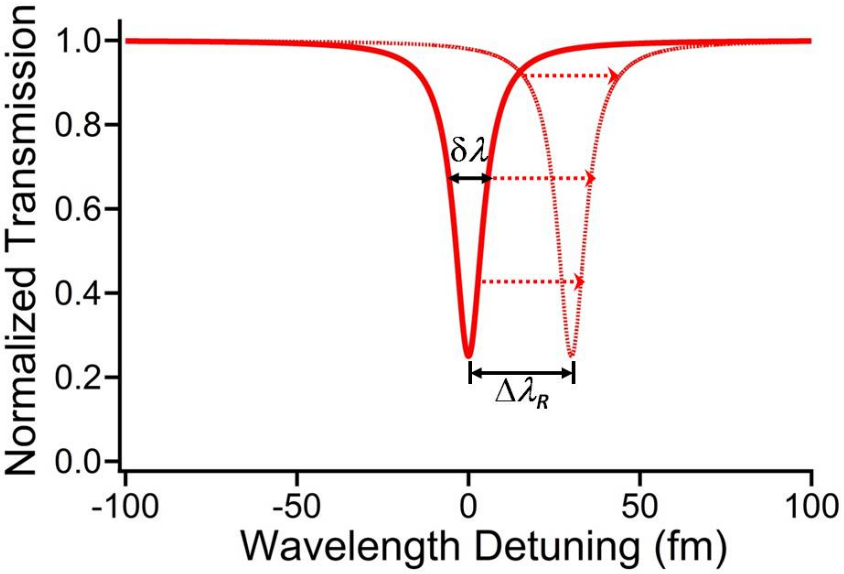

Figure 3.4: Transmission spectra depicting a resonance red-shifting a distance $\Delta\lambda$ in wavelength-space in response to adsorption of protein to the resonator surface. The minimum fractional transmission, along with the total transmission when no light is coupled into the resonator, may be used to calculate the coupled power P_D. The value of Q may also be determined using the observed value of $\delta\lambda_R$ and Eq. (3.12).

leading to the following expression for quality factor:

$$Q = \omega_R \frac{W}{P_D} = \omega_R \frac{W}{P_C}. \tag{3.11}$$

2. **Resonance Linewidth**

Alternatively, the quality factor may be expressed in terms of the readily measured resonant wavelength (λ_R) and linewidth ($\delta\lambda_R$). Both of these quantities may be determined from a transmission spectrum, like the one in Fig. 3.4, and related to the quality factor using the following simple expression:

$$Q = \frac{\lambda}{\delta\lambda}. \tag{3.12}$$

Note that for an ideal, loss-less resonator, there is an infinite Q because $\delta\lambda_R = 0$.

3. **Cavity Ringdown Time**

Since the quality factor describes the rate of loss in a material, it is also be related to the time required for the light in a cavity to completely dissipate [82]. The instantaneous energy within a resonator is difficult to measure, so this type of cavity ringdown measurement requires monitoring the rate of light leaving the cavity through the optical waveguide previously used to couple light in. A photodetector may be used to measure this leakage light and calculate the quality factor based on an curve fit to that data where the exponential decay constant is the ringdown time τ_{RD}:

$$Q = \omega_R \tau_{RD}. \tag{3.13}$$

These expressions are all equivalent. Moreover, the quality factor can be deconstructed and expressed in terms of the individual loss mechanisms that exist in a resonator. This paradigm was originally introduced by Gorodetsky and colleagues [83] for spherical WGM resonators and expresses the quality factor in a manner similar to how resistors in series contribute to the resistance of a circuit. This expression is

$$\frac{1}{Q_{tot}} = \frac{1}{Q_{mat}} + \frac{1}{Q_{scat}} + \frac{1}{Q_{rad}} + \frac{1}{Q_{ext}}, \tag{3.14}$$

where Q_{mat} refers to the intrinsic material loss, Q_{scat} refers to surface scattering loss, Q_{rad} refers to the tunneling (radiation) loss, and Q_{ext} refers to the losses involved in coupling into external modes. The first three of these terms all involve loss mechanisms *within* the resonator, implying that these mechanisms must be dealt with and minimized in order to fabricate resonators with as high Q values (i.e., electromagnetic field intensities) as possible.

Material Loss

Gorodetsky et al. point out the most significant source of material loss in optical resonators is often absorption of light by the cavity material or the surrounding medium [83]. This loss can be characterized by the absorption decay constant α_{mat} according to

$$Q_{mat} = \frac{2\pi n}{\lambda \alpha_{mat}}. \tag{3.15}$$

This expression can be used to describe how the Q of a cavity will vary with environment within which the measurement is made. For example, the moisture content of air leads to adsorption of water onto a silica resonator, thereby limiting the Q when excited WGMs using light in the near-infrared where water has a high α_{mat}. Lasers in the visible spectrum (e.g., $\lambda = 633$ nm) and their corresponding optical components, which are often more costly than those in the near-infrared range used in telecommunications, are required for WGM optical resonator applications in aqueous environments if ultrahigh quality factors are necessary. The absorption-limited quality factors for resonators in water have been described in detail elsewhere [84].

Scattering Loss

Scattering loss typically occurs as a result of crystal faces in crystalline, anisotropic media or other imperfections where light experiences a discontinuity in refractive index. This includes both internal and surface imperfections that arise from contamination or roughness. Scattering losses may be minimized by choosing amorphous, homogeneous media and taking steps to ensure a smooth surface. Melting amorphous silica has emerged as a strategy to overcome these challenges, found most commonly in the fabrication of microsphere and microtoroidal resonators, and is now sufficiently widespread that scattering losses are rarely the limiting factor in the determination of Q_{tot}. The surface tension of molten silica leads to ultra-smooth surfaces, minimizing both the root mean square (rms) size, σ_{rms}, and length, B, of inhomogeneities. The scattering-limited quality factor may be expressed as

$$Q_{scat} = \frac{\lambda^2 R_{res}}{\pi^2 \sigma_{rms}^2 B}. \tag{3.16}$$

Radiation Loss

When the path length within a WGM cavity is sufficiently small that the resonant light undergoes few optical cycles during a round trip (i.e. <100), the angle at which that light approaches the interface is steep enough to reduce the efficiency of the total internal reflection responsible for shaping the optical path. Some of this light is lost because it cannot be confined in a path that turns quickly enough. There exists no explicit expression for tunneling loss in a WGM resonator, but the overall radiation loss can be minimized by making using resonators with the largest radii possible for a given application. It appears that for $R_{res} > 30$ μm, absorptive or scattering losses become dominant in silica microspheres [85]. While this provides a lower constraint when selecting a resonator size, the upper bound will come from the free spectral range. Increasing the resonator size will result in an increased mode density in wavelength-space, making it challenging to track the shift of a single resonance due to the overlap of its Lorentzian transmission trough with that of another mode.

3.4 WGM Resonator Fabrication

WGM resonators exist in a variety of different geometries, including spheres, cylinders, disks, and toroids. The present work focuses on toroidal resonators, which pose wholy unique fabrication challenges. This process is outlined in Fig. 3.5, and features three steps[82]. The first step is photlithography, which begins with a silicon wafer on which 2 μm of thermal oxide has been grown. A photoresist is spun onto the sample and a photomask is used to develop a pattern of circular pads from this layer. These pads protect regions of the silica during the second step, which involves exposure of the entire chip to buffered oxide etchant (BOE), a diluted hydrofluoric acid solution that selectively etches SiO_2. The photoresist is then washed off of the sample to reveal a pattern of silica disks on a clean silicon wafer.

The third step defines microdisk resonators by employing a gas phase $\mathrm{XeF_2}$ etch to isotropically remove *only* the silicon. The glass disks are “undercut," leaving them resting on silicon pedestals. There are other methods to selectively etch silicon, including concentrated potassium hydroxide, however it etches only along certain crystal faces in the silicon and can produce pedestals that are not round. Figure 3.6 shows one of these pedestals. This $\mathrm{XeF_2}$ etch step is often the slowest of the entire fabrication process. Scaleup is difficult because the etch chamber must efficiently deliver etchant to the sample as evenly as possible (ruling out forced convection) while making sure that the depletion zone formed around one sample does not overlap another sample. The chamber cannot be made too large, however, because it must be pumped down to very low pressures and purged with nitrogen between etchant pulses due to the toxic nature of the etchant and product gases.

The final step of the toroid fabrication process involves melting the edges of the silica microdisk using a focused $\mathrm{CO_2}$ laser putting out 10.6 μm normal to the plane of the resonator. This process is often referred to as *reflowing* the disk, and is possible because silica absorbs light $\approx 1000\times$ more efficiently at 10.6 μm than the silicon below it. The etching process removes the silicon from beneath some of the disk, ensuring that the absorptive heating of the silica there results in melting. The surface tension of this molten silica at the periphery of the disk drives the symmetric, inward collapse of the structure toward pedestal, which acts as a heat sink preventing the portion of the disk above it from building up sufficient heat to melt. The end result is a silica toroid supported by a silicon pedestal.

Ultimately, the major and minor radii of the toroid are determined by the diameters of the original disk diameter relative to the pedestal. It is best to manually increase the power of the $\mathrm{CO_2}$ laser, watching the toroid as it forms and stopping when an increase in power fails to produce additional reflow. Extremely high laser powers can generate toroids that are deformed due to the wetting of the silicon pedestal with molten silica. Though these deformed devices will still support WGMs, a great deal of the resonant light will be absorbed by the nearby silicon, resulting in very low quality factors. A helpful rule of thumb to avoid this problem is to stop increasing the power when the separation between the toroid and the pedestal is roughly

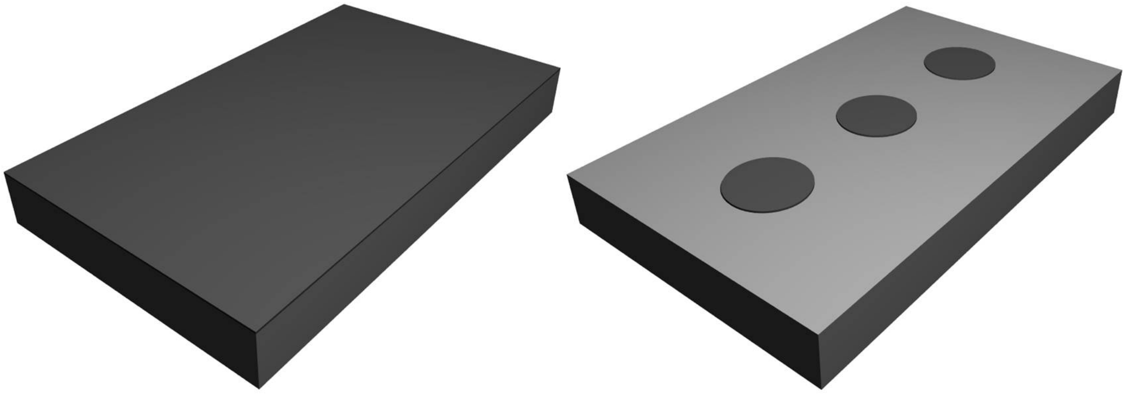

(a) Silicon Wafer with Thermal Oxide Layer

(b) Etched Silica Circles

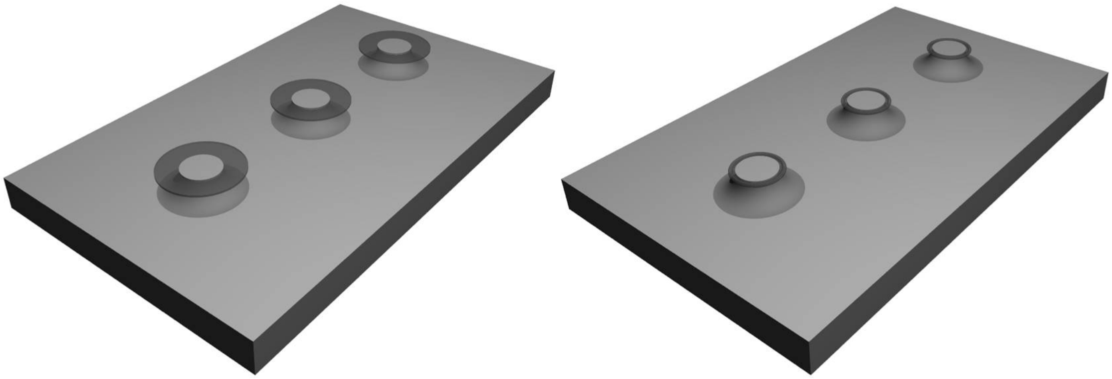

(c) XeF_2 – Etched μDiskResonators

(d) Reflown Toroid Resonators

Figure 3.5: The four-step process to fabricate toroidal WGM resonators on (a) a bare silicon wafer with 2 μm of thermal oxide. (b) Photolithography is used to define a pattern of silica discs through a buffered oxide etch process. (c) The chip is exposed to XeF_2, an gas that isotropically and selectively etches the silicon from beneath the silica disks. (d) A CO_2 laser at 10.6 μm wavelength light is focused normal to the microdisks, melting the edges and leaving microtoroid resonators on silicon pedestals.

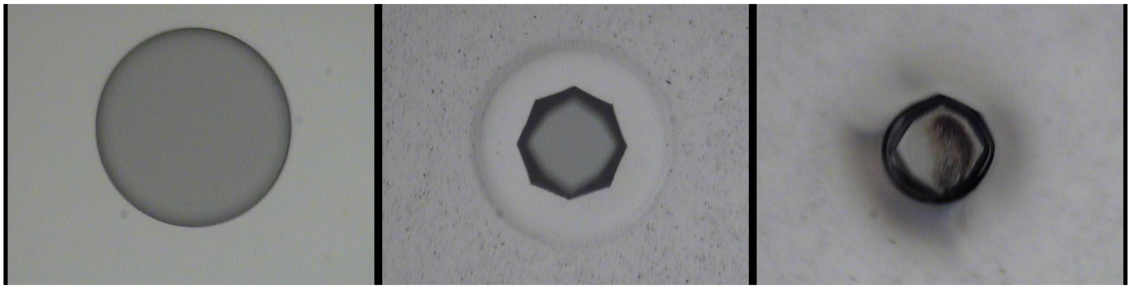

(a) Before KOH Etch (b) After KOH Etch (c) After Reflow

Figure 3.6: Three photographs of a single disk during an experiment to use a a KOH etch procedure (10 minute piranha clean followed by a 90 minute exposure to 30 wt% KOH in water) to define a silica disk followed by reflow with a CO_2 laser. The anisotropic nature of the KOH etch produces an off-round pedestal, eliminating any chance of a smooth toroid. Note: field of view in all images is 310 μm wide

equal to the minor diameter of the toroid itself. This optimized laser power may change from one chip to the next as a result of slight nonuniformity of the XeF_2 etch process throughout the etch chamber. The experimental apparatus used for this process is shown in Fig. 3.7.

Microspheres are simpler to make than the toroids and disks described above. Spheres are made by melting the end of a cleaned, stripped optical fiber with either a CO_2 laser setup, as in Fig. 3.7, or a hydrogen flame. In this way, the resonator is really a spherical bulb on the end of a fiber that may be conveniently manipulated. The majority of fiber has an outer diameter of 125 μm, limiting the minimum possible diameter of the resonator. The FSR of such a device is small enough to cause problems resolving single modes during a scan through wavelength space. Smaller spherical resonators that are more useful for biosensing applications may be fabricated by starting with the narrow end of a tapered optical fiber rather than an unaltered piece.

Microcyliinder resonators are perhaps the most straightforward to produce, as they require only minor alteration of an optical fiber. In order to remove the polymer jacket of the fiber without scratching the smooth silica surface beneath, I submerge fiber scraps $1 - 2$ inches in length into a dichloromethane bath overnight. The polymer absorbs this solvent, swells, and slinks off the fiber like a sock. After a rinse, presents a sufficiently smooth surface that it may support modes with quality factors as high as 2.3×10^7 in water. These results are illustrated in Fig. 3.8. Unlike spherical and toroidal devices, whose geometries include

(a) Present Reflow Setup Diagram

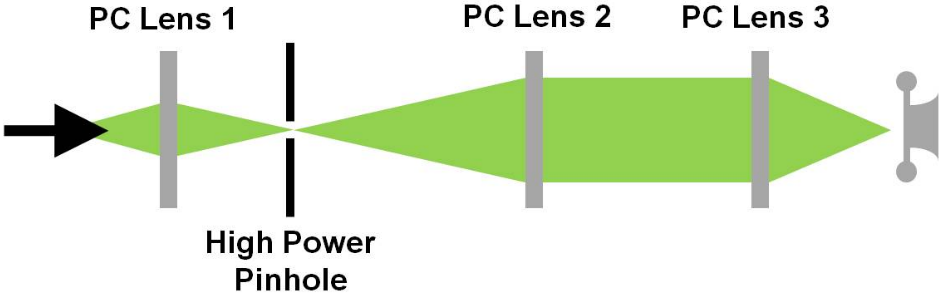

(b) Alternative Reflow Setup Diagram

Figure 3.7: Diagrams of experimental reflow apparatus. The black arrow indicates the laser source. Plano-convex (PC) lenses made from ZnSe, which does not absorb light at 10.6 μm like silica optics do, are also shown. The alternative setup proposed in (b) may have the advantages of a cleaner beam profile due to both the spatial filter (pinhole) as well as better control over the beam diameter entering the third PC lens.

material interfaces above and below the WGM, cylindrical resonators support many “corkscrew" modes that result in a great deal of loss in the direction normal to the WGM (see Fig. 3.9).

Comparison of toroidal, spherical, and cylindrical resonators reveals inherent advantages and disadvantages of each. Specifically, the minor diameter of a toroid excludes the many non-azimuthal modes that are supported in spherical and cylindrical cavities. The “compression" of the toroidal mode that results from confinement in the axial direction can also make it easier to couple light into the device may be positioned farther from the the cavity than in other geometries while achieving the same coupling efficiency. Work by Spillane also speaks to the relative mode confinement in a sphere and a toroid, pointing out that the optical fields are more intense in a toroid of identical Q due to the vertical compression of the mode compared to a sphere [78]. Spherical and cylindrical resonators, however, do not require access to a cleanroom because they are not made using photolithography. That they are made from relatively inexpensive optical fiber scraps also make these cavitiy geometries far less expensive than toroids, which require silica-on-silicon wafers. Finally, the process of incorporating a toroidal resonator into a microfluidic cell is far simpler than with spherical and cylindrical devices because they are fabricated on a planar chip that may be attached to the floor of a flow channel. It is clear that all of these features must be taken into account when designing a biomolecular assay based on one of these geometries of WGM optical resonator.

3.5 Coupling Light into WGM Resonators

The task of coupling light into a resonator is one that has been studied thoroughly [86, 87, 88]. This may be accomplished, albeit inefficiently, by simply shining a light onto the resonator. The solutions for a plane wave incident upon a dielectric microsphere are given in detail elsewhere[89]. This Mie scattering pattern predicts that an infinite number of modes exist and all are energy degenerate for an ideal resonator (i.e., no loss). In reality, imperfections lead to some modes existing at a higher energy state than others, a feature that may be exploited to study these quantized states and their interactions as model systems in quantum electrodynamics. In practice, the use of a waveguide leads to far more efficient methods for coupling light

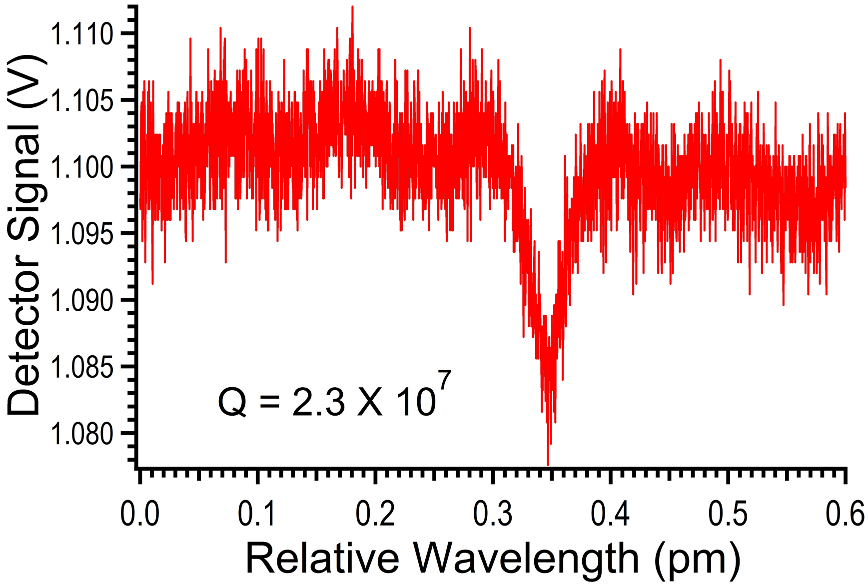

Figure 3.8: Coupling of 633 nm light into a 125 μm diameter optical fiber in water with $Q = 2.3 \times 10^7$

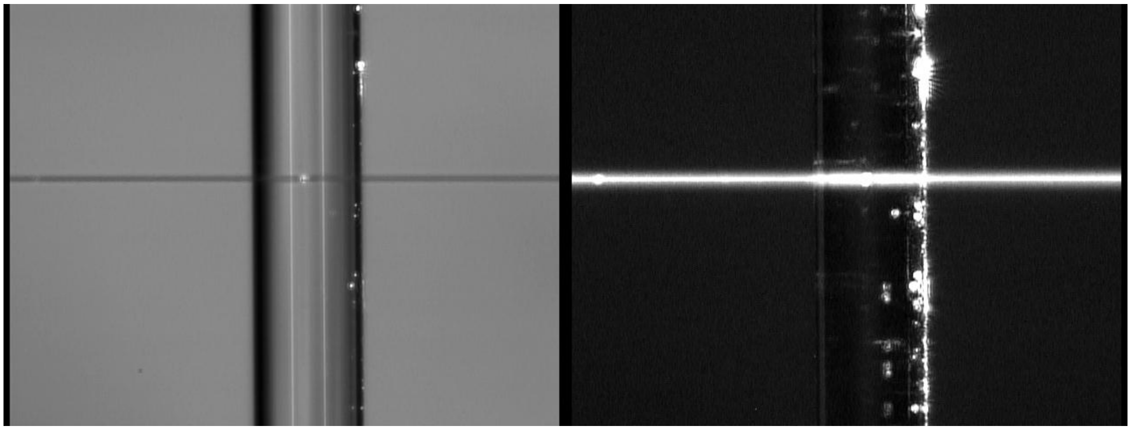

(a)

(b)

Figure 3.9: Coupling 633 nm light into a microcylindrical WGM resonator. (a) Illumination of the taper and resonator by a bright field, and (b) illumination of the system by only the coupled light. The bright spots in (b) indicate how light is coupled into "corkscrew" modes, reaching parts of the fiber far from the taper and being scattered.

into WGMs. Moreover, waveguide coupling techniques each introduce inherent losses because the waveguide itself may interact with the resonant light and alter the Q via the last term in Eq. (3.14).

Regardless of the method, coupling requires phase matching between the resonant light and incoming light. This means that the overall phase velocities must match, an unlikely event in the case of a free space wave in air or water incident upon a silica resonator. Mismatch leads to a significantly lower coupling efficiency. The fact that light propagates at different velocities in different media implies that one way to achieve phase matching is to simply match the refractive indices of the waveguide and the resonator. This principle has given rise to a number of silica waveguide-based methods for coupling light into silica WGM resonators, which are described in greater detail elsewhere [90, p. 11]. The most common and efficient method involves using a tapered optical fiber waveguide fabricated by pulling the two ends of fiber while it is held over a flame to melt a small section. By creating the tapered section, one provides a small region where the mode leaks out of the fiber radially in an evanescent field. Positioning the resonator in proximity of this field enables coupling with minimal loss.

It is important to use a hydrogen flame to ensure that the taper pulling process does not leave a hydrocarbon film to contaminate the waveguide. While there are some who have pulled tapers often enough that they can simply monitor their thickness using a camera and tell when to stop pulling, the method used in the present work is to monitor the transmission through the taper during the pulling process. As the melted segment thins, it will support a variety of modes that interfere in different ways. The transient signal consequently oscillates with a frequency and amplitude that changes over time to reflect the decreasing number of transmission modes available. The transition to a single-mode regime is marked by the end of oscillations. A single-mode waveguide is required to couple the maximum amount of light possible into a resonator. Multimode waveguides limit this coupling efficiently because only one of the transmission modes, a fraction of the total transmitted optical power, will be phase-matched to the WGM at a time. It is helpful to remember that the single-mode taper diameter is larger in water than air due to the diminished contrast in refractive index. This allows a slightly thicker and more robust single-mode tapered waveguide to be used in biosensing experiments where flow (or collisions between the resonator and taper that result from flow)

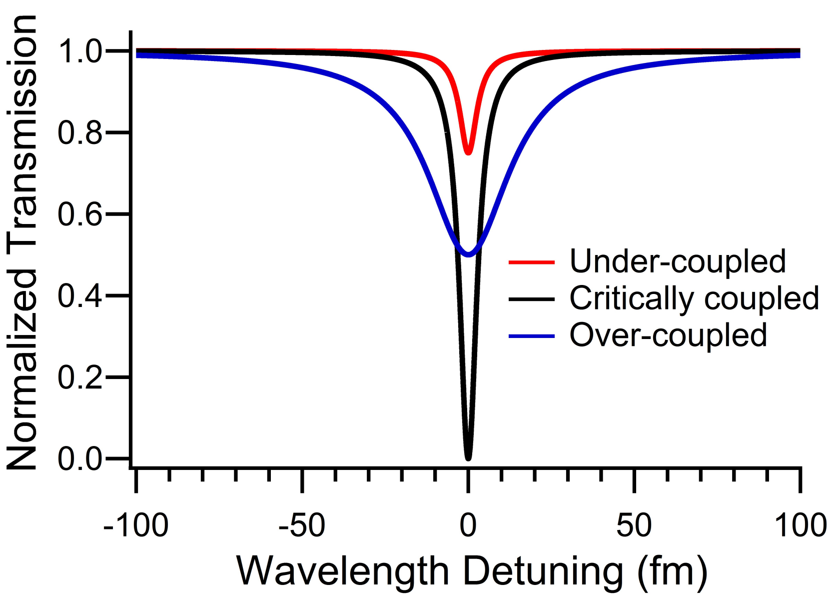

Figure 3.10: Typical transmission profiles illustrating the under-coupled, critically-coupled and over-coupled regimes.

may break the taper.

The overlap of the evanescent field of the waveguide with the resonant mode of the cavity determines how much light is coupled into the device. This coupling efficiency can be tuned through control of the distance separating the waveguide and resonator. Three regimes of coupling behavior are apparent when manipulating that spacing, l_{coup}, which are demonstrated in Fig. 3.10 and described here:

Under-coupled Regime: When $l_{coup} \approx \lambda$, very little of the evanescent wave overlaps the resonant mode of the cavity and P_C is small. Decreasing this gap will couple more light into the resonator until scattering losses due the presence of the waveguide approach those of the limiting loss mechanism. This is the best regime for determining Q_{tot} so that it reflects the loss mechanisms intrinsic to the resonator.

Critical Coupling: The point at which Q_{ext} becomes the limiting factor in Eq. (3.14) due to scattering of resonant light by the waveguide. Transmission through a perfect, single-mode taper is zero as all light is coupled into the resonator.

Over-coupled Regime: Decreasing the gap between the waveguide and the resonator only decreases the amount of light getting into the mode because more and more is being lost to scattering by waveguide. Q_{tot} is dominated by Q_{ext}.

3.6 Nonlinear Effects in WGM Resonators

The ability to make resonators with quality factors as high as $Q = 6.3 \times 10^{10}$ [91] while confining the mode into such small volumes makes WGM optical devices perfectly suited to explore nonlinear phenomena in materials. Several well-known second-order effects (i.e., their contribution to the polarization of the medium depends on the electric field magnitude squared, $|\mathbf{E}|^2$), such as second harmonic generation and optical parametric amplification/oscillation may be observed in materials exposed to sufficiently large electric fields. Though fewer in number, some third order phenomena such as the Kerr effect and optical limiting may also be observed. The nonlinear phenomena that play the most prominent role in the present work are discussed in detail in Chapter 5. Fig. 3.11 depicts how these effects manifest themselves in a typical transmission spectrum for a resonant mode.

Of particular importance in studying the WGM biosensor response is the thermo-optical effect. This phenomenon occurs in most materials and applies to how the refractive index defined in Eq. (3.1) varies with temperature according to the thermo-optical coefficient $\frac{dn}{dT}$. The small amount of optical energy absorbed by the silica in a resonator is dissipated as heat because no radiative relaxation (e.g., fluorescence) is available to it. For silica, $\frac{dn}{dT} = 1.3 \times 10^{-5}\,\mathrm{K}^{-1}$ and warming produces an increase in the refractive index. Eq. (3.10) suggests that any increase in the effective refractive index n_{eff} will produce a red shift ($\Delta\lambda > 0$). Transmission spectra are transient measurements collected as the wavelength is scanned and light is coupled into the resonator.

As the instantaneous output of the scanned laser approaches the resonant wavelength λ_R and light is coupled into the mode, the heat generated by absorption increases the cavity temperature and the resonant wavelength shifts. The transmission curve changes from a symmetrical Lorentzian shape to an asymmetrical sharkfin-like shape, with an artificially wide trough observed while $\frac{d\lambda}{dt} > 0$ and an artificially narrow one

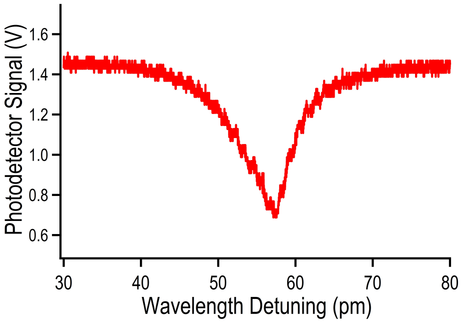

(a) Thermal Broadening

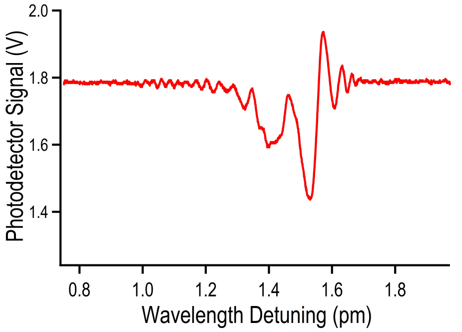

(b) Opto-mechanial Oscillations

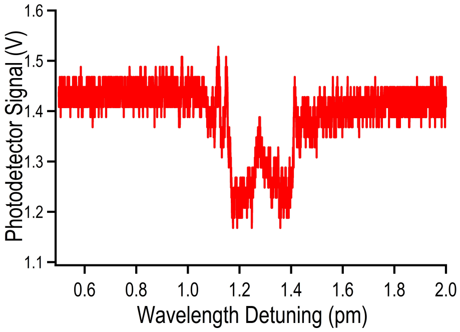

(c) Resonance Splitting

Figure 3.11: Nonlinear effects observed while coupling into WGM resonators. (a) Asymmetrical transmission trough for a 150 μm microdisk excited with 1310 nm light. (b) Opto-mechanical oscillations as the momentum of propagating light excites mechanical vibration modes in a microtoroidal resonator excited with 1540 nm light. (c) A split resonance peak as backscattering in the cavity can break the degeneracy of counter propagating modes in a microtoroidal resonator excited with 1310 nm light

when $\frac{d\lambda}{dt} < 0$. This effect is demonstrated in Fig. 3.11a. The thermo-optical effect is greater detail in Chapter 5. This thermal broadening effect can be managed by using low coupled power, but eliminating absorption by the bulk materials is impossible for near-infrared light in water or visible light in silica.

Another nonlinear effect involves mechanical feedback that results from the momentum of the resonant light [92, 93, 94]. Circulating photons can apply enough force at certain frequencies to excite vibrational modes in microdisks and microtoroids supported on silicon pedestals. Since coupling into the resonator is sensitive to the relative position of the cavity and the waveguide, any mechanical oscillations directly effect the coupling. Fig. 3.11b illustrates this phenomena and how coupling more light during the wavelength sweep increases the amplitude of mechanical oscillation and distorts the transmission trough.

A third nonlinear phenomena that appears often when working with high-Q WGM optical resonators ($Q > 10^7$) involves what are called split peaks. When inhomogeneities in or on the resonator are efficient enough at scattering light backwards, the counter-propagating mode is excited. The two modes have a different resonant wavelengths because their path lengths vary slightly due to the backscattering, resulting in a transmission profile that features two local minima rather than the single Lorentzian trough observed in the absence of this effect (see Fig. 3.11c). Since the magnitude of the backscattered wave is determined by the size and number of inhomogeneities present, the mode splitting can be used to report the quantity of material as well as the nature (e.g., size, refractive index, geometry) of that inhomogeneity. This effect has been described [95] and demonstrated [96] elsewhere. This phenomena is only observed in sufficiently high-quality resonators because there is a threshold circulating power required to sustain resonance in the counter-propagating direction, and those powers are attainable with quality factors of $Q > 10^7$.

3.7 Sensing with WGM Resonators

WGM sensing experiments are carried out by monitoring the resonant wavelength as analyte solution is introduced to the sensor. This process involves enclosing the resonator and waveguide inside a flow cell while scanning through wavelength space and capturing transmission spectra. The apparatus used for this measurement is shown in Fig. 3.12, and the flow cell configuration used for the experiments in the present work is depicted in Fig. 3.13. The flow cell is constructed on the end of a stainless steel sample holder that may be fixed to a positioning system. Manipulation of the gap between the resonator and the waveguide is performed by keeping the tapered optical fiber waveguide immobile while moving the resonator and the flow cell into which it is incorporated. A range of motion of roughly 25 mm is usually required to test multiple resonators defined on a single chip in search of the mode with the highest Q, but great precision is also required to control the light coupled into the device. This difficult combination is achieved by attaching a 3-dimensional piezo positioning system (range of motion 100 μm) to a 3-dimensional translation stage (range of motion 25 mm).

Cameras with microscope objectives are positioned to give a top and side view of the waveguide and resonator, with lamp light coupled down the optical axis of these camera systems to provide sufficient illumination. The top view provides useful feedback during the positioning of the resonator, but ultimately the power coupled into the cavity provides the most precise information about how close the device is to the waveguide. The relative coupled power as well as the instantaneous λ_R may be read from the transmission spectrum data sent from a low-noise photodetector to an oscilloscope. The side view camera enables the planar alignment of the waveguide and the resonator, which is extremely important for toroidal devices because they do not support non-equatorial modes. This entire apparatus, with exception to the oscilloscope, is enclosed in a box to limit environmental effects on the system. Fig. 3.14 shows a top view image of a toroid and tapered optical fiber waveguide in far-field illumination as well as one illuminated only by the light coupled into the device. Notice the striation-like defects in the toroid visible in Fig. 3.14b.

The external cavity laser is scanned by sending it a customized triangular function from a waveform generator. The oscilloscope that receives the data from the photodetector reports the total power to the diode as a function of time, which may then be converted to wavelength with knowledge of the triangular waveform characteristics. Programs were written in both LabVIEW and Igor to be run on a computer in order to query and retrieve data from the oscilloscope. The scanning of the excitation laser underscores the transient nature of this measure. More detail about the experimental method behind WGM optical biosensor

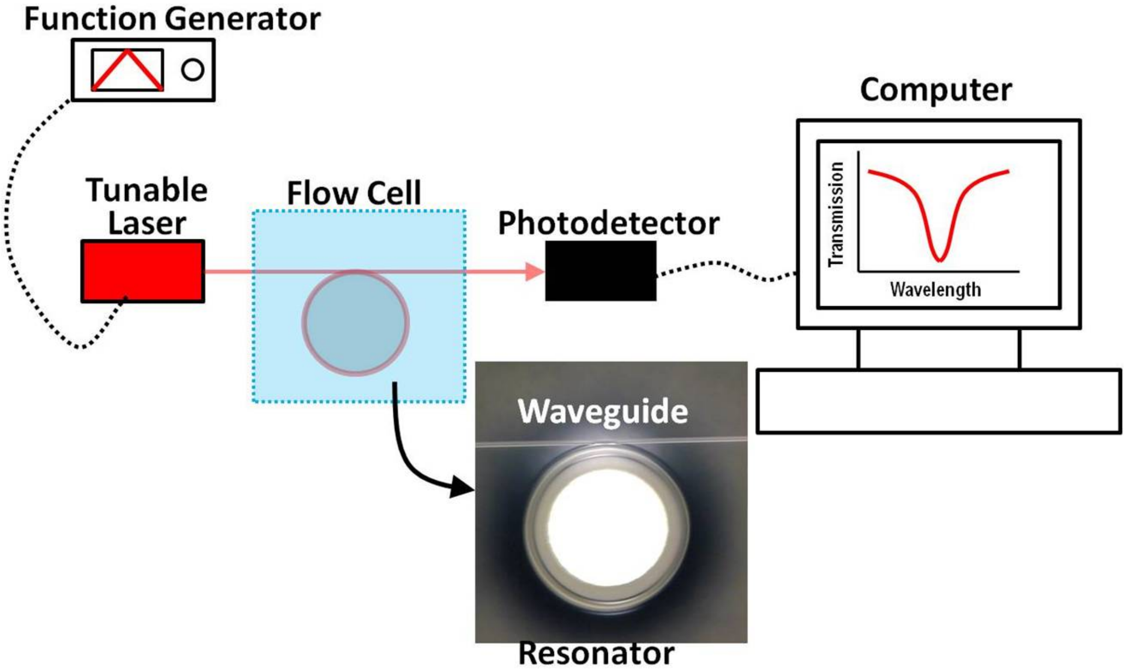

Figure 3.12: The WGM sensing experimental apparatus, featuring a tunable laser, tapered optical fiber wavguide, resonator, detector and data capture/processing computer. A function generator is used to sweep linearly through wavelength space so that a transmission spectrum may be used to locate the center of the resonance peak or determine the Q of the resonance.

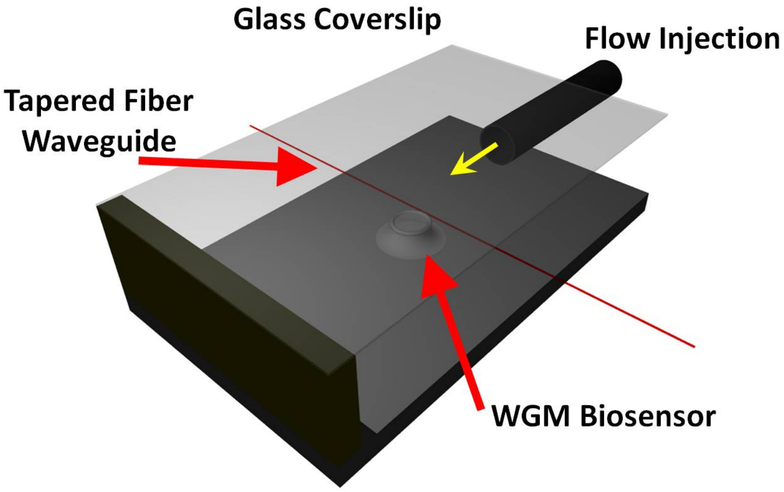

Figure 3.13: The flow cell used in WGM biosensor experiments, shown with a microtoroidal resonator and tapered optical fiber.

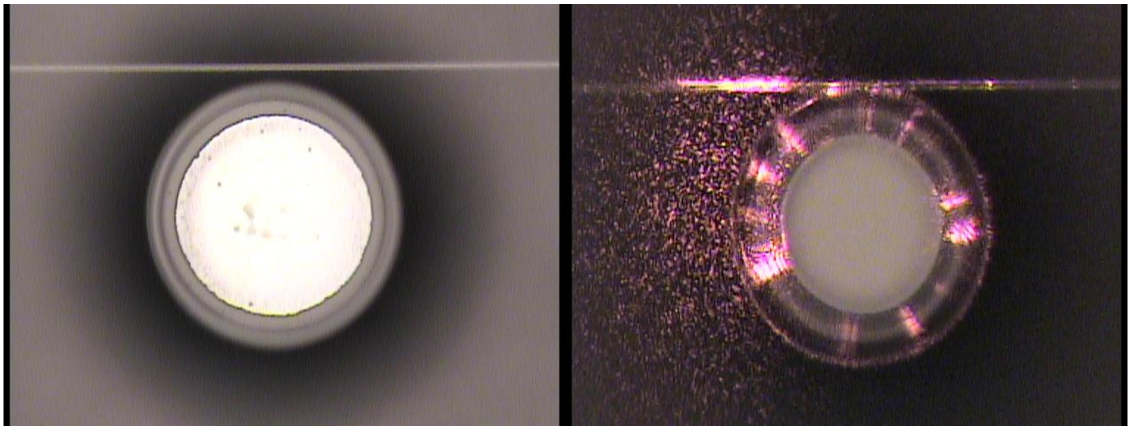

(a) (b)

Figure 3.14: Using a tapered optical fiber waveguide to couple light into a toroid. (a) A view showing the two in proximity to one another. (b) A low-quality toroidal WGM resonator ($Q \approx 10^2$) scattering light out of the cavity.

experiments as well as a thorough discussion of the role that transient behavior plays in the interpretation of these results is included in Chapter 5.

The processing of data involves determining the location of the resonance based on each captured transmission spectrum. As discussed above, nonlinear effects like thermal broadening can complicate the process of finding the resonant wavelength from this spectrum because it changes with the temperature of the resonator. In this case, the minimum may be an effective measure of the resonance location, assuming that the material that adsorbs to the sensor during the experiment does not significantly perturb the shape of that trough. For low-P_C conditions, however, the trough will be well described by a Lorentzian function that may be determined through curve fitting. A study of this data processing step revealed that a curve fit, though time consuming considering the typical time resolution of the measurement that generates a single scan for every 0.5–1 s, does a better job of preserving small features in the data than applying a smoothing function and determining the minimum of the curve.

Chapter 4

Flow-Enhanced Transient Response in Whispering Gallery Mode Biosensors

4.1 Abstract

Whispering gallery mode (WGM) optical resonator sensors are an extremely sensitive label-free technology for detecting the binding of biomolecules in solution. To better understand the fast transient response observed with these devices, we model mass transfer to spherical and toroidal WGM sensors of identical outer radius. Finite element simulations predict a 3-10 fold higher binding frequency for toroidal sensors. These results agree to within an order of magnitude with experimental data from the literature and suggest a design strategy to improve the transient response of a sensor by making the device small only in the dimension that governs boundary layer development.

4.2 Introduction

Whispering-gallery mode (WGM) optical microcavities [60, 61] are a promising label-free sensing technology that may one day be the basis for high-sensitivity diagnostic and analytical tools capable of detecting biomolecules in complex biological fluids. Recent data demonstrating single-molecule limits of detection [1] have stimulated a debate [97] over the physical processes that enable such a sensitive response when a biomolecule adsorbs to a WGM resonator and interacts with the resonant light. The data published by

Armani and colleagues [1] are extraordinary because of both their sensitivity and the fast response observed, with the latter exceeding the approximate binding rates obtained with mass transfer calculations [98]. The present work examines mass transfer to non-planar, WGM sensors in flow cells, demonstrating how fluid flow and resonator geometry affect the transient sensor response.

The microscale size (i.e., outer diameter $< 100\mu\mathrm{m}$) of the WGM sensor, though useful for limiting the amount of sample required, poses a challenge for sample delivery at low concentrations: the overall analyte binding rate is limited by the small surface area. Both the time to achieve a given level of binding during an experiment and the amount of valuable sample required can be reduced by using convection. Some WGM sensor embodiments, like the liquid-core optofluidic ring resonator (OFRR) [99], have their own integrated flow systems. Microfluidic flow cells [30] have also emerged as a popular delivery system due to their small volumes and ease of fabrication, but integration into WGM sensing systems has, understandably, received limited attention in the face of the pressing need for further characterization of basic device performance.

4.3 Boundary Layers

To enable high sensitivity analysis, the flow system must deliver the few analyte molecules in a dilute sample to the sensor as efficiently as possible. The flux of material to the surface of the sensor, $\mathbf{j}_{\mathrm{surf}}$, depends on the concentration gradient evaluated at the surface through Fick's Law, i.e., $\mathbf{j}_{\mathrm{surf}} = -D\nabla c|_{surf}$, where D is the diffusion coefficient. In a quiescent fluid, the gradient scales as $(c|_{surf} - c_\infty)/\ell_s$, where ℓ_s is the characteristic dimension of the sensor. Identifying ℓ_s is obvious for a sphere which has a single dimension, but it is more challenging for the toroid which has two. Flow can limit the extent of the concentration gradient to a thin region of thickness δ at the surface of an object (see Figure 4.1). This so-called *boundary layer* increases the magnitude of the gradient that drives diffusion of the analyte to the sensor and, thereby, enhances the flux.

Squires and colleagues provide an excellent introduction to boundary layer effects in planar sensor performance [98], and develop intuitive relationships between experimental flow parameters and the transient response of those sensors. Their analysis is framed in terms of the Péclet number, a dimensionless group that

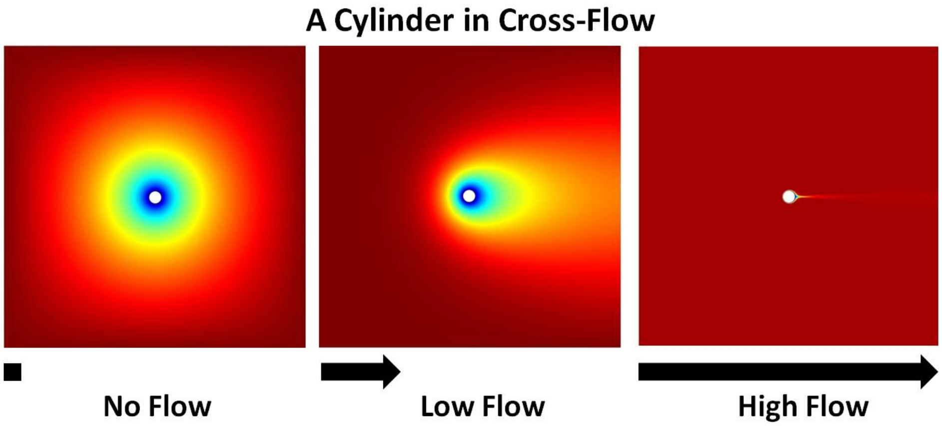

Figure 4.1: Concentration profiles for mass transfer to a cylinder in cross section under various flow conditions. Red denotes a normalized concentration of 1, and Blue denotes a normalized concentration of 0. (a) Diffusion alone delivers the species to the cylinder isotropically. (b) At low upstream flow velocity, an asymmetric concentration distribution forms, with an extended boundary layer in the wake of the cylinder. (c) At high upstream flow velocity, the boundary layer is thin and the concentration gradient remains asymmetric and is confined to a narrow region around the cylinder.

describes the ratio of advective to diffusive timescales, $\mathrm{Pe} = \frac{Ud}{D}$, where U is the inlet flow velocity and d is the critical length scale of the flow obstacle (i.e., sensor diameter). Large values of Pe indicate that advection is dominant and boundary layers are thin. The insights gained in that study provide guidance for understanding the parameters that govern the transient response of non-planar, WGM sensors. The convenient planar, half-sphere, and half-cylinder geometries have been considered elsewhere [100], but ultra-high quality factor WGM sensors and other structures supported on a pedestal have received less attention. For example, these methods are appropriate for nanowire devices [39] that sit on a surface, but they fail to capture the full boundary layer development that occurs for 3-dimensional objects, like the spherical or toroidal sensors, that are removed from the slow-flow region near a substrate.

Mass transport to a small target in flow has been studied extensively in the context of filtration [101], providing a starting point in our effort to analyze flow effects on WGM sensor performance. For our purposes, the biomolecules may be treated as small (< 5 nm diameter) particles undergoing both advection and diffusion. Filtration has traditionally been modeled by considering spheres and cylinders exposed to a uniform upstream flow [101] in an effort to estimate the efficiency with which the filter element will remove particles from the fluid stream. These studies have established how boundary layers that develop around objects in flow play a critical role in the particle capture process. Convection dominates mass transport far from the object, but the “no slip" boundary condition and the strong adsorption reaction cause both the velocity and the concentration to fall sharply in the boundary layer, where diffusion dominates instead. A typical concentration boundary layer is shown in Fig. 4.2 (inset) for flow around a sphere.

Here we develop a full 3-dimensional model for both spherical and toroidal microresonators using representative dimensions inspired by experimental studies [85, 1]. Specifically, we model a spherical resonator of radius $r_{sphere} = 42.5\,\mu$m and toroidal resonator of major and minor radii $r_a = 40\,\mu$m and $r_i = 2.5\,\mu$m, respectively, so that the two geometries have equal outer radii. In the absence of convenient analytical expressions or approximations like those for the flow fields surrounding spheres and cylinders, the most effective method for solving the momentum balance and continuity equations (i.e., the Navier Stokes equations) for laminar flow around a toroid is to use numerical techniques. Here we use COMSOL Multiphysics, a commercially available finite element (FE) solver, to calculate the velocity and concentration profiles as well as the flux of analyte at the reactor surface. We assume that the fluid is water, and that the inlet has a uniform flow rate (i.e., a flat velocity profile). The concentration of analyte is taken to be 1 fM, and we assume that the system is at steady state. We also assume that the surface binding reaction by the analyte is instantaneous and irreversible, an assumption valid early in the transient measurement when there is insignificant depletion of analyte in the bulk and the vast majority of binding sites on the sensor surface are unoccupied. As a matter of practice, we verified both that the mesh elements used in the FE approximation were sufficiently small to ensure that the mesh size did not impact the accuracy of the calculation (see supplemental information), and that the overall geometry dimensions were large enough that wall effects in the enclosure did not influence the results.

To validate the results of our FE model, we examined the flow around a single spherical resonator of outer radius $r_a = 42.5\,\mu$m. Figure 4.2 shows that these calculations are capable of reproducing the boundary layer depth δ_{95} scaling relationships predicted by Levich [102] and elsewhere [98], where δ_{95} is determined by the distance from the surface of the object at its most upstream point where the concentration reaches

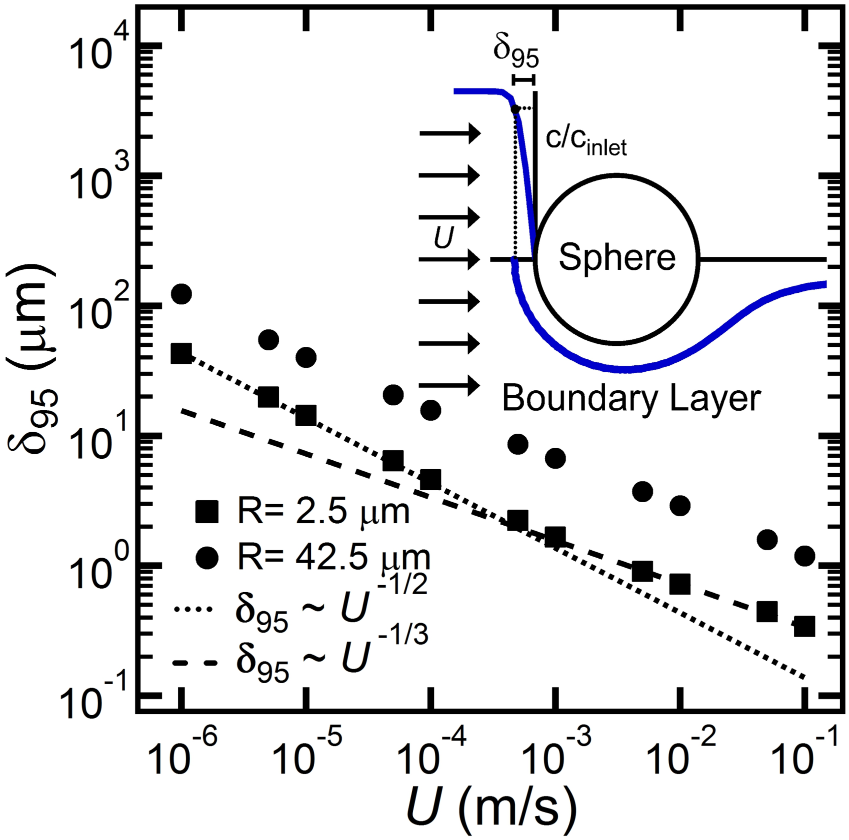

Figure 4.2: Upstream boundary layer thickness δ_{95} as a function of inlet flow velocity for spheres of radius 42.5 μm (circles) and 2.5 μm (squares) with predicted scaling laws at high (blue) and low (red) flow velocity limits. The inset graph depicts how δ_{95} is determined.

95% of the bulk value. Specifically, a small inlet flow velocity, U, yields a boundary layer large compared to the object and that scales with the velocity as $\delta_{95} \sim U^{-\frac{1}{2}}$, but a high inlet flow velocity produces a thinner boundary layer that scales as $\delta_{95} \sim U^{-\frac{1}{3}}$. That these simulations exhibit the predicted asymptotic behavior allows us to proceed with confidence that our model captures the relevant physics.

WGM sensors only yield a signal when biomolecules adsorb where the evanescent field is sufficiently strong, which we take to be $> 10\%$ of the peak mode intensity on the resonator surface. The fraction of this surface where sensing occurs was determined by mode simulations in spherical and toroidal resonators that were performed using the methods presented by Oxborrow [103]. Due to mode compression imposed by the minor radius of the toroid, the effective area for the toroids considered here is $\approx 50\%$ of that for a sphere of

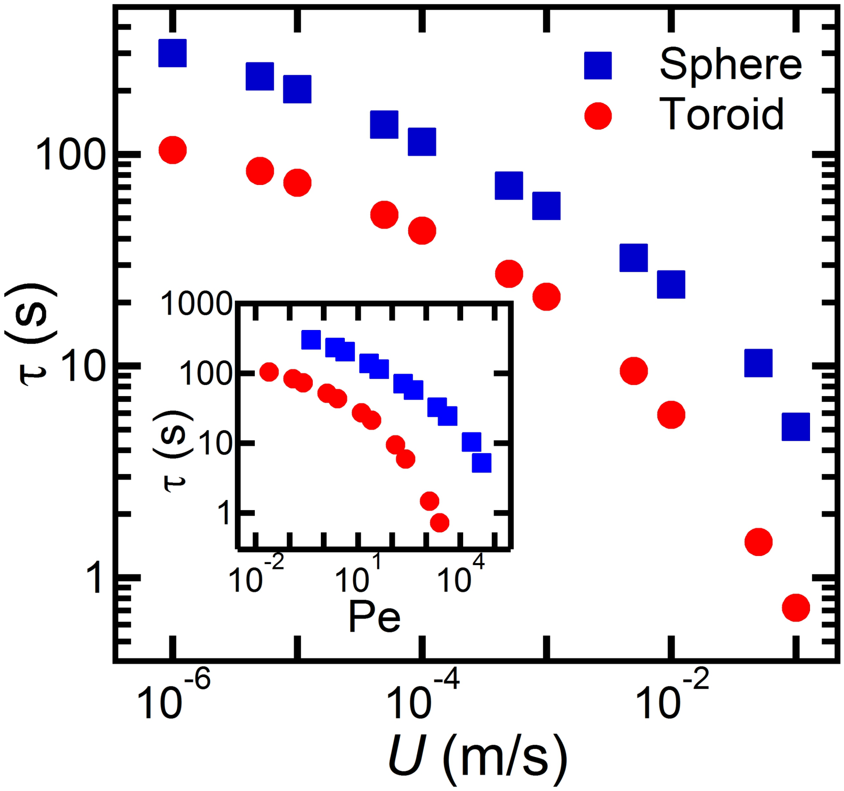

Figure 4.3: Time between binding events, τ, for 1 fM analyte concentration solution introduced to toroidal (circles) and spherical (squares) WGM sensors. (inset) τ recast as a function of sensor Péclet number.

similar major radius (see Section 4.4). We calculate the mean time delay between single-molecule binding events, τ, by integrating the flux over the entire sensing surface and inverting this binding rate.

Despite the somewhat smaller available surface area for interactions with bound material, our model predicts more frequent binding events on a toroidal WGM biosensor than on a spherical one with identical outer radius for all inlet flow velocities studied (Fig. 4.3). The range of accessible flow rates is bounded at low velocity by the ability of most syringe pumps to provide steady, non-pulsatile flow and, at high velocity by the onset of the laminar-turbulent transition regime where the present laminar-flow model is no longer applicable. The different boundary layers that develop around the major and minor diameters of the toroidal resonator lead to consistently shorter response times than those for spheres. In the case of the toroid, the small minor radius thins the boundary layer as did small sphere size in the results shown in

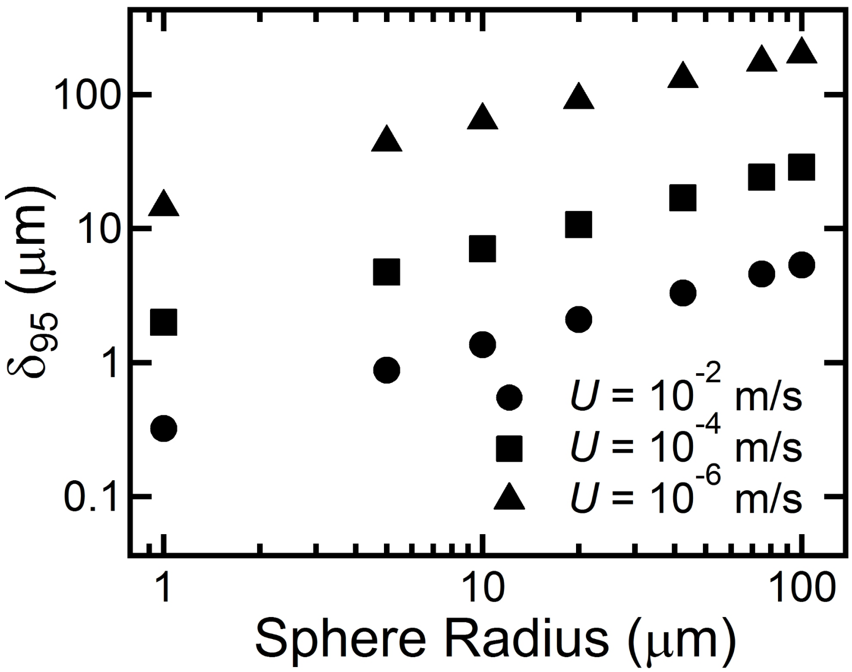

Figure 4.4: The effect of sphere radius on δ_{95} for varying inlet flow velocities, calculated using the same model as in Fig. 4.2.

Fig. 4.4, enhancing the surface flux over that for a sphere with the same outer radius. The toroid experiences a higher binding rate because the increase in analyte flux to the sensor far outweighs the decrease of effective sensing area relative to a sphere.

Toroidal WGM resonators reject many of the non-azimuthal modes that spherical devices exhibit [82]. It is now clear that they offer an additional advantage over spherical sensors because of their enhanced transient response. For inlet flow velocities relevant to the experiments ($U \approx 10^{-2}$m/s) [2], toroids yield 3–10 times more frequent binding events than do spherical devices of similar size. This may explain, at least in part, why single-molecule binding events have been observed only with the former geometry to date.

In Fig. 4.5 we compare the model predictions for τ at various concentrations to single-molecule sensing data gathered with a toroidal WGM sensor by Armani and colleagues [1]. Our simulations of a toroidal device agree with these experimental data to within an order of magnitude, while those for a spherical sensor poorly describe these data (inset). Refinement of the computational model may further reduce these discrepancies. In particular, we leave for future work the incorporation of the chip from which the toroids

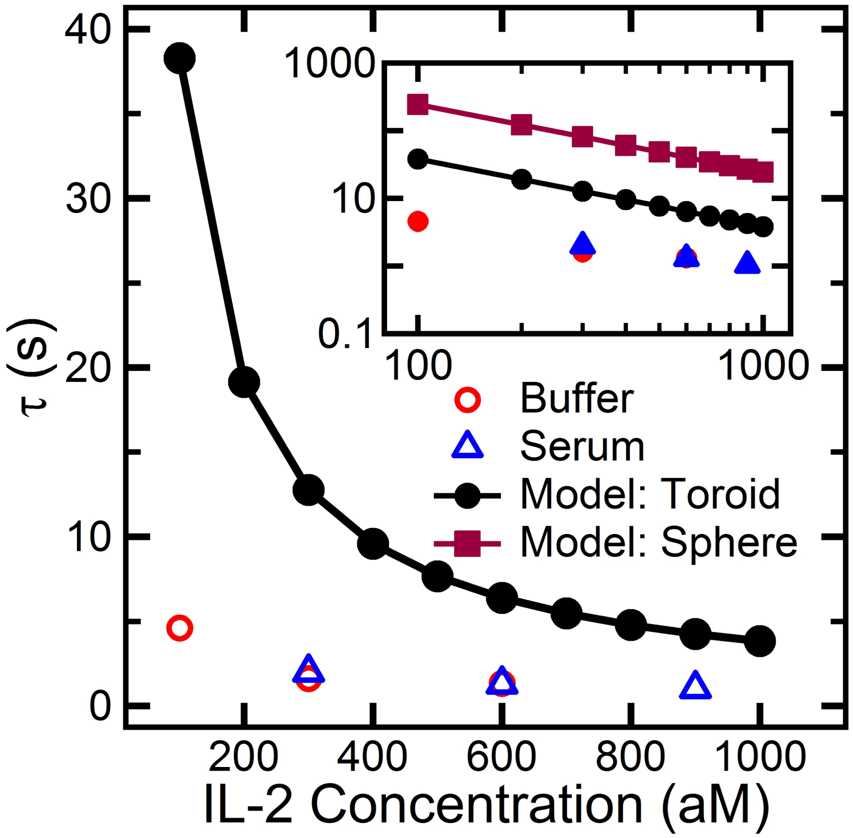

Figure 4.5: Modeled results for τ at a range of concentrations for Interleukin-2 with $U = 10^{-2}$ compared to experimental data published by Armani et al. [1, 2] collected in buffer (circle) and bovine blood serum (triangle).

are fabricated into the simulated geometry as well as a consideration of equilibrium binding of analyte to the functionalized device.

This study uses a finite element computational model to investigate mass transfer to spherical and toroidal WGM optical biosensors in flow. The thickness of boundary layers that develop around these devices determine the flux of analyte to the surface and, consequently, the transient signal of the sensor. Our simulations show that the minor diameter of a toroidal device produces a thinner boundary layer than for a sphere of identical outer radius, allowing the toroid to experience more frequent binding events. These results support experimental observation in the literature [1] and illuminate a strategy that may be broadly applied to sensor design that will result in a more rapid transient device response. Making the sensor small only in the dimension that governs boundary layer development simultaneously maximizes both surface flux of analyte and the effective sensing area of the device.

This work was supported by funding from the Jacobs Institute for Molecular Engineering for Medicine at the California Institute of Technology.

4.4 Supplemental Information

Numerical Solutions

Calculating the rate at which a species reaches the sensor surface involves solving the momentum and continuity differential equations to describe fluid flow (e.g., the Navier-Stokes equations) as well as solving the conservation of mass equation, which requires knowledge of the flow velocity field. For a single species with concentration, C_i, in an incompressible Newtonian fluid, these equations are expressed as

$$\rho\Big(\frac{\partial \mathbf{u}}{\partial t} + \mathbf{u}\cdot\nabla\mathbf{u}\Big) = -\nabla p + \mu\nabla^2\mathbf{u} \tag{4.1}$$

$$\nabla\cdot\mathbf{u} = 0 \tag{4.2}$$

$$\frac{\partial C_i}{\partial t} + C_i\nabla\mathbf{u} = D\nabla^2 C_i \tag{4.3}$$

where ρ is the fluid density, $\mathbf{u}$ is the velocity, p is the pressure, μ is the viscosity, and D is the diffusion coefficient.

We use a commercially available finite element (FE) solver, COMSOL Multiphysics 4.1, to solve this system of equations on a server with 32 64-bit AMD processors and 256 GB DDR-2 RAM. The FE method involves breaking the geometry over which the equations apply (i.e., the "flow cell") into small tetrahedral volumes and applying boundary conditions at each face of an element. This powerful method allows the user to focus computation power on parts of the geometry where the solution varies most strongly with position by locally controlling element size. Elements at the edge of the volume experience the macro-scale boundary conditions commonly imposed when solving differential equations analytically, while those in the interior experience a "continuity boundary condition" that applies to the dependent variables as well as their derivatives.

Figure 5.7 shows the flow cell used for the present work, comprising a rectangular flow cell with a symmetry plane that bisects both the cell as well as the sensor. This half cell is 2.5 mm in the flow direction, and 1.5 mm x 1.5 mm in cross section (3 mm wide by 1.5 mm tall for the full cell). These dimensions were determined to be sufficiently large that increasing them led to less than 1% change in integrated analyte adsorption rates to the sensor for all flow rates considered here.

The sensor surface features a "no-slip" boundary condition typical of solid walls and the analyte is assumed to adsorb instantaneously there. Figure 4.7 shows additional boundary conditions. We assume a flat profile for the inlet flow velocity, U_{inlet}, and an inlet analyte concentration of $C_{inlet} = 1$ fM. The top, bottom, and side boundaries are given "no-slip" and "no flux" conditions, while the flow outlet is set to atmospheric pressure $p_0 = 101{,}325$ Pa. The diffusion coefficient of Interleukin-2 (IL2, Mw 15.5 kDa) was approximated to be$D \approx 10^{-10}\mathrm{m}^2/\mathrm{s}$ [104].

The array of elements used in an FE solver is called the *mesh*, and its design can significantly impact the accuracy of the mathematical solution. A balance must be struck between making the mesh elements small enough to capture local changes in dependent variables and making them prohibitively small that the computer has insufficient resources to find a solution. We evaluate the dependence of our results on surface mesh element size, l_{mesh}, by studying flow around a spherical sensor of radius $R_{sphere} = 42.5\,\mu$m and $U_{inlet} = 0.01$ m/s. We set l_{mesh} to be a maximum of R_{sphere}/N and calculate the steady-state binding rate to the entire sensor surface. These data are reported in Fig. 4.8 as a relative binding rate with respect to that calculated for the case $N = 500$ where

$$\Phi_{N=500} = \frac{\mathrm{Bindingratefor}N}{\mathrm{Bindingratefor}N = 500}. \tag{4.4}$$

This limiting condition ($N = 500$) represents the mesh size beyond which solutions take prohibitively long to converge. The value of $\Phi_{N=500}$ is greater than 0.98 for N $>$ 80, indicating an acceptable 2% relative error. Therefore, we set the surface mesh size in all models for the current work as 1/80 of the critical dimension (R_{sphere} for a sphere and r_{minor} for a toroid).

While analyte is assumed to adsorb to the entire surface of the resonator, only a fraction of that surface is effective for sensing. COMSOL solutions for the mode in a spherical and toroidal WGM resonator, calculated using methods described by Oxborrow [103], were used to identify the functional region of the sensor defined by where the mode intensity at the resonator surface is >10% of the surface maximum. These results are shown in Fig. 4.9. The effective mode height for the toroid modeled here ($h_{mode} = 2.84\,\mu$m) is less than half that for a sphere of identical outer radius ($h_{mode} = 6.00\,\mu$m) due to mode compression by the minor radius of the toroid.

Single-Molecule Binding Data

We compare the predictions of our model with single-molecule binding data observed experimentally by Armani and colleagues [1]. Those data are transient measurements monitoring the resonant wavelength, λ_R , of the mode as interleukin-2 binds to the resonator, which has been functionalized with anti-IL2. The sensor exhibits a step-wise response in λ_R for a range of IL2 concentrations regardless of whether buffer or bovine blood serum was used as the solvent. The experimental data included in Fig. 4.5 represents the average time between binding events detected during the first 60 seconds of the experiment. This time window was chosen in accordance with the assumptions made in the computational model. A step was defined as any time $|\Delta\lambda_R| > 2\sigma$, where σ is the noise of the signal in λ_R within a single step and averaged over the first five steps in an experiment. Typical values of σ were between 0.15 fm (0.15× 10-15 M) and 0.25 fm.

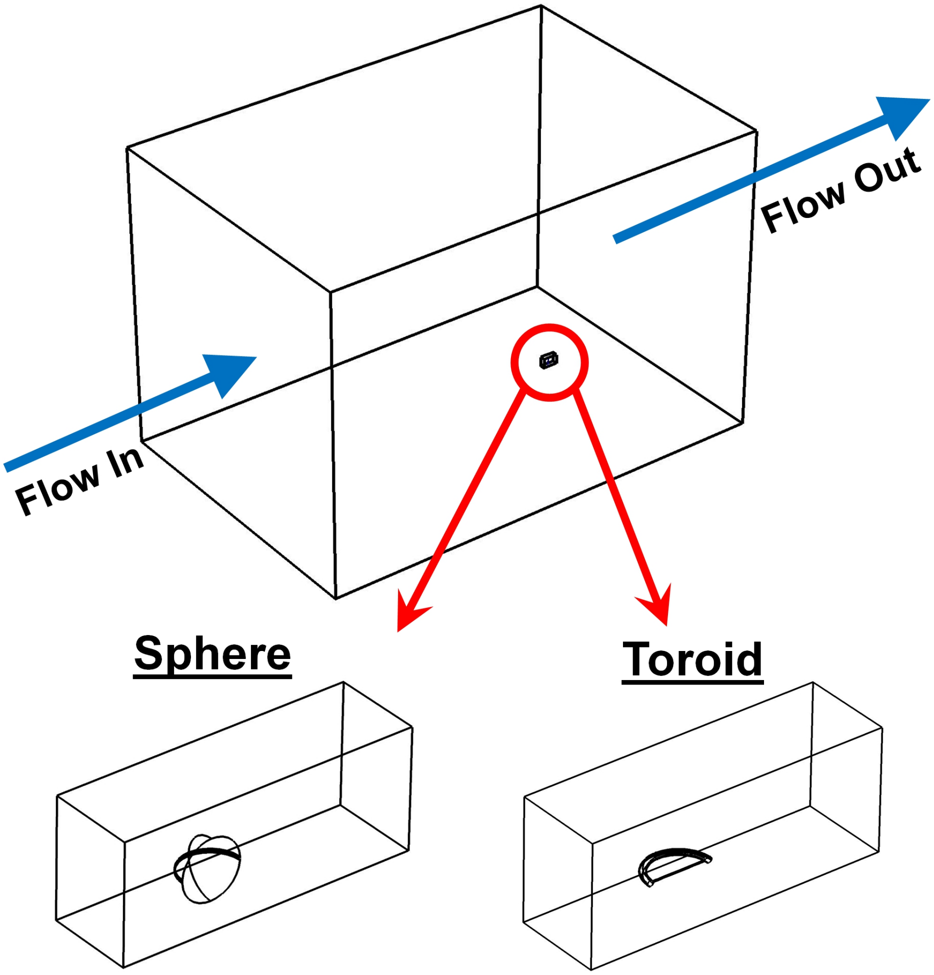

Figure 4.6: Flow cell geometry used in COMSOL Multiphysics simulation of flow around a WGM sensor. The near plane is a symmetry plane that bisects the cell and the resonator. The sensors are cut out of the cell, and their surfaces feature no-slip flow and $C_i = 0$ (i.e., instantaneous surface reaction) boundary conditions.

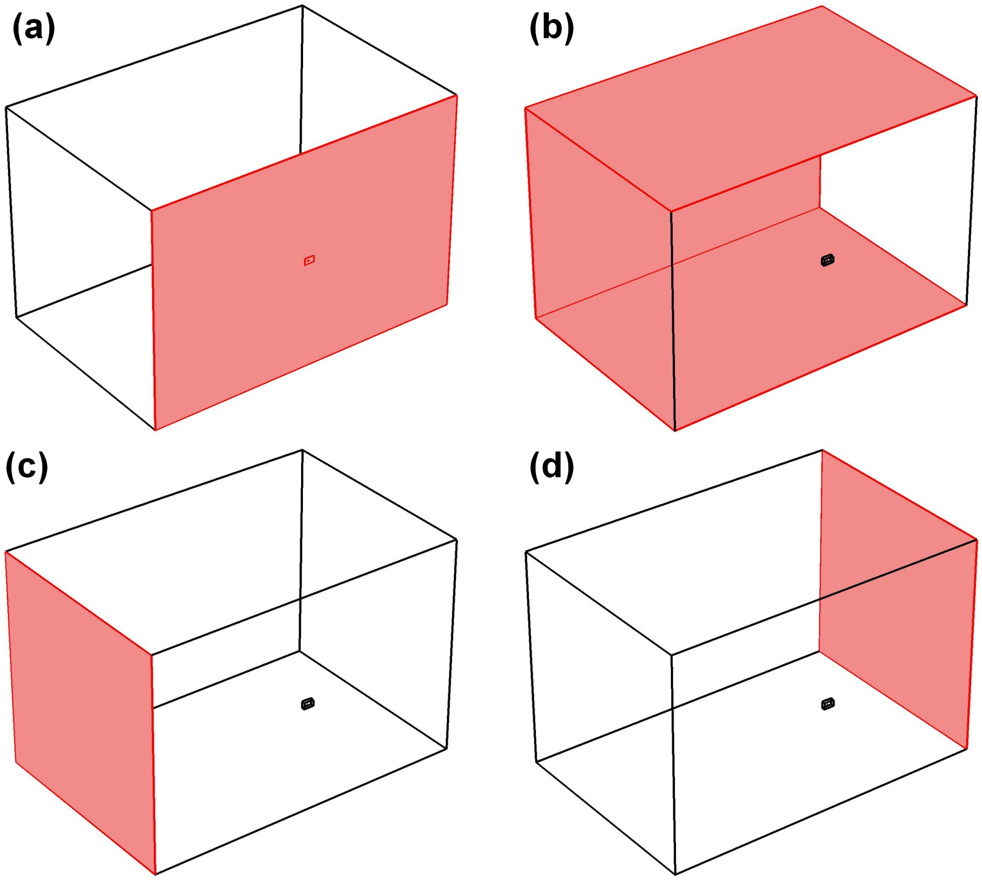

Figure 4.7: Flow cell boundary conditions used in COMSOL Multiphysics simulations of flow around WGM sensors. (a) Symmetry plane. (b) “No-slip" and “no flux" conditions. (c) Uniform flow inlet velocity $U = U_{inlet}$ and inlet concentration $C_{inlet} = 1$ fM. (d) Flow outlet at pressure $p_0 = 101{,}325$ Pa.

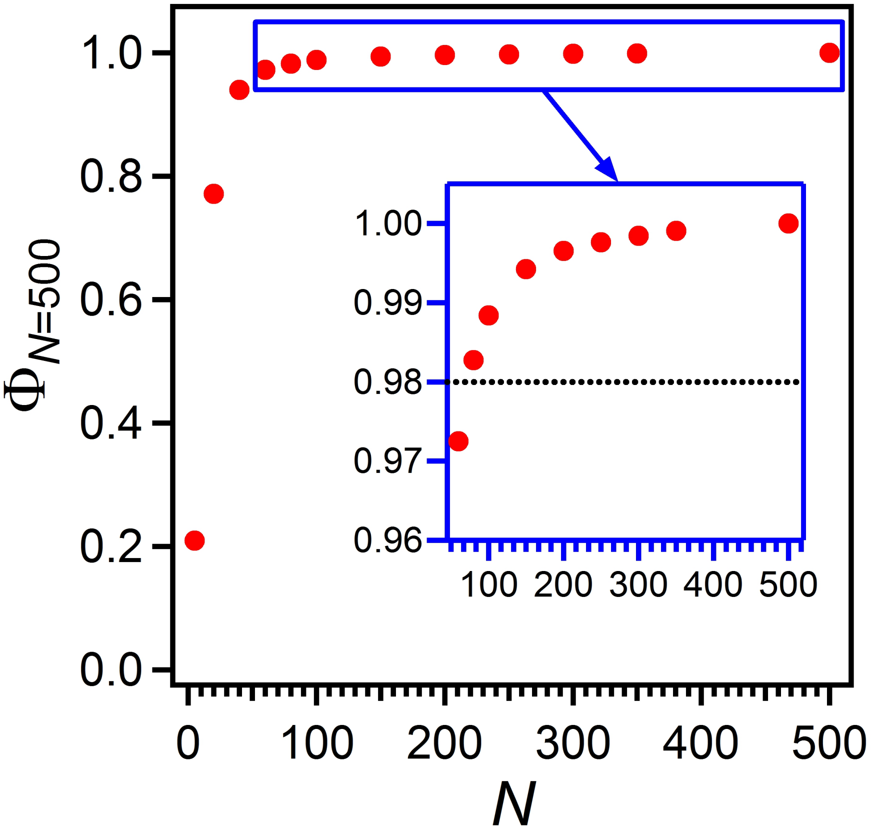

Figure 4.8: The relative surface binding rate to a sphere with $R_{sphere} = 42.5\,\mu m$ and $U_{inlet} = 0.01$ m/s as a function of the surface mesh element size ($l_{mesh} = R_{sphere}/N$), calculated with respect to the case $N = 500$ ($l_{mesh} = 85$ nm). This quantity converges with increasing N and achieves a relative error of less than 2% for N $>$ 80 (see inset for detail).

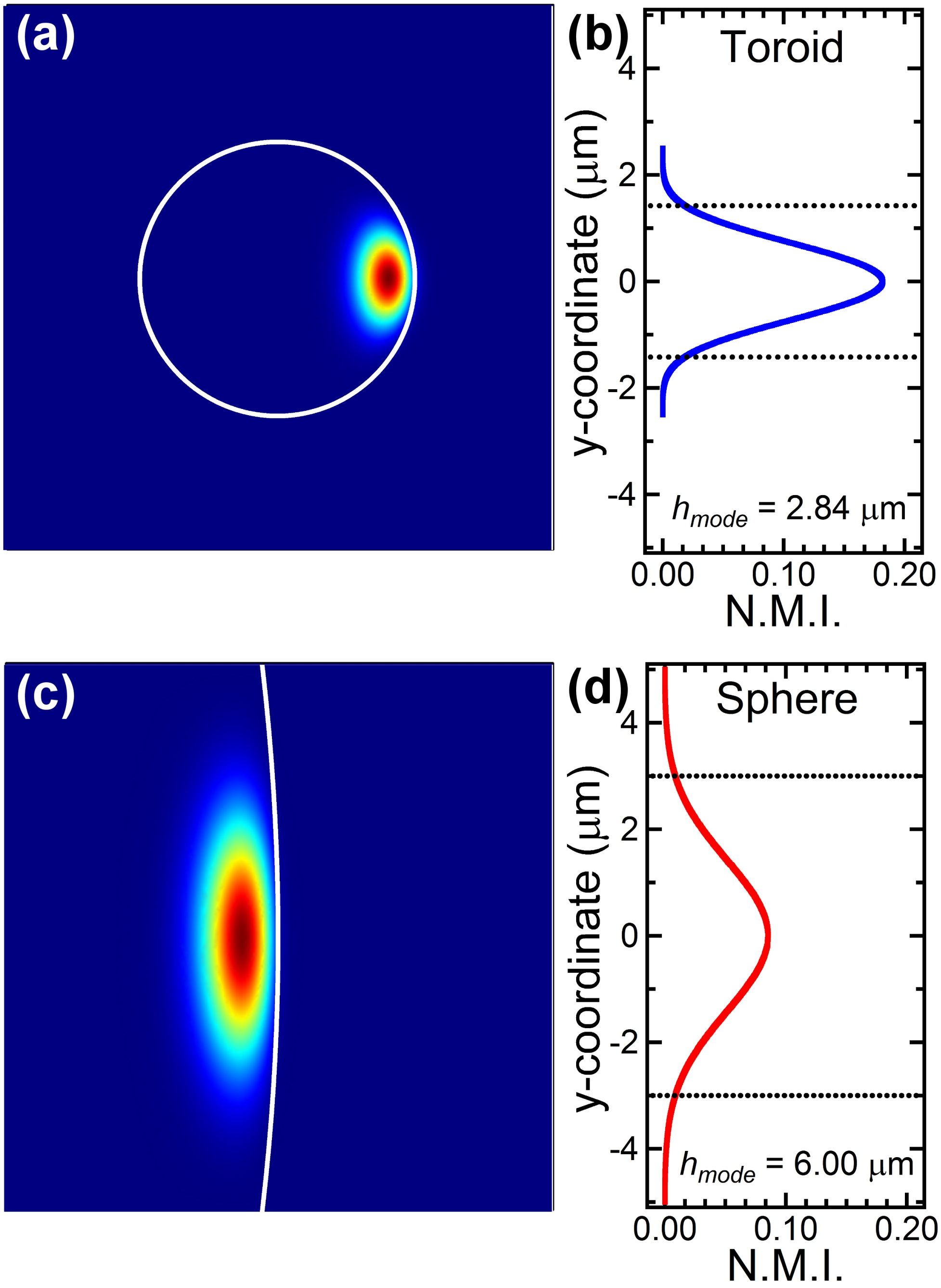

Figure 4.9: Solutions for the normalized mode intensity (NMI) of a (a) toroidal and (c) spherical optical whispering gallery mode resonator. The effective sensing area is determined by where the NMI is greater than 10% of the surface maximum as indicated by dotted lines for (b) a toroid and (d) a sphere.

Chapter 5

The Physics of Extreme Sensitivity in WGM Optical Resonator Biosensors

5.1 Abstract

Whispering gallery mode (WGM) optical biosensors are capable of extraordinarily sensitive specific and non-specific detection of species suspended in a gas or fluid. Recent experimental results suggest that these devices may attain single-molecule sensitivity to protein solutions in the form of stepwise shifts in their resonance wavelength, λ_R, but present sensor models predict much smaller steps than were reported. This study examines the physical interaction between a WGM sensor and a molecule adsorbed to its surface, exploring assumptions made in previous efforts to model WGM sensor behavior, and describing computational schemes that model the experiments for which single protein sensitivity was reported. The resulting model is used to simulate sensor performance, within constraints imposed by the limited material property data. On this basis, we conclude that nonlinear optical effects would be needed to attain the reported sensitivity, and that, in the experiments for which extreme sensitivity was reported, a bound protein experiences optical energy fluxes too high for such effects to be ignored.

5.2 Introduction

Whispering gallery mode (WGM) optical microresonators have emerged as extraordinarily sensitive tools for the label-free detection of biomolecules in solution [60, 61, 81]. These devices employ a circular resonator made from a dielectric material, most often silica, and typically have diameters less than 200 μm. This results in an adaptable surface chemistry and small effective sensing area. These traits, along with their ability to detect unlabeled biomolecules, make WGM biosensors an appealing technology for the development of analytical and diagnostic instruments, but further development requires an understanding of how these devices function and the limits of their abilities.

Soon after the first application of WGM optical resonators as biosensors [5], researchers demonstrated stepwise shifts in the resonant wavelength, λ_R, upon exposure to nanoparticle [33, 105, 106, 107] and protein solutions [1, 108], suggesting single-molecule sensitivity for these species. This intriguing possibility has inspired efforts to reconcile these results [97] with the established model for sensor response presented by Vollmer and Arnold [5, 6]. However, that model implicitly assumes a linear optical response and approximates single-molecule contribution to the signal by extrapolating from response predicted for a full monolayer of material.

The adsorption of viral particles and polystyrene beads (200-750 nm diameter) were observed to produce shifts of 10–650 fm (10^{-15} m) in the resonant wavelength of spherical sensors[33, 105, 106]. It should be noted that these experiments may not fully represent molecular detection studies or be described by previous modeling efforts [5, 6] since the analyte is sufficiently large that it does not experience uniform electromagnetic field intensity upon binding. A later study by Lu et al.[107] investigated wavelength shifts in a toroidal sensor due to the adsorption of smaller (25, 50, and 100 nm diameter) polystyrene beads, reporting shifts of 0.4–11 fm. Although significantly smaller than the previously observed beads, these are still an order of magnitude larger than a single protein and too large to experience a uniform field. The greatest WGM sensitivity reported thus far is the 1–30 fm resonance shifts upon *specific* binding of the proteins Interleukin-2 and streptavidin (M_w 15.2 kDa and 60 kDa, respectively, and diameters < 5 nm) to toroidal sensors by Armani et al.[1, 108] using uniquely low-loss resonators and high coupled powers. The details of published single-molecule or single-particle experiments involving the measurement of changes to λ_R that result from adsorption of these species are included in Table 5.1 along with abbreviations used to refer to these publications. Additional single-particle studies that measure quantities other than changes in λ_R [96, 109] are outside the scope of the present work since direct comparison is impossible.

This study examines the fundamental physical processes involved in the interaction between an optical WGM microresonator and material that adsorbs to its surface in an effort to understand the reported single-molecule sensitivity of these devices. We discuss the validity of assumptions made in previous efforts to model the behavior of WGM biosensors, and describe computational schemes necessary to capture the relevant physical phenomena. Finally, we apply these principles to predict sensor response according to computational capacity and available information about both the material properties and the experimental conditions and protocols employed in the different studies, and compare these results to data from single-molecule sensing experiments presented in SM1.

5.3 The WGM Biosensing Experiment

WGM optical resonators support circular modes that are confined to the periphery of the cavity via total internal reflection at the interface between the resonator and the surrounding medium. These modes are excited when the light introduced into the resonator can constructively interfere with itself by completing an integer number of optical cycles in the time required to make one revolution around the cavity. This occurs at the resonant wavelength, λ_R, which, assuming uniform properties around the entire resonator perimeter, can be expressed as

$$\lambda_R \approx 2\pi R_{mode}(T) n_{eff}(T)/M, \tag{5.1}$$

where M is the integer number of wavelengths in the cavity path length; T is temperature; R_{mode} is the effective radius of the mode; and n_{eff} is the effective refractive index of the mode (see Supplemental Information).

Total internal reflection at the resonator boundary produces an evanescent field in the medium outside

Table 5.1: Single-molecule and Single-particle Detection Using $\Delta\lambda_R$ for WGM Optical Biosensors

	Resonator		**Analyte**						
Code	**Shape**	**Size**^{a} (μm)	**Species**^{b}	**Size**^{c} (nm)	$\boldsymbol{\lambda}$ (nm)	**Q**	$\mathbf{P_D}$	$\boldsymbol{\Delta\lambda_R}$ (fm)	**Ref.**
SM1	Toroid	$r_a = 40$ $r_i = 4$	Interleukin-2	< 5 nm	680	$1-2\times10^{8}$	≈ 1 mW	$1 - 30$	[9]
SM2	Toroid	^{d}	Streptavidin	< 5 nm	680	^{d}	^{d}	$2 - 30$	[10]
SP1	Sphere	$R = 45$	PSL^{e}	200	1310	^{d}	^{d}	≈ 168	[5]
			PSL^{e}	500	1310	^{d}	^{d}	≈ 655	
			Virion (InfA)	≈ 50	765	6.4×10^{5}	^{d}	11.4	
SP2	Sphere	$R = 53$	PSL^{e}	750	1060	1.5×10^{6}	32μW	≈ 500	[7]
SP3	Sphere	$R = 27$	PSL^{e}	500	633	1×10^{6}	^{d}	≈ 550	[6]
SP4	Toroid	^{d}	PSL^{e}	25	680	1×10^{8}	10 μW	≈ 0.35	[8]
			PSL^{e}	50	680	3×10^{7}	10 μW	≈ 0.5	
			PSL^{e}	100	680	8×10^{6}	10 μW	≈ 11	
			Virion (InfA)	≈ 50	680	^{d}	10 μW	$1 - 11$	

---

[a] Outer radii (R) are given for spheres; major (r_a) and minor (r_i) radii are given for toroids

[b] All analytes are detected in aqueous solution

[c] Approximate analyte diameter

[d] Information not provided by the authors

[e] PSL: Polystyrene latex nanoparticle

the cavity. Material that binds to the device interacts with this electromagnetic field, altering λ_R in two ways. First, the adsorbed material displaces fluid, immediately changing the refractive index about the device. Second, the bound material absorbs energy, heating the surrounding device and fluid, causing their refractive index to change and the device to expand. The resultant resonant shift, $\Delta\lambda_R$, is described by [81]

$$\frac{\Delta\lambda_R}{\lambda_R} = \frac{\Delta n_{eff}}{n_{eff}} + \frac{\Delta R_{mode}}{R_{mode}} \tag{5.2}$$

Processes that alter either n_{eff} or R_{mode}, including the adsorption of material with a refractive index that differs from the medium surrounding the resonator, will result in a change in λ_R of a mode. The magnitude of the resonant shift increases with the contrast in refractive index between the adsorbed material and the surrounding medium it displaces, but sensitivity to single-molecule binding events requires that $\Delta\lambda_R$ exceed the measurement noise of the experiment, which was reported to be $\sigma_{\lambda_R} \approx 0.25$ fm in SM1.

Regardless of whether single molecule binding events are detected, WGM resonator sensors provide an extremely sensitive way to optically probe adsorbed species without measuring spectral features of the molecule or any tag that has been attached to it. Label-free techniques, such as this one avoid altering the behavior of the analyte molecule when attaching a tag, offering the opportunity to study the behavior of molecules in their native state. Detection of a specific analyte in a mixture may be accomplished by functionalizing the resonator surface with an antibody or other molecular recognition agent that binds exclusively to the species of interest. A variety of techniques have been reported for modifying silica surfaces [24].

The experiments leading to the reported single-molecule sensitivity of SM1 involved coupling approximately 1 mW of optical power into low-loss toroidal resonators, resulting in extremely intense electromagnetic fields within the cavity. This field strength is determined by the rate of energy coupled into the device and the rate of optical loss. The quality factor, Q, is the ratio of energy stored within the mode, W_{mode}, to the the energy lost per optical cycle, and serves as a figure of merit for resonant cavities. This quantity may be expressed as $Q = \omega W_{mode}/P_D$, where P_D is the power dissipated by the cavity and ω is the resonant angular frequency. At steady state, the power coupled into the device is equal to P_D. A high quality factor implies a resonator in which losses due to radiative mechanisms, absorption, or scattering are small[83, 110].

The studies reported in Table 5.1 span a wide range of experimental and optical parameter space. Two types of resonators were employed: (i) microtoroidal resonators were used in SM1, SM2, and SP4; (ii) microsphere resonators were used in the other studies. Some studies used narrow-linewidth 680 nm lasers to achieve the highest possible Q by minimizing absorptive losses in water, while others used lasers at 765 nm, 1060 nm, and 1310 nm. In all cases, the laser was coupled into the resonator via a tapered optical fiber waveguide. The coupled power used for experiments varied by at least two orders of magnitude from a high of $P_D \approx 1$ mW in SM1; this important parameter is, unfortunately, not uniformly reported in WGM resonator studies. Finally, the quality factor varied from $Q \geq 10^8$ (SM1,SP4) to $0.6 \times 10^6 < Q < 1.5 \times 10^6$ (SP1, SP2, SP3).

The variation in reported sensitivities may, at least in part, be a function of the differences in experimental and physical parameters involved. In the discussion that follows, we model WGM resonator sensor performance for the system for which the greatest sensitivity has been reported, i.e., SM1 [1]. In that experiment, the light transmitted through the waveguide was monitored with a photodetector while the wavelength was swept in a sawtooth pattern. None of the studies in Table 5.1 reported the scan rate; however, due to its importance, we obtained [2] the rate for SM1, $|\frac{d\lambda}{dt}| = 1.35\ \mathrm{nm\,s^{-1}}$. A Lorentzian dip in the transmission spectrum centered at λ_R indicated that light was coupled out of the waveguide and into a resonant mode, as illustrated in the simulated transmission spectrum in Figure 5.1 for a resonant mode in a device with a measured $Q \approx \lambda_R/\delta\lambda = 10^8$, where $\delta\lambda$ is the full width at half maximum of the resonance. The resonance shift, $\Delta\lambda_R$, is measured by first making a transient sweep with the sensor surrounded by fluid devoid of analyte. Transient sweeps are then taken continuously throughout the course of the experiment while a fluid containing analyte flows past the sensor. The difference between the initial resonance wavelength and the subsequent ones is the resonance shift. Although many more studies of WGM sensing have since been conducted, the combination of high Q (10^8) and coupled power ($P_D \approx 1$ mW) used in SM1 has yet to be repeated.

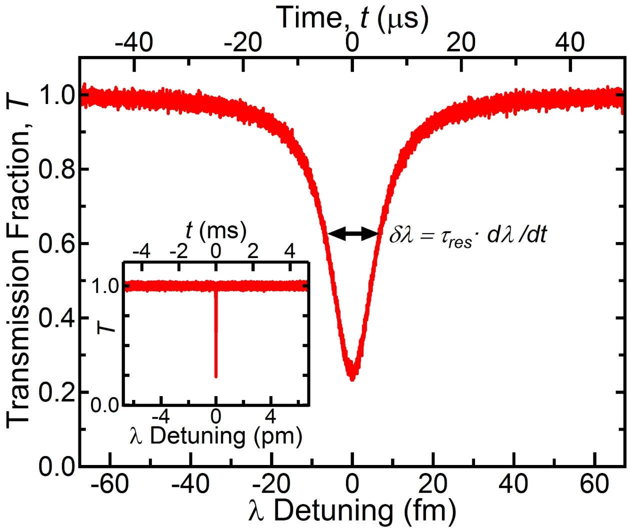

Figure 5.1: Part of a simulated transmission spectrum that might be observed by measuring the photodetector output using an oscilloscope while the wavelength is swept at $\frac{d\lambda}{dt} = 1.35$ nm s^{-1} across a resonance with $Q = 10^8$. The full wavelength scan is shown in the inset. The lower horizontal axis is in terms of wavelength detuning from λ_R while the upper is in terms of time.

5.4 Existing Models of WGM Biosensor Behavior

The first model to describe the WGM sensor response upon binding of protein molecules to its surface is presented by Arnold and Vollmer [6] and treats the bound material as a perturbation to the energy of the optical mode. The resulting shift in resonant wavelength is then expressed as

$$\frac{\Delta\lambda_R}{\lambda_R} \approx \frac{\delta W_{mode}}{W_{mode}} \approx \frac{\alpha_{ex}|\mathbf{E}_0(\mathbf{r})^2|}{2\int \epsilon_R|\mathbf{E}_0(\mathbf{r})|^2\, dV} \tag{5.3}$$

where W_{mode} is the mode energy, α_{ex} is the excess polarizability of the bound material (i.e., the difference in the polarizability of the protein compared and the water it displaced), $\mathbf{E}_0(\mathbf{r})$ is the electric field at position $\mathbf{r}$, ϵ_R is the permittivity of the resonator, and the denominator is integrated over all space. Applying the analytical solutions for the mode in a spherical device and integrating the effect of all molecules present at steady-state surface coverage provides an estimate of the frequency shift as a function of the surface density of bound proteins, σ_p, the refractive indices of the resonator and its surrounding medium, n_R and n_M, respectively, the permittivity of vacuum, ϵ_0, and the effective radius of the mode, R_{mode}, i.e.,

$$\frac{\Delta\lambda_R}{\lambda_R} \approx \frac{\alpha_{ex}\sigma_p}{\epsilon_0(n_R^2 - n_M^2)R_{mode}}. \tag{5.4}$$

Teraoka, Arnold, and Vollmer [111] completed a more detailed examination of the effect of the protein on the electromagnetic field; they showed that Eq. (5.4) is the first-order perturbation term for the whispering gallery mode resonance.

This model assumes that perturbations to the optical properties of the mode that occur when protein molecules adsorb and displace solvent molecules are independent of the optical field strength. It also assumes that the magnitude of the energy perturbation this protein represents is limited to the difference in the work that must be done to distort the electron distribution of the protein to align with the electric field relative to the electron distribution of the solvent. The molecules are assumed to bind at randomly distributed positions on the sensor surface, a notion in need of validation in light of the subsequent demonstration of optical gradient forces trapping larger species (i.e., nanoparticles) in the evanescent field of a WGM resonator by the same researchers [111] and hydrodynamic focusing in the flowing-sample mode of operation employed in SM1 [112]. Nonetheless, this model is an excellent foundation upon which to advance our understanding of these devices. Experimental results presented by Vollmer et al. [5] and Arnold et al. [6] use resonators with $Q \approx 2 \times 10^6$ and unspecified coupled power to show that cross-sectional areas for bound proteins calculated from the measured $\Delta\lambda_R$ values agree well with crystallographic data.

The original inference of single-molecule detection with a WGM resonator in SM1 [1] presented a model to relate the resonance shift to intuitively important physical parameters. The authors noted that, at high circulating optical power, the effect of a bound molecule may be enhanced due to the thermo-optical effect, wherein the refractive index varies with temperature increases that occur as a result of light absorption by the bound molecule. This dependence is determined by the thermo-optical coefficient, $\frac{dn}{dT}$. The relative single-molecule shift in resonant wavelength was estimated to be

$$\left[\frac{\Delta\lambda_R}{\lambda_R}\right]_{SM} = \frac{\sigma\lambda\frac{dn}{dT}}{8\pi^2 n_R^2 \kappa_T V} Q P_D \int \frac{|u(\mathbf{r})|^2}{|\mathbf{r}|+\varepsilon} d\mathbf{r} \tag{5.5}$$

where σ is the absorption cross section of the protein, κ_T is the thermal conductivity of silica, V is the mode volume, $u(\mathbf{r})$ is the "whispering gallery mode field," and ε is a size parameter on the order of the physical radius of the molecule. The model neglects thermal coupling between the resonator and the surrounding fluid, only considering temperature changes within the silica cavity where greater than 95% of the mode energy resides.

Though the authors provide no derivation for Eq. (5.5), it appears to have been inspired by the work of Gorodetskii and Il'chenko [113]. This study describes the heat generated by absorption in a differential volume element, h_V, in terms of the bulk absorption coefficient, α_{abs}, and the energy density of the electric field at that point, $\tilde{W}_e$, as $h_V = \omega\alpha_{abs}\lambda\tilde{W}_e/2\pi n$. Without a detailed derivation of Eqn. (5.5) it is difficult to identify and evaluate all the assumptions that went into the model, but the absence of any time-dependent quantity or heat capacity suggests that steady-state thermal conditions were assumed. Noting a three order of magnitude unit-conversion error in the absorption cross sections of the molecules studied by Armani et al.[1], Arnold[97] argued that this model cannot explain the wavelength shifts that were reported. Though the model appears to poorly describe the data, it suggests that nonlinear physical processes may contribute to the sensor response. If the bound protein causes heating, the strength of the heat source will vary with time as the wavelength is swept and P_D varies. The temperature plume generated by a single bound protein could, through this thermal perturbation, affect a region hundreds of times larger than the molecule itself. This phenomenon, also referred to as photothermal lensing, has been applied with great success to detect single molecules from changes in light scattering due to the thermal plume [114, 115].

More recently, Arnold et al. [97] consider the heat transfer to estimate the change in temperature experienced by the mode. They argue that the bound protein molecule can be treated as an induced dipole held in an electric field oscillating at frequency ω. The heat generated by the protein in watts, h, is then expressed as the change in the energy of the configuration with time, a quantity that is related to the absorption cross section of the molecule via

$$h = \langle \mathbf{E}(\mathbf{r}_a, t) \cdot \partial \mathbf{p}/\partial t \rangle = \tfrac{1}{2}\omega \varepsilon_0 n_m \sigma \left|\mathbf{E}_0(\mathbf{r}_a)\right|^2 / k \tag{5.6}$$

where $\mathbf{E}(\mathbf{r}_a, t) = \mathbf{E}_0(\mathbf{r}_a, t) \exp(i\omega t)$ is the electric field at the position of the protein, $\mathbf{p}$ is the induced dipole moment, $\mathbf{r}_a$ is the position of the protein, ε_0 is the permittivity of vacuum, n_m is the refractive index of the medium surrounding the resonator, and k is the magnitude of the wave-vector in vacuum. This model describes the underlying physical processes that govern the steady-state response to a bound particle or molecule, but does not describe the transient signals produced by the swept-frequency experiments of Armani et al. [1] or any other researchers in the field. Thus, in spite of numerous efforts to model the extreme sensitivity of WGM biosensors, questions remain.

5.5 Physical Processes in WGM Sensing

Each of the aforementioned models incorporates simplifying assumptions in an effort to develop analytical descriptions of WGM biosensor resonance shifts. The discussion that follows explores the physical processes in an effort to develop a model that more accurately describes the the experimental system for which extreme sensitivity has been reported.

First, we consider the nature of the WGM sensing experiment. As noted above, the simplest models assume that the laser is continuously tuned to the resonance to enable steady-state operation despite this setup never having been demonstrated experimentally [116]. In contrast, the experiments of Table 5.1 involve sweeping the laser output over a range of wavelengths to find resonance. To capture the widest variety of physical phenomena that may occur using this technique, we model experiments at high P_D and Q. Nanoparticle studies are thus irrelevant to the model under development since there no high-power, high-Q studies to compare with the model. As a result, we consider the single-molecule studies SM1 and SM2.

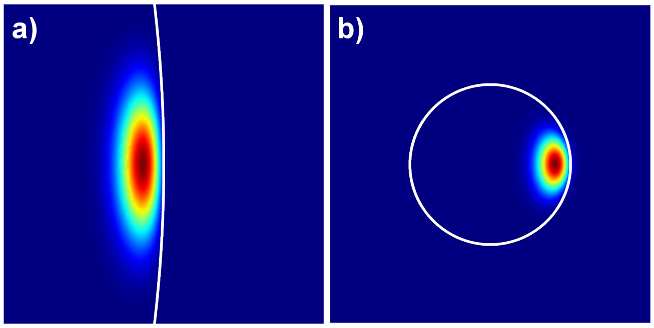

Figure 5.2: The normalized mode intensity for $\lambda_R \approx 680$ nm in a (a) spherical ($R = 42.5$ μm) and (b) toroidal ($r_a = 40$ μm, $r_i = 2.5$ μm) WGM resonator.

Excitation of the Optical Mode

Whispering gallery modes may be excited in a variety of closed dielectric structures including rings, disks, spheres, cylinders, tubes, and toroids [60, 61]. Each of these geometries has unique mode structures, as illustrated in Figure 5.2 for spherical and toroidal cavities. Predicting how biomolecules that adsorb to the surface of these devices will interact with resonant light begins with an accurate description of this mode structure.

Light is coupled into the microcavity using a waveguide, which we assume here to be a tapered optical fiber waveguide as described above. An evanescent wave decays with distance from the surface of the waveguide; bringing the resonator within the evanescent field couples a traveling wave into the cavity. The extent to which the optical field from the waveguide overlaps the WGM in the resonator determines how much total power can be coupled into the device [88]. Previous studies ignore the method of coupling and assume that a single mode is populated in the WGM resonator [97]. This choice does not necessarily reflect experimental conditions as modes often overlap in wavelength-space, but it appears to be an acceptable approximation. Spherical and cylindrical cavities provide the advantage of well-developed analytical expressions for the electric and magnetic field profiles [89, 117] for a variety of coupling methods. Oxborrow [103] presented a convenient, and much more general, method for calculating the mode profile for axisymmetric systems using COMSOL multiphysics, the same finite element solver that we employ below. The numerical solutions obtained via this method must, however, be rescaled to reflect the power coupled into the cavity for a given experiment. Another approximate expression for the mode in a toroid was derived using perturbation theory for quasi-TE and TM modes [80], although those expressions are not provided in their entirety.

Poynting's theorem for harmonic fields may be used to calculate the energy flux inside and outside of the resonator. In the case of no current flow, this is

$$2i\omega \int_V (\tilde{W}_e - \tilde{W}_m)\, dV + \oint_A \mathbf{S} \cdot \mathbf{n}\, da = 0, \tag{5.7}$$

where $\mathbf{S} = \frac{1}{2}\big(\mathbf{E} \times \mathbf{H}^*\big)$ is the time-averaged Poynting vector, $\mathbf{n}$ is the unit normal vector at the differential surface da, $\mathbf{E}$ is the electric field, $\mathbf{H}$ is the auxiliary field, and $\tilde{W}_m$ is the energy density of the magnetic field. The first term in this expression is integrated over the volume of the system and the second term is integrated over the surface area of the system.

For a resonator fabricated from a lossless dielectric, and with no scattering at the resonator boundaries, $\oint_A \mathrm{Re}(\,\mathbf{S}\cdot\mathbf{n})\, da = 0$ because there would be no net energy flow leaving the cavity for such an ideal device. The imaginary part of the Poynting vector for this system is a measure of the circulating, or stored, energy. The materials used in the laboratory are far from ideal, each with its own complex refractive index, so power will be coupled out of the resonator according to the real part of the Poynting vector as scattered and absorbed light. The time-averaged Poynting vector incorporates all the losses due to scattering and heating within both the glass and the surrounding water. It does not include the additional losses due to the perturbation of the system by the protein; these must be evaluated using the light remaining in the resonator ($\mathrm{Im}(\mathbf{S})$). This is similar to the attenuation of circulating power in a resonator by a point defect [118]. A typical value for the time-averaged energy flux at the surface of a microcavity with $Q \approx 10^8$ and $P_D \approx 1$ mW is 1–10$\times 10^{13}$ W/m^2.

Since the excitation wavelength is scanned during the measurement of the transmission spectrum, the power coupled into the WGM changes as a Lorentzian function of time as the wavelength is scanned at rate $\frac{d\lambda}{dt}$ past the resonance (see Fig. 5.1). For the single-molecule experiments in Table 5.1, the typical time required for optical loss mechanisms and the "ring-up" of the mode to reach a steady state ($\tau_{WGM} < 10$ ns) is very small compared to both the total time for a wavelength scan ($\tau_{scan} \approx 5$ ms) and the time to scan across a single resonance of $Q \approx 10^8$ ($\tau_{res} \approx 5$ μs based on full width at half-maximum of Lorentzian profile). This useful relationship, which may be expressed as $\tau_{WGM} \ll \tau_{res} \ll \tau_{scan}$ suggests that optical timescales may be considered instantaneous.

Interaction of Resonant Light with Surrounding Materials

Here we consider the interaction between the electromagnetic fields in a resonator with $Q \approx 10^8$ and the various materials that play a role in a WGM sensing experiment. As light passes through matter, the time-varying electromagnetic fields interact with the electrons in a material according to its molecular or crystal structure. A single molecule, for example, may have a net dipole moment if it includes net charge or an asymmetric arrangement of atoms with varying electronegativities. Regardless of whether such a permanent dipole exists, an electric field will distort the flexible electron distribution in a material and generate an induced dipole according to the polarizability of the molecule. These dipoles will align themselves to the instantaneous orientation of the electric field. The interactions between light and matter result in a slower propagation than in a vacuum, and are collectively described by the complex refractive index $\tilde{n} = n + i\kappa$. The real part of the refractive index, n, is the ratio of the propagation velocity in vacuum, ν_{vac}, to that in a particular material, ν_{mat}, i.e., $n = \frac{\nu_{\text{vac}}}{\nu_{\text{mat}}} = \frac{\lambda_{\text{vac}}}{\lambda_{\text{mat}}}$. The imaginary part of the refractive index, κ, describes the attenuation of light due to loss mechanisms such as absorption or scattering.

Regardless of whether a protein molecule is present, light circulating within the WGM resonator interacts with the silica cavity and the water surrounding the device. Water molecules form strong hydrogen bonds with one another. The electron distribution in each material undergoes oscillating perturbations in response to the optical field. Water molecules, however, are free to alter their orientation to the extent allowed by their hydrogen bonds. In contrast, silica exists as a rigid amorphous solid whose covalent bonds prohibit any significant translational or rotational motion. The energy that induces this electron and molecular motion is dissipated as heat, leading to linear absorption by these materials in the electromagnetic field.

The presence of a bound protein molecule on the surface of the resonator complicates this response. Each of the amino acids in a protein molecule has a unique permanent dipole moment and molecular polarizability that reflects its composition. Exposure to an electric field induces an additional dipole moment, just as in the silica and water, but the protein can also change its conformation in response to the applied field. The tertiary structure of the protein is determined by the intramolecular forces as well as the energetic incentive to hide hydrophobic regions of the molecule from the surrounding water. What is often thought of as a rigid molecule is, in fact, in continuous flux. Thermal vibrations allow the molecule to sample a range of conformations, all of which are sensitive to interactions with surrounding species and external electric fields. Each conformation has a unique permanent dipole moment, however. Whereas the permanent dipole moment can be treated as a constant for silica and water, this flexibility causes the molecular conformation, induced dipole moment, and permanent dipole moment of the entire protein molecule to become functions of time in the presence of intense, temporally, and spatially varying electric and magnetic fields.

The behavior of the protein in these conditions is even more complex when considering the non-ideality of the interactions between light and matter. It is useful at this point to view the protein as a network of oscillators (i.e., polarizable amino acids) being forced by time-varying optical fields. The timescale of the variation of the electric field ($\tau_{field} \approx 10$ fs) is much shorter than that of molecular motion[119] ($\tau_{molecule} \approx$ 10–1000 fs), so there is a lag between the instantaneous alignment of the field and the orientation of the permanent dipole. In contrast, induced dipoles are established in time $\tau_{electron} \approx 10^{-3}$ fs $\ll \tau_{field}$. The existence of a lag in the alignment of the permanent dipole implies that the electric field must fight the rotational momentum it imparted on the protein during its last optical cycle, increasing the energetic cost as light propagates through the protein. We refer to the work required to align the induced and permanent dipoles as W_A; it depends on protein size, permanent dipole moment, and the polarizability of the constituent amino acids. Only the portion of this work related to the creation and alignment of the induced dipole is considered by Arnold and Vollmer[5, 6].

The conformational changes that the protein undergoes may give rise to an additional lag between the orientation of the protein dipole and the electric field alignment. In this case it is more reasonable to view the protein not as a molecule, but as a polymer where each amino acid is responding independently. The

3-dimensional arrangement of these components reflects a vast array of intramolecular interactions that are stretched and bent when an electric field is applied to the molecule. Behaving like springs, these interactions can oppose molecular realignment and increase the amount of work that must be done by the optical fields, W_{IM}. The calculation of W_{IM} based on amino acid sequence or a known tertiary structure has yet to be demonstrated.

Finally, an accurate molecular-scale depiction of the protein must also include the thermal motion that constantly perturbs the tertiary structure of the molecule. The electric field must fight the thermal vibrations of the protein molecule as it changes its conformation. Since each amino acid responds differently to the field according to its physical properties and interactions with nearby amino acids, the degree of thermal vibration is likely nonuniform across the molecule. An electric field must overcome the thermal energy of the system ($E_{thermal} \approx k_B T$, where k_B is the Boltzmann constant) in order to maintain alignment of the dipoles. Therefore, thermal effects could be significant at high optical intensities because of increased absorptive heating, thereby increasing the work to overcome thermal motion, W_T.

The total work done by the propagating optical field on a protein molecule, W_{tot}, may be thus expressed in terms of these three sources

$$W_{tot}(T) = W_A + W_{IM} + W_T(T) \tag{5.8}$$

where W_A describes the work to overcome the forces resulting from a lag in alignment between the electric field and the protein dipole, W_{IM} is the work required to overcome intramolecular forces that introduce additional lag, and W_T is the work done correcting for misalignment due to thermal vibrations. This work is dissipated as heat when the field imparts kinetic energy on the molecule, and that energy is transferred to the surroundings via molecular collisions.

Energy may also be injected into the system as heat if the protein directly absorbs light. Absorption requires the incident light to be at a frequency that excites mechanical or electronic resonances in the molecule. At low optical intensities, the amount of heat generated is proportional to the amount of light absorbed. This process is typically described by the absorption cross section of the molecule, $\sigma(\lambda)$, which is the cross section that a black body absorber would have if it was absorbing as much light as the protein. The absorption cross section of a protein in solution may be calculated based on absorbance measurements in the dilute limit (where scattering and agglomeration may be neglected). Typically, non-fluorescent proteins do not absorb strongly near 680 nm (in contrast to $\lambda < 350$ nm where proteins absorb quite efficiently due to the electronic structure of aromatic amino acids). As a result, concentrations above 10 μM must be used for these absorption spectrophotometry measurements despite the potential for artifacts such as aggregation that may occur at such high concentrations.

The intense optical fields that build up within a WGM resonator with $Q \approx 10^8$ (irradiance $\approx 10^{13}$ W/m^2) suggest that linear absorption may account for only a portion of all energy that is absorbed by a surface-bound protein molecule and consequently dissipated as heat. To date, the contribution of nonlinear phenomena to WGM sensor response has been ignored, but it may be relevant due to the high irradiance experienced by adsorbed material. In fact, the intense circulating powers achievable in WGM resonators have been used to create lasers by doping the dielectric with a gain medium [120, 121, 122]. An important category of nonlinear effects is optical limiting, which is often studied in chromophores [123, 124] with respect to optical limiting switches and other photonic applications[125, 126]. This phenomena is characterized by a significant deviation from linear absorption behavior with increasing irradiance. Optical limiting of transmission is often explained by phenomena such as multiphoton absorption, a process involving absorption of an additional photon by a molecule that is already in an excited state. A large irradiance, and the frequent photon interactions that result, are necessary to exceed the threshold at which an additional photon arrives during the lifetime of the excited state. One can imagine that, even for meager absorption, exposure to a sufficiently high power of light would increase the vibrational energy of the protein molecule greatly and may vastly increase the amount of work required to overcome W_T.

Other nonlinear optical phenomena may play a role in WGM sensing as well, including second harmonic generation (SHG) and the Kerr effect. SHG is a second-order nonlinear process that involves the generation of light at $\lambda_{SHG} = \frac{1}{2}\lambda_{input}$, which, for the excitation wavelengths used in WGM biosensing experiments ($\lambda_{input} = 680$ nm), generates light in a range that is absorbed *far* more efficiently (10x or more) by proteins than the WGM excitation light. SHG is more likely to occur at a material interface because inversion symmetry is broken there [127], enabling a weak SHG signal to be generated even in materials such as silica that do not exhibit the phenomena in the bulk [127]. This technique was recently used to demonstrate coherent SHG from a small number of fluorescent molecules patterned on a spherical WGM resonator [128]. The Kerr effect, which is a third-order nonlinear process whereby the refractive index of a material is a function of the electric field strength, has been demonstrated relevant in silica for ultra-high Q resonators at room temperature [129].

Unfortunately, very little information is available on the physical constants describing nonlinear phenomena in non-fluorescent proteins. If a fluorescent species absorbs efficiently, its binding could cause both a resonance shift *and* a step change in the quality factor of the mode [1]. Non-fluorescent species absorb too little light to measure these physical properties using conventional fluorescence spectroscopy. Although it is difficult to generate continuous electromagnetic waves intense enough to probe nonlinear optical phenomena for proteins, ultra high Q WGM resonators generate the needed fields, possibly contributing to the previously reported sensitivities and enabling future study of nonlinear phenomena in biomolecules. Thus, the uv-vis spectrophotometric measurements used to describe simple, linear absorption are likely incomplete.

Heat Transfer

A non-fluorescent protein molecule that absorbs light will generate heat $h = \sigma \mathrm{Im}(\mathbf{S} \cdot \hat{\phi})$, where $\hat{\phi}$ is the unit vector in the direction of light propagation. A fluorescent protein dissipates some of its absorbed energy as light, however the remainder is converted to heat according to $h_f = (1 - \eta_q)h$, where η_q is the quantum efficiency of the fluorophore under experimental conditions. The dissipated heat will be removed from the vicinity of the absorbing protein(s) by collisions with surrounding molecules. The thermal coupling of the protein to the resonator and to the surrounding fluid depends on the molecular configuration, which includes a patchy network of hydrophobic and hydrophilic regions, in contrast to the uniform surfaces of polymer beads that have been the subject of numerous studies (see Table 5.1). Recent molecular simulation studies suggest that these local regions of hydrophobicity in the protein can decrease the density of the surrounding water molecules immediately adjacent to those regions, drastically reducing the ability of the protein to transmit its thermal energy to the solvent [130].

Furthermore, in specific binding studies, the protein is not bound directly to the surface of the resonator. Instead, it is tethered to the resonator by the targeting species, which itself has been immobilized to the surface, possibly through covalent linkages. These molecular recognition agents that connect the protein to the resonator surface further differentiate the biomolecule sensing experiments from those involving beads. This may mean that, in the case of the protein, the most efficient means of dissipating energy could be through the high-affinity interactions with the targeting molecule attached to the sensor surface. This could have significant implications on the isotropy of heating that occurs in response to excitation of the protein by the resonant light, suggesting that the molecular properties of the targeting molecule (e.g., rigidity, polarizability, size, etc.) could play a role in the resonance shift observed upon analyte binding. To date, researchers have assumed that the interaction between the targeting species and the mode contributes only to the baseline of the resonance shift measurement and plays no role during the analyte sensing experiment.

The modeling of nanoscale heat transfer requires knowledge about these numerous and complex interactions between a particular protein species and its surroundings [131]. Lacking the data to describe these molecular-scale effects, we assume bulk material properties and energy transport models that apply to macroscopic systems. This assumption is quantitatively accurate within the silica and water, describing the formation of a temperature plume with characteristic radius $l_{plume} \sim (\rho C_P \tau_{res}/\kappa_T)^{-1/2}$, where ρ is the material density and C_P is the heat capacity. There is a transition from a discrete to a continuous system near the protein molecule that will affect the magnitude of the temperature perturbation within this plume and, ultimately, determine the magnitude of the resonance shift. Heat transfer in the continuous system may be described by the heat conduction equation,

$$\mathbf{q} = -\kappa_T \nabla T, \tag{5.9}$$

where the heat flux $\mathbf{q}$ is proportional to the local gradient in temperature. The energy balance for the WGM biosensor system may be expressed as

$$\rho C_P \frac{dT}{dt} + \kappa_T \nabla^2 T = \frac{\omega \alpha \lambda n |\mathbf{E}|^2}{2\pi} + h_{SM} \delta(\mathbf{r} - \mathbf{r_a}), \tag{5.10}$$

where the transient temperature profile, $T(\mathbf{r}, t)$, is evaluated at position $\mathbf{r}$ and time t. All physical properties are a function of $\mathbf{r}$ to account for the different materials. The right side of (5.10) describes heat generation in the system. The first of these terms describes the heat source due to bulk absorption by the resonator and its surroundings [113], while the second term represents that due to the protein at position $\mathbf{r_a}$. Here δ represents the Dirac delta function. In these experiments the protein sits at the interface between two materials, and so thermal dissipation will be anisotropic due to the different physical properties in the resonator and the surrounding fluid (see Supplemental Information). Note also that the magnitude of the electric field, $|\mathbf{E}(\mathbf{r}, \mathbf{t})|$, is a function of position *and* time because the power is coupled into the resonator in a Lorentzian time pulse (as illustrated in Fig. 5.1) as the wavelength is swept past the resonance.

This Lorentzian functional form represents an ideal case. The true shape of this function is a challenge to predict *a priori* because it can be strongly affected by bulk heating due to absorption, but the Lorentzian shape and its distortion have been modeled for axisymmetric systems[132]. As the wavelength is swept, absorption warms the resonator and surrounding medium, causing a shift in the resonant wavelength according to the thermo-optical effect. Since their thermo-optical coefficients have opposite signs, the warming of water will produce a resonance shift opposite in sign to that caused by warming silica. This results in an asymmetric broadening or narrowing of the resonance peak in the transmission spectrum depending on that fraction of the mode that overlaps each material [1] or the direction of the wavelength sweep (see Supplemental Information). This effect, discussed in further detail by Carmon, et al. [116], was also observed by Lu and colleagues in SP4 for $P_D \approx 10\ \mu$W and is experimentally demonstrated in the Supplemental Information to this chapter. One consequence of this heating effect is that the up scan has a wider resonance peak, which allows power to be coupled in for a longer fraction of the scan, possibly increasing sensitivity. What appears to be a Lorentzian peak in the case of negligible absorption can become a complex function of the material properties and experimental parameters. Schmidt et al. [133], and Rokhsari et al. [134] explore in more detail the role of $\frac{d\lambda}{dt}$ and P_D on the appearance of the transmission spectrum. Transmission curves from biosensing experiments are rarely, if ever, reported. This handicaps efforts to validate any model, as these curves are needed to accurately gage distortion by bulk heating, and the subsequent effects on coupled power throughout the experiment.

The thermal effects that contribute to the distortion of the Lorentzian transmission peak used to identify the instantaneous value of λ_R in a WGM biosensing experiment emphasize the transient nature of the experiment. A measurement with time resolution of τ_{scan} is used to determine a quantity that varies on a timescale τ_{res}. By considering thermal diffusion, we introduce another timescale: the time for a heat source at the sensor surface to be experienced by the optical mode, τ_{HT}. This timescale may be expressed in terms of material properties and the relevant length scale over which diffusion must occur, l_{mode}. We assume that the radial distance from the sensor surface to the peak of the mode intensity as an acceptable approximation of l_{mode}, which gives $\tau_{HT} \approx \frac{r_a^2 \rho C_p}{\kappa_T} \approx 0.3\ \mu$s for the toroidal resonators used in SM1. This value is comparable to τ_{res}, implying that it will take the duration of the pulse before the entire mode experiences the full effect of the heat from a single-molecule source. Our efforts to solve the transient Equation (5.10) represent a significant deviation from previous efforts to model WGM biosensor response [5, 6, 111, 1, 97] where no heating or steady-state heating are assumed.

Changing Material Properties

It is evident from the analysis of molecular scale physical processes that no previous effort to describe the WGM sensor device response has modeled the transient sensing experiment in which attomolar sensitivities and single-molecule binding events were observed. By scanning the excitation wavelength in order to measure λ_R, the power coupled into the optical field becomes a function of time and position $\mathbf{r}$. Both linear and nonlinear optical phenomena introduce heat into the system, making the temperature a function of position and time t as well. The electric field and temperature change with time; so too will a number of important physical properties of the system. These include the refractive index and thermo-optical coefficient [135],

Table 5.2: Summary of Functional Dependencies of Physical Properties

Refractive Index	$n(T, \|\mathbf{E}\|, \mathbf{r})$
Resonator Radius	$R_{res}(T)$
Bulk Absorption Coefficient	$\alpha_{abs}(T, \|\mathbf{E}\|, \mathbf{r})$
Protein Absorption Cross Section	$\sigma(T, \|\mathbf{E}\|)$

absorption coefficient, and protein absorption cross section. The resonator may also expand due to bulk temperature increases on the order of 1-10 K according to the thermal expansion coefficient [116], α_{exp}. These effects are summarized in Table 5.2. At the level of the individual protein and its surroundings, any application of bulk material properties may be quite inaccurate due to local variations in density or energy.

5.6 Modeling WGM Biosensors

A rigorous model of the transient WGM biosensing experiment must take into account all of the physical processes outlined above, including the time-varying material properties of the system. Calculating the sensor response, $\Delta\lambda_R(t)$, therefore requires a numerical computation scheme like the one depicted in Fig. 5.3a, which involves evaluating the instantaneous value of λ_R at descrete points in time. In this case, accuracy demands that the time steps be sufficiently small to capture the rapid changes that occur in the system due to the Lorentzian shape of the curve in Fig. 5.1. In general, solving for $\Delta\lambda_R(t)$ requires beginning at $t = 0$ and continuing by: (i) evaluating the power coupled into the resonator based on $\lambda(t)$, (ii) determining the material properties of the system as a function of current temperature profile and position, (iii) calculating the 3-dimensional electromagnetic field profile, (iv) evaluating the amount of heat generated by the silica, water and protein according to the electromagnetic field profile, (v) solving for the updated temperature profile, taking into account thermal diffusion, (vi) calculate integral

$$\Delta n_{eff} \approx \frac{\int_V \frac{dn}{dT}\Delta T(\mathbf{r})|\mathbf{E}(\mathbf{r})|dV}{\int_V |\mathbf{E}(\mathbf{r})|dV} \tag{5.11}$$

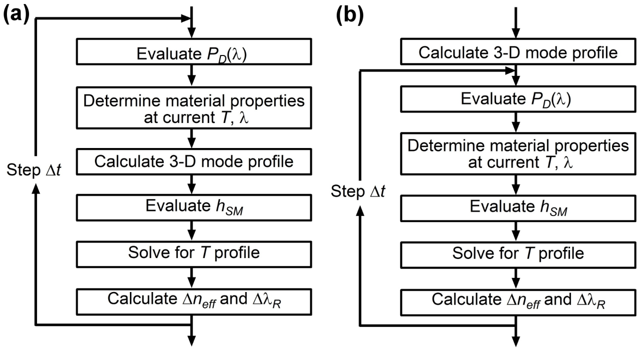

Figure 5.3: (a) Rigorous and (b) modified computation schemes for calculating the WGM sensor response.

to determine $\Delta\lambda_R$, and (vii) stepping Δt in time and repeating this process. A more complete discussion of this computation method is included in the Supplemental Information.

Simulating all simultaneous physical processes using the scheme in Fig. 5.3a is not presently possible due to the lack of information about how a single protein molecule may respond to the intense optical fields within a WGM resonator with $Q \approx 10^8$. We instead begin by evaluating the assumptions that may be made to simplify this enormous challenge. For example, thermal expansion due to temperature change may be considered negligible according to both theoretical predictions and experimental observations [136], suggesting that we may be able to omit the second term on the right hand side of Eq. 5.2. However, it remains unclear if the thermal perturbation from the protein heat source is significant enough to warrant repeating the mode structure calculation at each computation step in light of the local thermal expansion of the silica that may result. The full, 3-dimensional simulation of the mode structure and solution for the eigenfrequencies (i.e., resonant frequencies) of the mode, followed by the evaluation of the protein heat source and solution of micro-scale heat transfer, would accomplish the same goals as the computation scheme above, but would require a supercomputer to implement.

Finite element analysis has become a valuable tool in solving for such complex systems, and it is particularly well-applied here where computational accuracy and labor can be focused on regions in the geometry where it is needed by generating smaller mesh elements there. We use a commercially available software package, COMSOL Multiphysics, to solve for the electromagnetic field and the temperature profiles, as a function of time in the simple case of a point source of heat at the interface of silica and water blocks.

Here we used the computation scheme outlined in Fig. 5.3b to consider the limiting case where the only heat introduced into the system is due to linear absorption by the protein molecule during a frequency sweep, and the effect that this thermal perturbation has on the mode structure are negligible. These assumptions are identical to those made in previous evaluations of the thermo-optical model of WGM biosensor response [1, 97], but our efforts include a consideration of transient heat transfer. We use the Oxborrow method [103] to calculate the electromagnetic field profiles for a toroidal resonator with major radius $r_a = 40$ μm, minor radius $r_i = 2.5$ μm, and material properties as detailed in the Supplemental Information. We also assume that the analyte is the common tetrameric protein streptavidin[97] ($\mathrm{M_w} \approx 60$ kg/mol) for which $\sigma = 1 \times 10^{-23}$ m^2. At peak coupled power the protein molecule is exposed to an irradiance of 6×10^{13} $\frac{\mathrm{W}}{\mathrm{m}^2}$ and produces a heat of $h_{SM} = \sigma \mathrm{Im}(\mathbf{S} \cdot \hat{\phi}) \approx 6 \times 10^{-10}$ W. Quality factors ranging from 10^6 to 10^8 are also considered.

5.7 Results and Discussion

We model the WGM biosensor response to the adsorption of a single protein molecule, as in SM1, using the computational scheme outlined in Fig. 5.3b to solve for the mode structure, the intensity of the single-molecule heat source, and the 3-dimensional transient temperature profile. The results of our finite element model show an asymmetric thermal plume that evolves and expands over time into the silica and the water. A cross-section of the temperature profile at peak coupled power, as well as its overlap with the mode structure, is depicted in Figure 5.4. To better visualize the transient evolution of the plume, we look more closely at the temperature at two points of interest in Figure 5.5. These two points correspond to the location of the protein and the point of maximum mode intensity. Note that the maximum temperature that occurs at the mode peak lags that at the protein. This delay is the time required for the heat to diffuse from the interface to the location of the mode peak, a distance of roughly 0.5 μm according to the Fig. 5.2. The calculated time delay of $\tau_{delay} \approx 0.8$ μs corresponds well to the value of τ_{HT} estimated above, although it should be noted

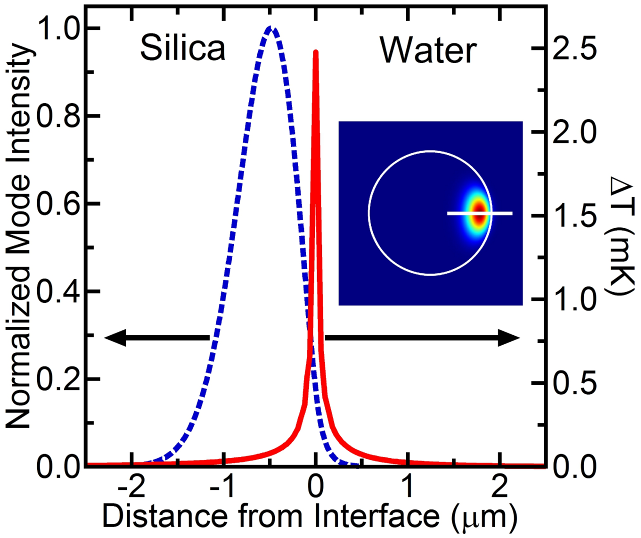

Figure 5.4: The normalized mode profile in a toroidal resonator with major radius $r_a = 40$ μm and minor radius $r_i = 2.5$ μm corresponding to the shown cut line (inset) and the thermal plume resulting from a single-molecule protein heat source exposed to a mode with $Q = 10^8$ and $P_D = 1$ mW resulting in linear absorption by the molecule.

that these simple scaling arguments do not capture the full complexity of the interactions of the thermal plume with the optical mode. This plume may also lead to localized thermal expansion of the resonator and affect sensor response. Modeling the thermal expansion near the protein, we conclude that the temperature rise that results from linear absorption is too small to measurably affect the resonance shift and omit it from further calculations.

We can now estimate the resonance shift by integrating over the calculated 3-dimensional temperature profile according to Eq. (5.14). This integral is evaluated at each time point for a range of quality factors, as shown in Fig. 5.6. The predicted shifts in resonant wavelength for Q values ranging from 10^6 to 10^8 fall between 0.05 to 1.6 am (10^{-18} m), as indicated by the maxima in the curves of Fig. 5.6. The resonance shift corresponding to $Q = 10^8$ is a factor of $10^3 - 10^4$ smaller than the sensor responses observed in SM1 and SM2, suggesting that linear absorption by the protein in the absence of bulk heating is insufficient to explain those experimental results. However, while decreasing Q may also decrease the intensity of the protein heat source, it extends the time power is coupled into the resonator and the duration of the heat pulse. This produces a nonlinear relationship between Q and $\Delta\lambda_R$, and a deviation from power law behavior in the inset

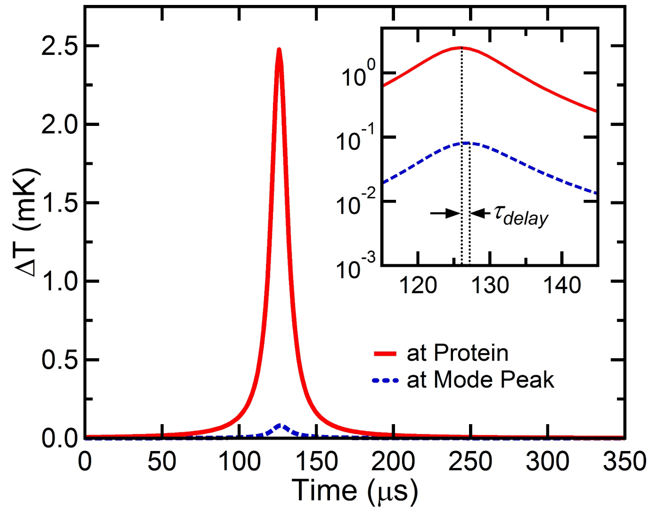

Figure 5.5: The temperature at the location of the protein (red) and mode peak (blue) as a function of time where the only heating comes from a protein exhibiting linear absorption bound to the surface of the toroidal sensor with $Q = 10^8$, $P_D = 1$ mW, and $\frac{d\lambda}{dt} = 1.35\ \mathrm{nm\,s^{-1}}$.

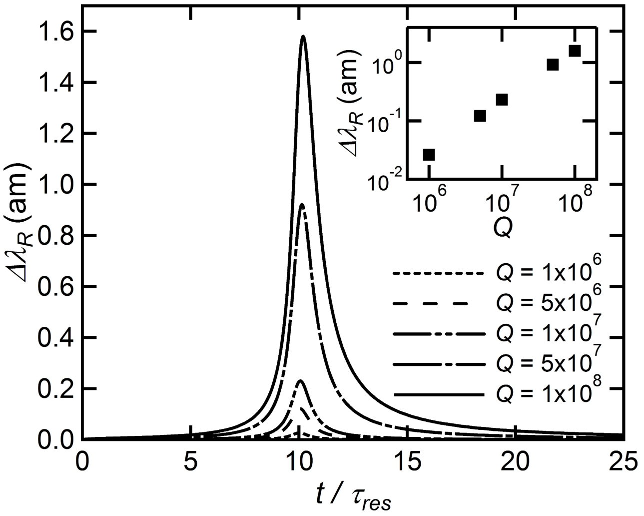

Figure 5.6: The resonance shift due to a single-molecule protein heat source for toroidal resonators ($r_a = 40\ \mu\mathrm{m}, r_i = 2.5\ \mu\mathrm{m}$) with $P_D = 1$ mW and $\frac{d\lambda}{dt} = 1.35\ \mathrm{nm\,s^{-1}}$ for varying quality factor. This shift is plotted against a relative time t/τ_{res} to simplify comparison. The maximum signal is plotted as a function of Q in the inset.

to Fig. 5.6.

We leave for future work the consideration of bulk heating, decreases in Q due to the accumulation of protein on the sensor, and nonlinear optical effects, the latter which pose a variety of challenges. Bulk heating demands that Eq. (5.10) include the first term on the right side of the equation, increasing the computational demands. Consideration of nonlinear optical effects requires additional knowledge about molecular properties that, if available in the literature, are difficult to locate.

5.8 Conclusions

Single-molecule sensitivity in WGM biosensors remains controversial due to the inability to reconcile experimental results with physical models. A review of the models to date reveals an oversimplified physical system and a failure to accurately model the single-molecule experiments. In particular, previous models ignore the exclusively transient nature WGM sensing experiments in the literature, instead adopting a steady-state assumption that precludes relevant physical processes. This time dependence implies that, as the wavelength is scanned during a measurement of λ_R, changes occur in the optical field intensity, the heat generated by the single-molecule source, the temperature profile, and the physical properties of the system. The model presented here incorporates the transient nature of the WGM experiments to predict the observed shift in λ_R, while still making simplifying physical assumptions: (i) the only heat added to the system comes from a protein undergoing linear absorption and (ii) temperature perturbations to the mode structure are negligible. We find that, in the limit of linear absorption by a single protein heat source and consequential thermo-optical effect, even the present, more rigorous model underestimates the reported sensitivity by a factor of $10^3 - 10^4$. Nonetheless, this model lays the groundwork for future studies. Present knowledge of the physical properties of biomolecules bound to the resonator surface limits our ability to model the sensor response. Data on the nonlinear optical coefficients for non-fluorescent proteins are needed, as is a fundamental understanding of energy transfer mechanisms at the single molecule level.

The authors would like to thank the Jacobs Institute for Molecular Engineering for Medicine at the California Insititute of Technology and the NASA Astrobiology Institute through the NAI Titan team managed at JPL under NASA Contract NAS7-03001 for the funding of this project, and the Ayrshire Foundation for their support in making computing resources available.

5.9 Supplemental Information

Finite Element Model

Calculating the 3-dimensional, transient temperature distribution $T(\mathbf{r}, t)$ at position $\mathbf{r}$ and time t that results from a single-molecule heat source at the interface between a toroidal WGM optical resonator and the surrounding medium is challenging. This task requires integrating the energy balance equation for an arbitrary differential volume element, an expression which may be written as

$$\rho C_P \frac{dT}{dt} + \kappa_T \nabla^2 T = \frac{\omega \alpha \lambda n |\mathbf{E}|^2}{2\pi} + h_{SM} \delta(\mathbf{r} - \mathbf{r_a}), \tag{5.12}$$

where ρ is the material density, C_P is the heat capacity , κ_T is the thermal conductivity, and $|\mathbf{E}(\mathbf{r}, t)|$ is the magnitude of the electric field. The right hand side of Eqn. (5.12) represent the generation of heat due to absorption by the bulk materials, i.e., silica and water, (first term) and heat due to absorption by a single-molecule bound to the sensor at position $\mathbf{r_a}$ giving off heat at a rate h_{SM} (second term). Here, δ represents the Dirac function.

Calculations were performed numerically, using the finite element (FE) mathematics software COMSOL Multiphysics 4.2. The present work makes the assumption that the thermal plume created by a single molecule will be small enough that the interface between the resonator and the surrounding medium may be approximated as planar, leading to the geometry drawn in Figure 5.7. The FE method allows the user to concentrate computation power on regions of the geometry over which the equations apply where the dependent variables change rapidly with position by controlling the size of local mesh elements. We take advantage of this feature by creating numerous subdomains in the geometry, within which the mesh element size is independently described to cut down on computation time by assuming changes in the temperature profile are small near the boundaries of (see Fig. 5.7b). The simulated geometry extends 20 μm into each material and 40 μm in each direction along the interface. A cubic subdomain 3 μm in length was defined at the center of the geometry with a maximum mesh size of 50 nm and surrounded by a larger cubic domain 6 μm in length with a maximum mesh size of 1 μm, which encompassed the entire region where temperature changes due to heating exceeded 10^{-7} K.

Solving Equation (5.12) requires boundary conditions that are applied to all mesh elements that touch an outer boundary of the geometry. The total volume of the system was large compared to the thermal plume that evolves during the WGM sensing experiment to allow us to apply a boundary condition at the extremities holding temperature constant at the ambient value of $T = 298$ K. The boundaries between all other mesh elements was left at their default boundary setting, which COMSOL refers to as *continuity.* This implies that temperature and thermal flux are continuous across each mesh element interface. The point at the center of the geometry, which lies on the interface between silica and water, was designated as a point

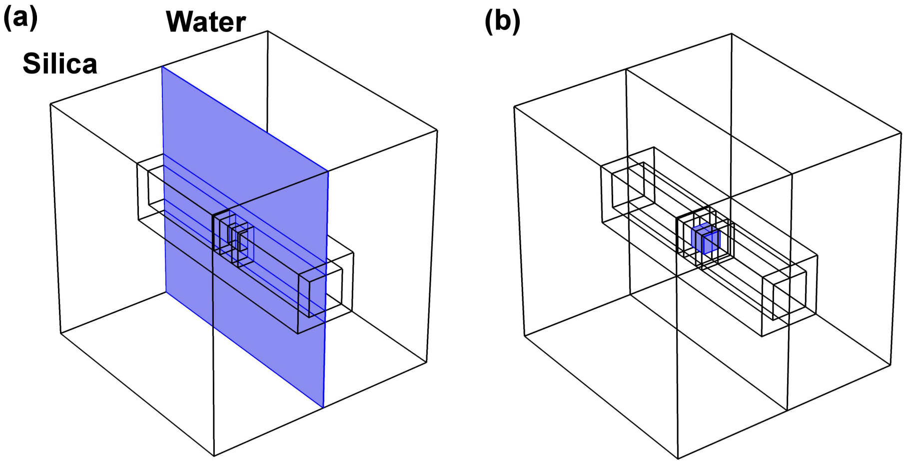

Figure 5.7: The geometry used in COMSOL Multiphysics to solve Eqn. (5.12) for the transient temperature profile resulting from the excitation of a single-molecule heat source located at what is assumed to be a locally planar interface (blue plane) between a toroidal WGM optical resonator and the water surrounding it. The interior lines are boundaries between subdomains created within the geometry to allow for convenient control over local mesh element size, reducing computation time and memory requirements.

source of heat that obeys a transient intensity function of

$$h_{SM} = \frac{\sigma \mathrm{Im}(\mathbf{S}\cdot\hat{\phi})\tau_{res}^2}{4(t-t_0)^2+\tau_{res}^2}, \tag{5.13}$$

where σ is the absorption cross-section of the protein, $\mathrm{Im}(\mathbf{S})$ is the imaginary part of the Poynting vector at the position of the protein, $\hat{\phi}$ is the unit vector in the direction of light propagation, t_0 is the time during the wavelength scan when $\lambda = \lambda_R$, and $\tau_{res} = \lambda/(\frac{d\lambda}{dt}Q)$. This expression describes the Lorentzian profile expected in the absence of bulk heating.

Since we considered resonators with varying quality factors, we evaluate the temperature profile over the geometry at a range of times that were scaled according to τ_{res}. The center of the Lorentzian profile was set to occur at $t = t_0 = 10\tau_{res}$ for all cases. For $0 < t < (t_0 - 2\tau_{res})$ and $(t_0 + 2\tau_{res}) < t < 3t_0$, the time resolution of the calculation was set to $\tau_{res}/6$, while time resolution was improved to $\tau_{res}/60$ during the part of the experiment when significant heat was being generated by the protein, i.e., $(t_0 - 2\tau_{res}) < t < (t_0 + 2\tau_{res})$.

In order to calculate the mode profile, we used methods outlined by Oxborrow [103]. This technique, which uses the axial symmetry of a WGM resonator to simplify the calculation, could not be used directly with our assumption of a locally-planar material interface. We instead mapped the mode onto the planar geometry by using the axisymmetric solution for the mode cross-section as the basis for an interpolation function in the plane normal to propagation and by assuming that the time-averaged mode does not vary in the direction of propagation. The mode profile was used for the weighted calculation of the change in effective refractive index, Δn_{eff}, experienced by the resonant light which may be approximated in terms of the electric field intensity, $|\mathbf{E}(\mathbf{r})|$, using the expression

$$\Delta n_{eff} \approx \frac{\int_V \frac{dn}{dT}\Delta T(\mathbf{r})|\mathbf{E}(\mathbf{r})|dV}{\int_V |\mathbf{E}(\mathbf{r})|dV}. \tag{5.14}$$

The electric field intensity may be easily calculated from the axisymmetric mode profile [103].

The experimental parameters used to predict the WGM optical biosensor response to the binding of a single protein molecule to the surface of an ultra-high Q toroidal resonator in the absence of bulk heating or nonlinear optical phenomena are shown in Table 5.3. Material properties for silica and water are also included in Table 5.4.

Thermal Effects in WGM Optical Resonators

Absorption by the resonator and its surrounding medium, though often negligible at low coupled power and low quality factor, can be significant for the ultra high Q WGM optical biosensors for which extreme limits of detection have been reported. The warping of the Lorentzian transmission trough that results from absorptive heating and subsequent thermo-optical resonance shift during the wavelength scan could help explain the sensitivity observed in SM1 and SM2. Though no raw data (i.e., transmission spectra) are available for those studies, we can see how similar conditions in Figure S5.8, which include 2.6 mW coupled into a toroidal resonator in water with $Q \approx 10^7$ at $\lambda = 765$ nm, can produce significant broadening of the transmission trough for positive scan rate and narrowing of the trough for negative scan rate. This implies that the methods described above, which assume a Lorentzian time profile for the transient point source of heat, may significantly underestimate the amount of heat put into the system. If taken with a positive wavelength scan rate, data collected during a sensing experiment may be influenced by a heat source with a lifetime that could be orders of magnitude longer than τ_{res}.

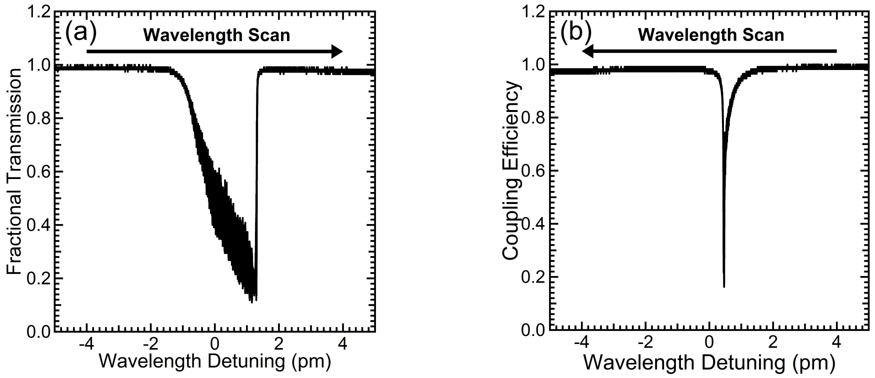

Figure 5.8: Transmission spectrum for a toroid of major radius $r_a = 40$ μm and minor radius $r_i = 5$ μm and $Q \approx 10^7$ at wavelength scan rates of (a) $\frac{d\lambda}{dt} = 7.6$ nm/s and (b) -7.6 nm/s. The resonator is submerged in water and is being excited using a 765 nm external cavity tunable laser, with a maximum coupled power of 2.6 mW. The difference in resonance linewidth and transmission minimum is due to thermal distortion of the Lorentzian trough, where λ_R shifts during the scan when light is absorbed and the system warms. Since this warming results in a red shift of λ_R, a positive scan rate leads to an artificially broad line and a negative scan rate yields an artificially narrow line.

Table 5.3: Experimental Parameters for Modeling WGM Biosensing Experiment

Parameter	**Symbol**	**Value**
Quality factor	Q	1×10^8
Driving power	P_D	1 mW
Wavelength scan rate	$\frac{d\lambda}{dt}$	1.35 $\frac{\text{nm}}{\text{s}}$
Wavelength Scan Duration	τ_{scan}	5 ms
Driving pulse FWHM	τ_{res}	5 μs
Energy flux at the protein	$\text{Im}(\mathbf{S})$	6×10^{13} $\frac{\text{W}}{\text{m}^2}$

Table 5.4: Physical Properties of Silica and Water at 298 K and 680 nm

Property	**Symbol**	**Units**	**Silica**	**Water**
Thermal Conductivity	κ_T	$(\frac{\text{W}}{\text{m}\cdot\text{K}})$	1.38 [137]	0.58 [137]
Density	ρ	$(\frac{\text{kg}}{\text{m}^3})$	2203 [137]	997 [137]
Heat Capacity	C_p	$(\frac{\text{J}}{\text{kg}\cdot\text{K}})$	703 [137]	4186 [137]
Thermo-Optical Coefficient	$\frac{dn}{dT}$	$(\frac{1}{\text{K}})$	1.3×10^{-5} [1]	-9.9×10^{-5} [135]
Refractive Index (Real)	n		1.4694 [110]	1.33322 [138]
Refractive Index (Imaginary)	k		1.74×10^{-10} [139]	1.41×10^{-8} [140]
Absorption Coefficient	α_{abs}	$(\frac{1}{\text{m}})$	0.0034 [139]	0.28 [140]

Chapter 6

Detection of Biomarkers for Respiratory Distress in Exhaled Breath Condensate

Our understanding of asthma was fundamentally altered when it was revealed to be not a single disease but rather a variety of phenotypes involving various tissues and molecular factors. The exact nature of the pulmonary inflammation is phenotype-specific, and a lack of information about the state of the respiratory system during an episode can hinder a diagnosis. A library of biological markers of pulmonary inflammation are being used to try to probe these different disease states, but specimen collection becomes a challenge when typical methods such as bronchoalveolar lavage, sputum induction, and bronchoscopy pose health threats and significant discomfort to the patient. Other specimen types, such as urine or plasma, offer only information about systemic inflammation.

Exhaled breath condensate (EBC) has emerged as a non-invasive alternative to these methods, where the aerosols in breath are condensed and collected in the liquid phase [141, 142]. This method is an effective and way to sample both volatile and non-volatile species within the respiratory tract, and has proven to be useful tool in asthma research due to its ease and repeatability. Specimen collection typically takes 10 minutes and, unlike with urine or plasma, offers localized information about the lungs at a specific point in time. This method has played an integral role in the study of two particular classes of biological molecules that describe respiratory conditions.

6.1 Biomarkers for Oxidative Stress

One such group of biomarkers is the leukotrienes (LTs). They are the result of arachidonic acid breakdown in the cell membrane first by 5-lipoxygenase (5-LOX) and then by another enzyme. Specifically, leukotriene LTC_4 synthase produces the cysteinyl leukotrienes, which include LTC_4, LTD_4, and LTE_4, and leukotriene A_4 hydrolase produces LTB_4. They are small molecules (molecular weight $\approx$330 g/mol) and are understood to be proinflammatory factors released by mast cells and eosinophils that are capable of contracting airway smooth muscles and increasing mucus secretion and vascular permeability. Elevated levels of the cys-LTs have been found in asthmatic adults and children [143, 144, 145], and Balanzá et al. [146] demonstrated a 20-fold increase in LTB_4 in children with persistent asthma, but only a 2-fold increase in children with episodic asthma.

Another common species found in conveniently high concentrations in EBC are isoprostanes, a class of small molecules (molecular weight $\approx$350 g/mol) that result from the free radical-catalyzed peroxidation of arachidonic acid as opposed to the naturally-occuring cyclooxygenase-catalyzed peroxidation [147]. For this reason, they make excellent markers for the oxidative stress level in the respiratory system when collected in the EBC. The prevalent regioisomer of this class is 8-isoprostane (8ip), also referred to as 15-F_{2t}-isoprostane, 8-epi PGF2α, and isoprostane-$F_{2\alpha}$-III. It is present in EBC at elevated levels in patients with asthma [148], cystic fibrosis [149], and sleep apnea [150] as well as in patients who smoke [151]. Interestingly, the same 2010 study by Balanzá et al. [146] that reported distinctly different LTB_4 levels according to episodic or persistent asthma also reported a disproportionately smaller difference in 8ip levels between the two groups, implying that a combination of these two markers could provide even more information about nature of the condition for a given patient.

It is rather fortunate that species such as leukotrienes and 8-isoprostane are present at such high concentrations in EBC, but it is unclear whether more reliable or informative biomarkers are present below the detection limits of those methods currently used or whether subpopulations could be better resolved with more sensitive analytical methods. Zanconato et al. observe in their 2004 study that 8-isoprostane levels in the EBC of a population of children with unstable asthma appears bimodal, suggesting the "heterogeneity

Table 6.1: Local Concentrations of 8-isoprostane in the Body [3]

Organ	**Concentration**
Liver	8-114 ng/g
Kidney (urine)	57-390 ng/g
Blood	20-80 pg/mL
Lung	5-60 pg/mL

of asthma phenotypes in subjects with difficult-to-control asthma" [145]. Analytical methods are limited for these measurements. Small molecules such as leukotrienes and 8-isoprostane are typically measured with either gas chromatography/mass spectrometry (GC/MS), liquid chromatography/mass spectrometry (LC/MS), or enzyme immunoassays (EIAs), but studies looking at the proteins found in the EBC use EIAs, flow cytometry, or enzyme-linked immunosorbent assays (ELISAs) [141]. The published limits of detection for all of these methods are between 1 and 10 pM. Unfortunately, the levels present in healthy subjects is no more than a factor of 2-4 higher than that limit (see Table 6.1). While EBC gives researchers a valuable tool to collect specimens that can accurately describe respiratory health, there remains a clear need to evaluate these samples with more sensitive techniques in order to search for biomarkers that current methods cannot detect. Increased sensitivity would make it possible to mine these samples for as much information as possible.

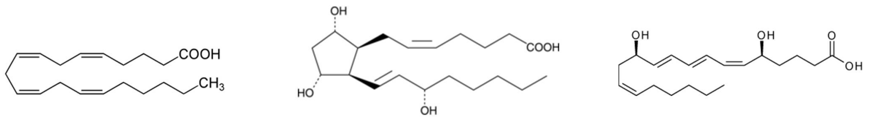

(a) Arachidonic Acid (b) 8-isoprostane (c) Leukotriene B4

Figure 6.1: The structures of arachidonic acid and two of its derivatives most useful as biomarkers of oxidative stress

6.2 Whispering Gallery Mode Optical Biosensors

Whispering gallery mode (WGM) optical biosensors have demonstrated extraordinary sensitivity for detecting the specific binding of proteins to their surfaces via immobilized antibodies [1, 6]. These round, microscale, dielectric devices trap light circulating around their periphery. Their smooth walls continually steer the light inward and minimize losses. When the trip around the periphery is equal to an integer number of optical cycles, the light is in phase with itself and may undergo constructive interference. The intensity of this resonant light grows until the input rate is balanced by the cumulative losses of the resonator. The quality factor, Q, the figure of merit often used to characterize loss in a resonator, is the ratio of the energy stored in the cavity, W, to the energy lost per optical cycle. It may be expressed in terms of the resonant frequency, ω_R, and the power coupled into the resonator, P_C, as $Q = \omega_R \frac{W}{P_C}$. At steady state, $P_C = P_D$, where P_D is the readily measured dissipated power. Though a number of mechanisms exist through which light may be lost from the resonator, the scattering due to surface roughness at the interface between the resonator and surrounding medium and the absorption of light by these materials are the two most significant.

Microtoroidal resonators have demonstrated quality factors of $> 10^8$ in water, and have been used to develop label-free bioassay sensors with attomolar (10^{-18} M) limits of detection for proteins [1] and small molecules [152] in both buffer and complex biological media [1]. While other devices, such as surface plasmon resonance (SPR), have acheived picomolar sensitivity, only the WGM optical biosensor has demonstrated label-free detection with this extreme sensitivity. The markers of interest here are much smaller than the species commonly studied in the literature. The present work examines the potential of the WGM optical biosensor for the previously unexplored class of diagnostic molecules.

The established performance of WGM biosensors [72, 73, 74] makes them an excellent candidate for use in low-concentration medical diagnostic and analytical measurements. Here we demonstrate that these devices can exceed the detection limits of current methods for sensing small molecule biomarkers that are found in EBC, thereby expanding the value of that non-invasive sampling method and accelerating its adoption into standard medical practice. As there appears to be no standard means of analysis for quantifying biomarkers of oxidative stress in the respiratory track [3], this exercise stands to present a technique to both unify and improve this process.

6.3 Detection of Model Biomarkers

To demonstrate the utility of WGM biosensors for detection of biomarkers in biological samples we choose as our analytes 8ip (M_w 350 g/mol) and the small protein Interleukin-2 (M_w 15300 g/mol), species with molecular weights that differ by nearly two orders of magnitude. While we discuss the significance and convenience of 8ip, it is worth noting that proteins in the interleukin family have been detected in EBC and may also serve as biomarkers for interrogating respiratory distress [153, 141]. These cytokines serve as intercellular signalling molecules during inflammation and immune response. Interleukin-2 [14] in particular has been used many times over as a model system with which to validate biosensor performance [1, 54], partly because monoclonal antibodies are available for its human variant.

The experiments that demonstrated the extreme sensitivity of the microtoroidal WGM sensor employed a New Focus Velocity$^{\mathrm{TM}}$laser operating at a wavelength of $\approx$ 680 nm. Unfortunately, that mechanically-tuned laser was too delicate for reliable use in routine sensing, so an alternative source was sought for this application. Yariv and coworkers [154] have developed a current-tuned distributed-feedback (DFB) laser that is much better suited for use in the long-term development of WGM biosensing instruments. The DFB laser produces a linear sweep in optical frequency by using an interferometer to combine the laser output with a delayer version of itself. As the frequency is swept, the light that is transmitted through different lengths of optical fiber differ in phase, producing an optical “beat" pattern when combined and sent to a photodetector. The resulting sinusoidal signal is used as a feedback signal to control the current source responsible for tuning the optical frequency. Further details of this laser system are provided in [154].

This laser is not continuously tuned in a symmetric sawtooth patthern like the more common external cavity laser (ECL), which is described in Chapter 3 and illustrated in Fig. 6.2. Instead, it is swept in a linear frequency “chirp," as illustrated by the blue line. This optoelectronic swept frequency laser (OSFL) represents a considerable improvement over ECLs due to its robust design that has no moving parts. Building

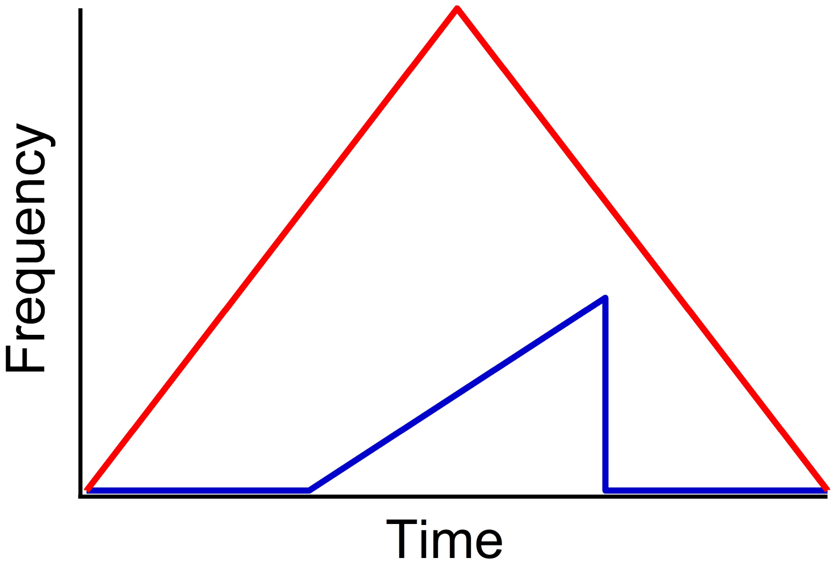

Figure 6.2: Typical frequency scan profile shape for external cavity laser (red) and chirp laser (blue). Note that the ECL has a wider tuning range; however, the OSFL laser has no moving parts so it may attain a far greater range of scan rates.

one also costs 10-40% of what most commercially available ECLs cost. Chirp lasers are limited by the wavelength and linewidth laser, however. Laser diodes that operate at visible wavelengths that are suitable for current tuning are rare because, unlike for near-infrared wavelengths such as 1310 nm and 1550 nm used in telecommunications, there is no great industrial need for them. Moreover, the inexpensive near-infrared laser diodes lack the diffraction gratings used in ECLs to produce narrow linewidths of < 1 MHz, increasing the noise of biosensing data collected collected using OSFLs relative to the alternative. While efforts to build an acceptable OSFL laser with output of $\lambda < 1310$ nm to reduce absorptive losses due to water are ongoing, the experiments described below were performed using a 1310 nm OSFL.

Experimental Methods

In performing sensing experiments with Interluekin-2 (IL2) and 8-isoprostane (8ip) we hope to clarify two performance characteristics of WGM sensors: (i) the limit of detection for each type of analyte, and (ii) the repeatability of the endpoint measurement that might be used to quantify the presence of the analyte in a biological sample. The first measurement comes down to the straightforward task of identifying the concentration of analyte below which the sensor gives a signal indistinguishable from noise (see Section 2.4). The second is more difficult because it requires excellent control over the sensor fabrication process. For microtoroidal WGM biosensors, this process involves lithographically definining a silica disk, gas-phase etching to remove silicon some from beneath that disk, and reflowing the disk using a CO_2 laser. This process is discussed in greater detail in Chapter 3. Each step involves variability that is compounded throughout the process, all but eliminating the chances of being able to establish repeatability using different devices. Instead, we focus here on using a single sensor and regenerating its surface between experiments.

As a first step toward accomplishing these goals, we conduct a series of experiments using a microtoroidal WGM biosensor to detect Interleukin-2 in buffer by immobilizing monoclonal anti-IL2 on the sensor surface. The injection port was a 23-gauge stainless steel tube, connected to a syringe mounted on a syringe pump. The injection tube was placed roughly 5 mm away from and aimed directly at the toroid being used in the experiment such that the tapered optical fiber waveguide was between the injection tube and the sensor. An open flow cell was constructed by attaching a glass coverslip cleaned in pirhana solution (30 vol% standard hydrogen peroxide solution, 70 vol% pure sulfuric acid for 60 minutes followed by a rinse in ultrapure water) to a stainless steel sample holder using minimal superglue. The glass coverslip is glued to and cantilevered off of a 1 mm tall spacer made from a small piece of a silica microscope slide cut to be as wide as the sample holder. A chip with a linear array of toroidal resonators was also glued to the stainless steel holder.

After waiting 30-60 minutes for the cyanoacrylate adhesive to react completely with atmospheric water, the sample holder was mounted on a piezo block for accurate positioning of the resonators with respect to the waveguide. The flow cell was flooded carefully by hand using a micropipette, adding buffer simultaneously on both sides of the taper to minimize the risk that capillary forces and water surface tension would break the waveguide as the cell filled. The volume of the flow cell varies each time one is made, but most are between 400-600 μL. A flow rate of 50 μL/min was used for all experiments.

Light from the OSFL was coupled into an optical fiber containing a tapered section to facilitate coupling of light into the optical resonator sensor. The tapered optical fiber waveguide was fabricated by pulling a piece of stripped and cleaned fiber over a hydrogen flame. The light transmitted through the waveguide was sent to a low-noise photodetector (Thorlabs, 200 MHz) that was connected to an oscilloscope (Tektronix TDS-2024B, 2000 points per scan). The pulse function sent to current source responsible for tuning the OSFL output wavelength was used to trigger the oscilloscope. Data collection involved the capture of entire transmission spectra, which facilitated the measurement of coupled power, Q, and $\Delta\lambda_R$. Raw data was acquired with a time resolution of ≈ 1 second using a script written in Igor 6.1 (Wavemetrics) to communicate with the oscilloscope. A constant coupling was maintained during the experiment through manual manipulation of the piezo controller according to live feedback from the depth of the Lorentzian trough in the transmission spectrum shown on the oscilloscope.

Protein solutions were made in a buffer consisting of 100 mM 4-(2-hydroxyethyl)-1-piperazine ethanesulfonic acid (HEPES), 100 mM NaCl, and a pH of 7.5 that was stored at room temperature. Phospate buffered saline, though a popular and convenient simulation of biological conditions, were unsuitable for our experiments as the phosphate absorbs light far more efficiently at 1310 nm than at 633 nm, leading to artifacts in the data. Protein stocks were stored in 20 μm aliquots at -20 °C, and solutions were maid daily and stored at 4 °C until 30 minutes before an experiment to allow for thermal equilibration at room temperature. The flow cell was flushed with 3 mL of buffer before any experiments were performed to remove any accumulated dust particles that may have been deposited during the the construction and subsequent curing of the flow cell structure.

Surface functionalization was achieved by first applying a nonspecifically-bound layer of Protein G to the bare silica surface. A 100 nM solution was introduced into the cell until the sensor showed a new steady-state value of λ_R to reflect the saturation of the sensor surface. The cell was then rinsed with 3 mL of buffer before flowing a 100 nM solution of antibody into the cell. Protein G is known to bind to the FC region of an antibody, ensuring that the molecular recognition regions of the molecules are oriented so that they may specifically bind their antigen. After the surface is saturated with antibody, the cell is rinsed again. The monoclonal antibody used for IL-2 was purchased from Invitrogen while the polyclonal antibody for 8ip was purchased from Cayman Chemicals.

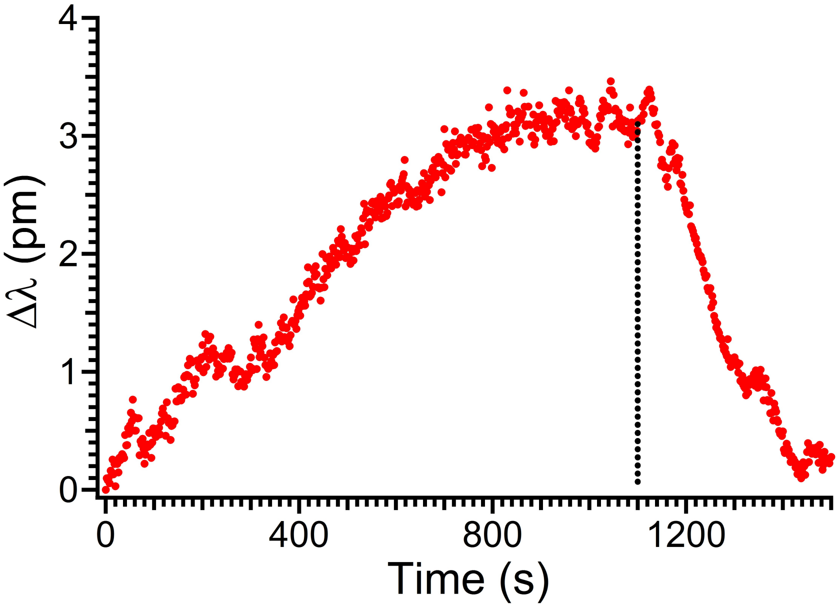

Figure 6.3: Typical sensor response for a microtoroid resonator in water at 1310 nm exposed to 50 μL/min flow of water. The dotted line marks the point at which flow was shut off.

Preliminary Results

In all experiments, we observed a sensor response upon flowing of buffer into the cell without protein present to adsorb to the device. Even when ultrapure water is flowed at 50 μL into the cell, we observe a reversible increase in the resonant wavelength, as demonstrated in Fig. 6.3. It is well-known that water absorbs light efficiently at 1310 nm, and the resulting heating is likely behind this effect. Just as described in Chapter 4 for the case of mass transfer, a temperature boundary layer forms in the region close to the sensor where thermal diffusion is the dominant mode of energy transfer and convection is locally negligible due to viscous forces. We have shown that the thickness of this region, δ, decreases with increasing flow velocity *or* decreasing size of the flow obstacle.

Increasing the inlet flow rate might then produce a thinner layer over which convection is unable to rinse away the water warmed by the optical field than at lower flow rates. Since the thermal flux q obeys Fourier's Law according to $q = -\kappa_T \nabla T$, where κ_t is the thermal conductivity and T is the temperature, the thinner boundary layer that results from an increased inlet flow rate will also lead to an increased temperature gradient at the surface of the resonator. Ultimately, heat will be better removed from the warming resonator under these conditions than if the inlet flow were small. Any change in temperature T of a material is accompanied by a change in refractive index n according to the thermo-optical constant $\frac{dn}{dT}$. As a result, the sensor will experience a change in the resonant wavelength when the temperature around the the device is perturbed by flow according to

$$\frac{\Delta\lambda_R}{\lambda_R} = \frac{\Delta n_{eff}}{n_{eff}} = \frac{\frac{dn}{dT}\Delta T}{n_{eff}}. \tag{6.1}$$

The thermo-optical constant of water is -9.9×10^{-5} K^{-1} [135], and any increase in the water temperature will produce a decrease in the resonant wavelength.

According to Eq. (6.1), this would suggest a blue shift in the resonance in response to absorption of light by the water, however this effect can only be observed when comparing the λ_R with the value measured in the limit of zero absorption. Instead, multiple processes are occurring simultaneously that generate both red and blue shifts in the resonant wavelength. Exposing the sensor to flow, thereby creating thermal boundary layers, washes away some of this "warm" water and replaces it with water at room temperature. In effect, this "cooling" of the water that has interacted with the optical mode produces a red shift. However, a more steep boundary layer increases the rate at which energy diffuses away from the resonator, lowering its temperature. The thermo-optical coefficient of glass is 1.3×10^{-5} K^{-1}, so cooling the resonator would yield a competing blue shift. Since silica absorbs so little light at 1310 nm, there is likely very little heat building up in the silica resonator compared to that due to absorption in the water. Accordingly, the net effect observed experimentally and shown in Fig. 6.3 upon flowing water around the WGM biosensor is a red shift because the removal of warm water from the mode is dominant.

A systematic study of this effect is ongoing. To date, this effect is unpublished, but would significantly impact the development of WGM biosensors at near-IR wavelengths that aim to cut costs by using inexpensive tunable lasers common to the telecommunications industry. This effect can be managed during a sensing experiment despite the notion that one would be unable to parse the respective contributions from biomolecular adsorption and fluid flow. This can be accomplished by collecting transient data while flowing a protein solution until the signal reaches a steady state due to saturation of surface binding sites, followed by turning off the flow to reveal the steady-state signal due exclusively to the protein. The relative resonance shift from the beginning of the measurement until the system stabilizes in the absence of flow is the true endpoint datum.

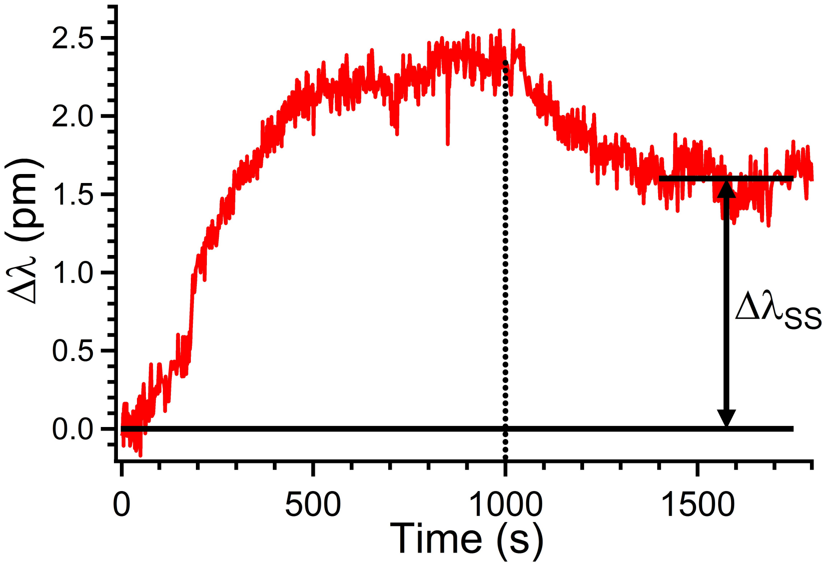

Figure 6.4: Detection of 100 fM Interleukin-2 in buffer using a toroid with Q=2.0 × 10^5, a flow rate of 50 μL/min, and a testing wavelength of 1310 nm. The dotted line marks when flow was shut off, and the endpoint resonance shift is marked as $\Delta\lambda_{SS}$

This method is demonstrated in Fig. 6.4 for the specific adsorption of 100 fM IL2. It clearly demonstrates how a single endpoint resonance shift, labeled $\Delta\lambda_{SS}$, is measured. It also shows the typical dual steady-state signal levels corresponding to the presence and absence of flow around the toroid. There is a signal-to-noise ratio of SNR>6:1, indicating that the true sensitivity of this assay is in the range of 1-10 fM for this analyte/buffer combination. As a point of reference, these data suggest that WGM optical biosensors outperform commercially available biosensor technologies such as surface plasmon resonance (SPR), which typically feature limits of detection (LODs) above 100 fM for label free assays.

Identical procedures were used to detect 8ip in solution as well. It was unclear beforehand how well WGM biosensors would be able to resolve specific adsorption of 8ip due to its small size. Fig. 6.5 shows the cumulative resonance shifts measured during a series of 8ip sensing experiments where successively higher concentrations of the analyte were introduced into the flow cell. Just as in the case for IL2 detection, we measured the steady state value for $\Delta\lambda_{SS}$ in the absence of flow. The small ridges that appear in the signal within a single sensing experiment, more clearly visible in the inset to Fig. 6.5, correspond points when water drops fell off of the sample holder and caused vibrations in the air-water interface around the flow cell. These vibrations cause motion in the tapered fiber waveguide and, subsequently, coupling-induced resonance shifts as the amount of power in the cavity changes. Fig. 6.6a shows the isolated sensor response to the specific adsorption of 100 μm 8ip. Note that the analyte concentration is a factor of 10^6 higher than that in Fig. 6.4, but the signal is only a factor of 3 larger. Fig. 6.6(b) shows a portion of the dynamic range for the microtoroidal WGM biosensor at 1310 nm, but it allows us to project a LOD of roughly 1-10 pM based on the SNR of the measurent.

It is important to keep in mind that these experiments are the beginning of our efforts to demonstrate WGM biosensor utility for detection of biomarkers. Our results are encouraging, especially considering that we tested at a wavelength of 1310 nm (limiting our sensitivity) and still observed LODs below the relevant concentrations of these analytes in the body. Our current detection limits for 8ip are similar to the techniques currently in use (LCMS, fluorescence assays). We hope to perform these measurements using 633 nm light, which will likely show a 10-1000 fold improvement in sensitivity compared to the present work. This will also allow us to establish a superior sensing detection method for 8ip and create opportunities to apply WGM biosensors to analytes that may be of even more use in diagnosing disease but are present at too low of concentrations for current analytical techniques.

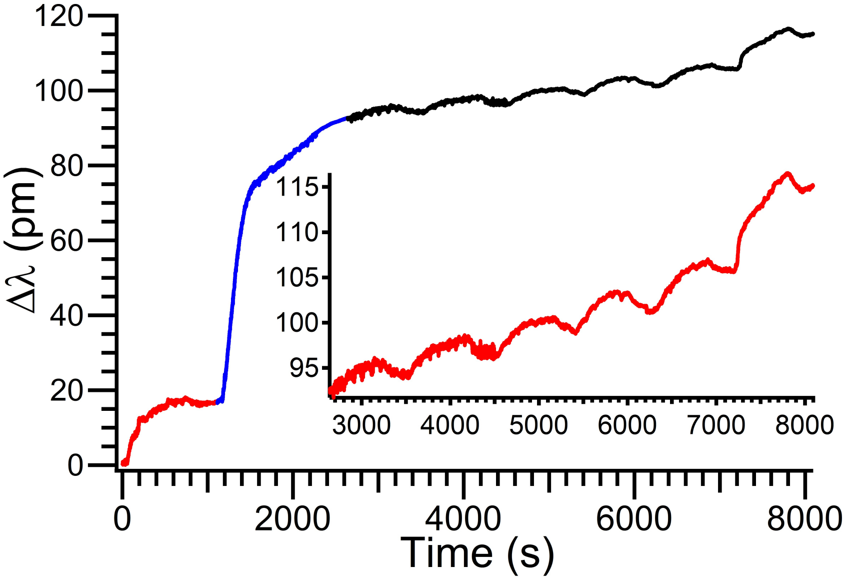

Figure 6.5: Detection of 8-isoprostane in buffer using a toroid with Q=4.2 × 10^5, a flow rate of 50 μL and a testing wavelength of 1310 nm. The data collection was stitched together to illustrate cumulative resonance shift. First Protein G (red) then polyclonal anti-8ip (blue) were allowed to adsorb. Next, six successively more concentrated 8ip solutions were flown into the cell (100 pM, 1 nM, 10 nM, 100 nM, 1 μM, and 10 μM). The inset expands this part of the curve for clarity.

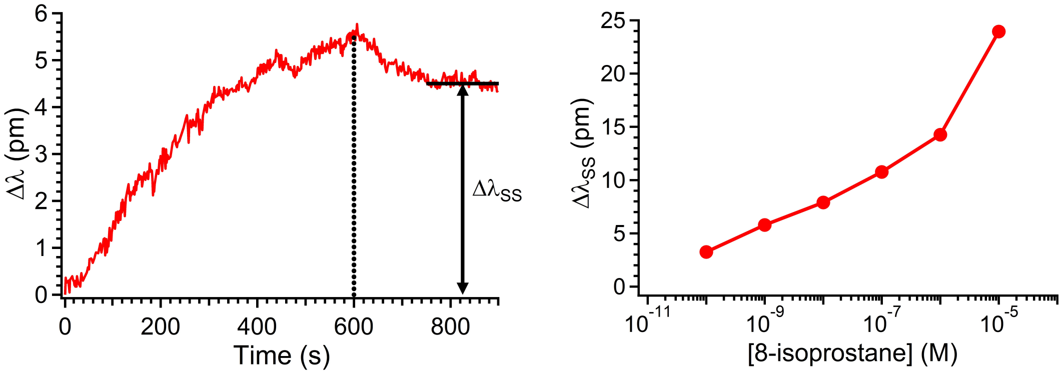

(a) Sensing 100 μM 8ip

(b) Dynamic Range Sensing Data for 8ip

Figure 6.6: (a) This sample data for 100 μM 8ip appears to saturate before flow is turned off (dotted line), at which point it reaches a new steady state. The endpoint data sought in this measurement is the value of $\Delta\lambda_{SS}$, the true steady state resonance shift. (b) By collecting this endpoint resonance shift and plotting against the concentration of 8ip that elicited that shift, we have a partial dynamic range curve for this system.

Chapter 7

Conclusions and Future Work

7.1 Summary

Though whispering gallery mode optical resonators were first characterized over twenty years ago, it is important to remember that they have only recently been put to use as chemical and biological sensors. During this developmental stage of the technology, it is critical that researchers continue to scrutinize all available data and models in order to avoid propagating misconceptions or errors that would delay progress toward a useful instrument. Because of their potential to help answer scientific questions, it is easy to forget that the goal for those who use any techology as useful and promising as WGM sensors should always be to make it more available and reliable. With this in mind, I present here my work to examine the various transport phenoma that contribute to the limiting behavior of WGM sensors and to explore ways researchers may take advantage of their extraordinary potential.

I begin by introducing the field of biosensors and how WGM sensing represents the state of the art in this arena. Explaining the principles behind how they may be used for biosensing, I discuss the details of their fabrication and incorporation into an apparatus to perform sensing experiments. This involves carefully positioning a waveguide with respect to a resonator and enclosing this assembly in a flow cell. I share some of the lessons I learned in assembling the equipment required for this delicate process and describe some of the techniques I have come to adopt as these details seldom appear in literature (to the great dismay of those beginning in this field).

Drawing conclusions with an analytical tool like the WGM sensor requires a fundamental understanding of how it operates. This understanding is the sieve through which artifacts may be identified and meaningful data may be extracted. With this in mind I present an exhaustive analysis of the physical models proposed in the literature to describe and predict sensor behavior. I reveal that a variety of misinterpretations of the relevant physical processes have contributed to the misconception that this behavior was well-understood, and go on to present a roadmap for calculating the resonance shift resulting from the interaction between a single biomolecule and the WGM. Though the immediate goal of such a calculation is to validate via theory the single-molecule sensitivity observed previously by Armani et al. [1], the study is intended as an aid and impetus for all researchers in the field to carefully consider the effect of experimental parameters. By applying current understanding and physical models, our results predict that these devices are have a sensitivity too low by a factor of $10^3 - 10^4$ to explain these experimental observations.

The physical processes previously assumed to be relevant to WGM sensing experiments are inadequate. I go on to propose the role that nonlinear optical phenomena may play in ultra high-Q WGM biosensor sensitivity, focusing in particular on 2-photon absorption. The likely occurrence of this effect would suggests that a single protein molecule adsorbed to a WGM resonator gives off much more heat when intensely illuminated on-resonance than previously estimated. Including 2-photon absorption in our physical model predicts single-molecule resonance shifts comparable to those observed in Ref. [1].

The extraordinary single-molecule sensing data mentioned above also inspired a rigorous consideration of fluid flow and its effect on observed binding kinetics. In the ultralow concentration limit, the analysis of this process can draw heavily from the filtration literature where particle capture from dilute air streams has been described extensively. My work shows how concentration boundary layers that form around objects in flow can greatly enhance the rate at which single molecules or other discrete entities will be adsorb to a sensor. Thin boundary layers yield increased flux of analyte to the sensor surface, and I demonstrate how these layers become thinner for objects with smaller radius or for higher uniform flow rates. Of particular note is the phenomena predicted for microtoroidal resonators, which benefit from anisotropic boundary layer formation due to their minor and major radii. Spheres have only a single characteristic radius and experience larger, symmetric boundary layers and may therefore demonstrate slower adsorption rates than microtoroids, an important result considering the fact that the WGM sensing literature includes results for both geometries. These results have important implications for the design of flow systems and resonator geometries for sensing applications that must conserve sample, as in the case of medical diagnostics.

I further explore the advantages of WGM sensors over other technologies for biomolecular detection applications by demonstrating quantitative sensing of the small molecule 8-isoprostane (8ip) at sub-picomolar concentrations. This species is used as a biomarker for oxidative stress in the body, but has proven to be a particularly attractive target for probing the conditions in the respiratory track. Sampling a patient's airways has always involved invasive and often dangerous bronchoalveolar lavage techniques, but recent advances in collecting and analyzing exhaled breath condensate (EBC) provide a new and potentially far less traumatizing method. The biomarker 8ip is present at concentrations too close to the detection limits of other analytical techniques to resolve key details in the data collected. I demonstrate that while WGM biosensors using 633 nm resonant light may be able to detect at concentrations as low as 10-100 fM of 8ip in buffer, a more affordable and robust chirp laser using 1310 nm resonant light can still match the sensitivity of current analytical techniques applied for this purpose.

7.2 Future Work

There is still a great deal of work to be done to prepare WGM sensing for the transition into a viable instrument. True quantitative sensing will require either a model to account for *all* experimental parameters (likely a computational nightmare to implement) or a convenient method for calibration. Moreover, there is a need for experimental demonstration of how the resonance shift scales with these parameters, including Q, $\frac{d\lambda}{dt}$, and P_D. Identifying parameters that do no significantly influence the sensor response would decrease the number of constraints that exist when designing and scaling up sensor fabrication processes. How the sensor response changes according to analyte physical properties, such as the molecular weight, M_w, the thermo-optic coefficient, $\frac{dn}{dT}_a$, and the hydrophobicity, will also be useful when evaluating applications for these devices. For example, protein biomarkers can be detected at lower concentrations than small molecule (e.g., 8ip) biomarkers because of the difference in molecular weight.

While the ultimate task of how to fabricate these virtually imperfection-free devices with as little variability as possible may appear daunting, the solution may lie in rethinking the entire laser-waveguide-resonator design. Already devices with integrated waveguides [155, 156] and narrow-linewidth tunable lasers without external cavities [154] have been developed. A great deal of work lies ahead incorporating these features into a single instrument, possibly even a single device.

These lines of research represent the next logical steps for anyone in the field of WGM sensing to build upon the results I present here. However, my work has focused on questions particularly well-suited for investigation by a chemical engineer, work that matches the expertise and skill set of those in the Flagan Lab. With that in mind I wish to highlight some of the interesting chemical engineering questions that arise from my work and describe what steps might be taken to explore these topics.

Additional Complexity in Mass-Transfer Analysis

Mass-transfer effects play a role in the analysis of all biosensor data because the transient response will always depend on two concurrent process that occur on independent timescales–reaction and diffusion. As my work on boundary layer formation and enhancement of WGM sensor response demonstrates, even in the presence of fluid flow it is diffusion that is ultimately responsible for the flux of analyte to the sensor surface. In the case of boundary layer development, that diffusion occurs over a shorter distance than if there was no flow.

My current work treats analyte binding as though it were particle capture by a filter fiber in flow. This simplification includes the convenient assumption that binding occurs immediately and irreversibly, however that is not the case for WGM sensing experiments. An antibody-functionalized resonator exhibits a binding equilibrium with the analyte in the solution, with finite association and dissociation rates. A full analysis of mass-transfer effects for these experiments requires that this feature be included in the model.

I have already seen from my modeling in Chapter 6 how the boundary layers that form around a WGM biosensor in flow are smaller upstream than downstream. This produces a molecular flux that is greater at the most upstream point of the sensor (on the equatorial plane) than the most downstream point. For my purposes here I will refer to these points as nodes. Preliminary 2-dimensional modeling of flow around a cylinder, including characteristic binding affinities between interleukin-2 (analyte) and its antibody (targeting species), shows that the antibodies saturate at the upstream node faster than they do at the downstream one. Fig. 7.1 demonstrates this trend and gives greater detail about the surface concentration profile of bound interleukin-2 over time.

The WGM biosensor is typically used to report the shift in resonant wavelength, a quantity integrated over the entire portion of the device where material may interact with resonant light. Alternatively, the quality factor may be used to gather localized information about binding because of its dependence on surface scattering. The presence of any inhomogeniety will serve as a point of scattering and reduce the Q. If binding at the upstream node is significantly faster than at the downstream node, a “hot spot" may be created upstream and scatter light. Similarly, a “cold spot" at the downstream node could scatter light due to the low density of adsorbed material, which likely based on how abruptly such a cold spot appears to develop along the resonator surface in Fig. 7.1b.

The anisotropic binding that results from stagnation point flow directly affects the shape of the transient response curve because the resonant wavelength only stops shifting when the entire system is at equilibrium, which occurs only when adsorption balances dissociation rates everywhere on the device. Fitting a function to this curve is a crucial step in measuring the binding reaction rate constant for a given targeting species and analyte pair. Any distortion to this shape will make the curve fitting process less accurate. It appears from Fig. 7.1b that the difference between the surface concentration at the upstream and downstream nodes is never large enough where the binding at one point is limited by transport while the other is limited by reaction rate.

I think there is a great deal to be learned from continuing this work, especially because such a change in Q with analyte adsorption pattern implies that the sensitivity of the device is another transient quantity in a collection of properties that are already complicated functions of time. This means that the following

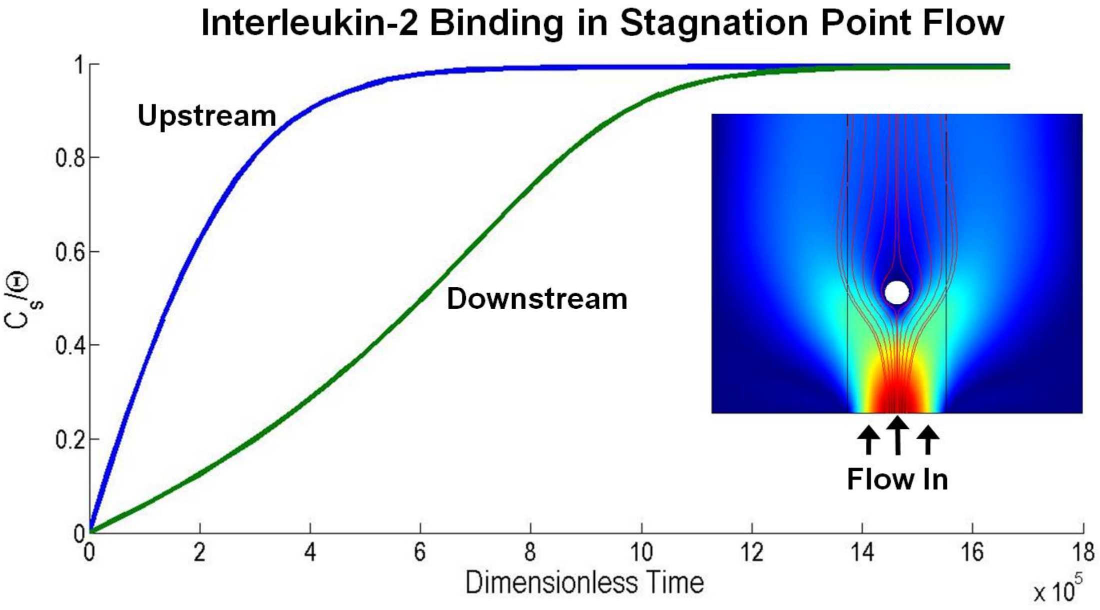

(a)

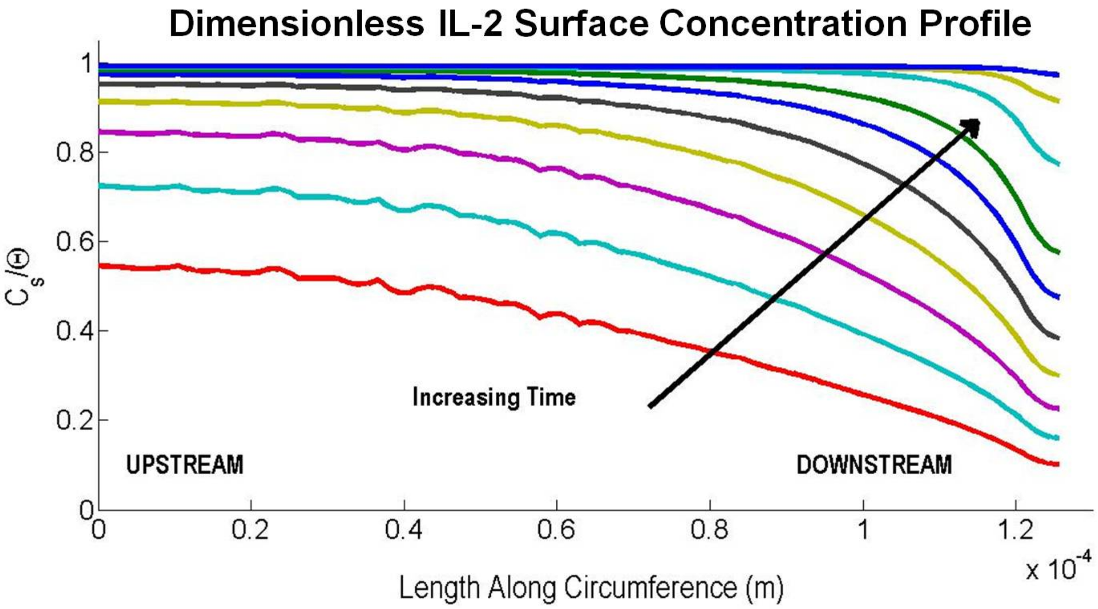

(b)

Figure 7.1: Modeling results for stagnation point flow around a cylinder with adsorption of IL-2 to its antibody. Upstream flowrate is 100 μL/min. (a) Dimensionless surface concentration of bound IL-2 at upstream node and downstream nodes as a function of dimensionless time (with respect to characteristic desorption timescale). Flow geometry as depicted in inset, with red lines depicting streamlines and cylinder diameter of 80 μm. (b) Dimensionless surface concentration of bound IL-2 as a function of arc length from the upstream node ($x = 0$ m) to the downstream node ($x = 1.26 \times 10^{-4}$ m). Each curve corresponds to a singe point in time.

quantities may vary as the tunable laser is swept across a resonant wavelength: the coupled power, the temperature of the resonator and surrounding medium, the refractive index of the resonator and surrounding medium, the mode structure, and the quality factor. Perhaps more interestingly, however, is the possibility that flow could be used to generate a scattering source efficient enough to break the degeneracy of the counter-propagating modes and yield a “split" resonance as seen in Fig. 3.11. These modes have been used to extract additional information about the scattering species, including particle size and number [96]. Some resonators feature imperfections that naturally cause this mode-splitting, but the use of careful flow patterns to create such a mode on demand could provide a more reliable means to explore how this sensing technique can be further applied.

Since any investigation of stagnation point flow effects on the adsorption profile of the analyte would mean sacrificing the convenient axial symmetry of the optical mode, continuing this work requires a full 3-dimensional description of the resonant light rather than the 2-dimensional version provided by the popular Oxborrow method [103]. All modeling results presented here have been calculated using COMSOL, a finite element analysis multiphysics program. Incorporating the binding equilibrium into such a model would be a relatively straightforward application of weak form surface reaction equations to describe the surface-bound species. The full 3-dimensional mode simulation is a task I am far less familiar with and may pose the greater challenge. Such a mathematical model would enable the investigation of the exact binding response, although including a heat transfer model to describe how temperature changes (turning the refractive index, now considered a material function solely of temperature, into a scalar variable of position as well) is so thoroughly complex that it may push the Flagan Laboratory’s computation server to its limits.

While using this model to explore the significance of experimental parameters like injection port size and position relative the resonator would be quite useful, a more realistic approach to these questions may be through simple experiments. This would be necessary to confirm the existence of scattering-induced change in Q as a result of stagnation point flow, and could also be used to determine how the sensor transient response would change if multiple injection ports were used to alter the traditional flow pattern. This flow pattern could help eliminate any change in Q due to scattering by hot or cold spots and would prove particularly useful when designing a flow cell for a WGM sensor instrument.

Optical Effects on Surface Reactions

For all sensor geometries, including the planar SPR sensor, one key assumption that is made when interpreting data or analyzing mass-transfer effects is that the affinity between the targeting species and the analyte is well approximated by the value measured for the freely diffusing species using other analytical methods and standard conditions. This assumption might be inaccurately applied to the WGM biosensor because of the unusually high electric fields to which these biomolecules are exposed when $Q > 10^7$ resonators are used and because of the temperature changes that may be occurring due to absorption. One or both of these factors could have significant effects on the apparent surface reaction rates, and I consider each here separately.

It is well established that nearly all materials exposed to a large gradient in electric field will experience what is referred to as an *optical gradient force.* This force results from the material's inherent ability to polarize in the presence of a field, which creates a dipole that may be thought of as two isolated charges. Each charge will experience equal and opposite force in the presence of a uniform electric field, however this is not the case when a gradient in the electric field $\Delta\mathbf{E}$ exists. The net force $\mathbf{F}$ on the dipole in this case can be expressed as

$$\mathbf{F} = \frac{1}{2}\alpha\nabla\mathbf{E}^2, \tag{7.1}$$

where α is the polarizability of the molecule or particle. In this way a material will always be pulled toward areas of greatest electric field strength, a feature exploited by optical micro- and nanomanipulation instruments called *optical tweezers* [157].

This force is relevant to how these WGM biosensors may be used to measure adsorption and desorption reaction rates because of the evanescent field that decays exponentially from the surface of the device. The gradient created by this decaying field provides a force attracting material to the surface, as has been demonstrate by Arnold et al. [106]. In that study, the authors were able to form an optical trap by capturing partially sulfonated polystyrene beads (particle radius $a = 375\,\text{nm}$) in the potential well that resulted from the attractive interaction of the optical gradient force and the repulsive interaction of the Coulombic force between the unfunctionalized silica resonator and particle, which each had a negative character in solution. These experiments were designed to demonstrate the existence of this phenomena, employing large particles to ensure that they would experience sufficient force to be trapped. WGM sensing experiments can use resonators with higher Q values (10^8 compared to the values of 1.5×10^6 as used in Ref. [106]) that produce larger gradients in the electric fields that scale as $|\nabla \mathbf{E}| \sim Q^{1/2}$, such that some microtoroidal WGM biosensors could generate optical gradient forces an order of magnitude stronger for a given species than those experienced using the spherical devices in Ref. [106].

In the presence of such an optical force, analyte molecules that are bound to the targeting species will find it particularly difficult to migrate away from the sensor. In fact, the vibrations due to thermal excitation of a molecule that typically lead to dissociation may no longer be isotropic, but would instead favor the bound state by virtue of the excluded (or, at least, less favorable) direction of motion. This effect could have implications on heat transfer, which occurs via molecular collision, and may lead to apparent thermal and mass diffusion coefficients that do not match their bulk values. Indeed, anecdotal evidence for role of the optical gradient force in WGM biosensing comes from a series of experiments performed in the laboratory of Professor Armani at the University of Southern California, conducted by graduate students Ce Shi and Maria Chistiakova [2].

In those experiments, a solution containing both dilute streptavidin protein as well as streptavidin-functionalized polystyrene nanoparticles (radius $a = 25\,\mathrm{nm}$) were exposed to a biotin-functionalized WGM resonator in buffer. The results for this two-species sensing experiment featured an unstable equilibrium in the surface adsorption reaction, which was replaced by a different equilibrium. The result resembled the response depicted in Fig. 7.2 and likely relates to the fact that the streptavidin diffuses much faster than these nanoparticles and likely coated much of the resonator at first, with the balance of the surface being covered with polystyrene nanoparticles. Over time, however, the streptavidin may have dissociated and diffused away while the PS nanoparticles were trapped at the surface by optical forces, essentially rendering their adsorption reaction irreversible. As the smaller streptavidin molecules relinquished their binding sites

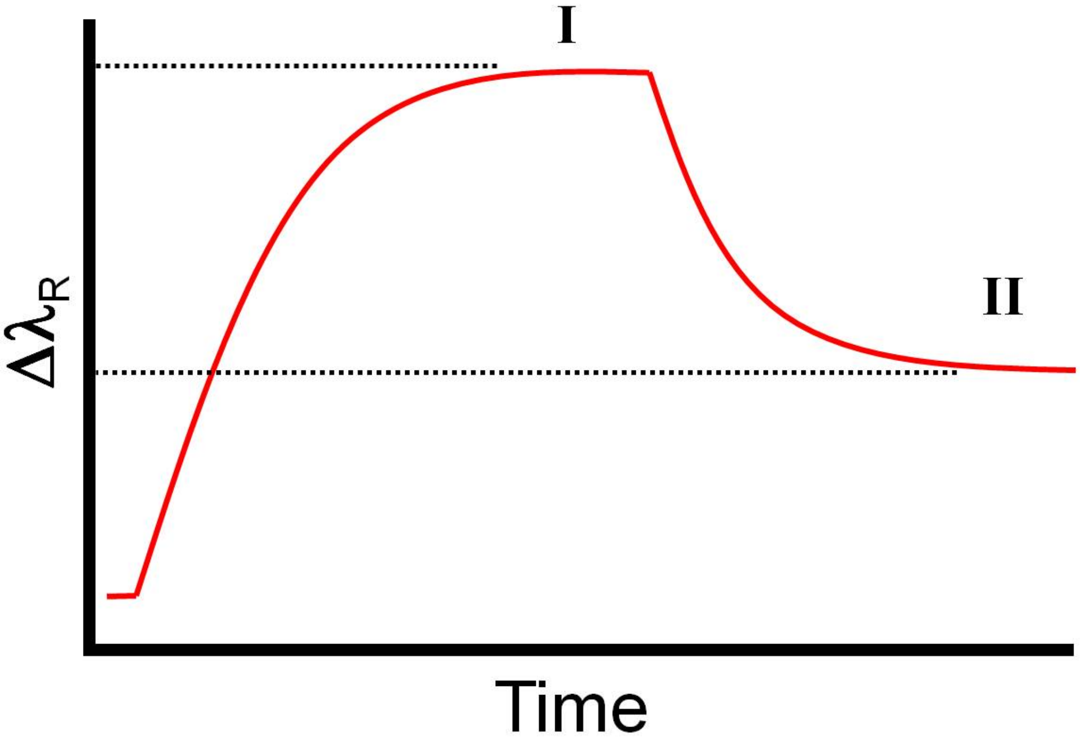

Figure 7.2: This graph shows how the WGM biosensor response appeared for detection of a mixture of streptavidin protein and streptavidin-coated polystyrene nanoparticles (radius a = 25nm) with a biotin-functionalized device. This is not actual data. Note the existence of two equilibria: the first (I) where the surface is populated with bound protein and nanoparticles, and the second (II) where the smaller streptavidin has dissociated and been mostly replaced by nanoparticles.

to the nanoparticles, a new equilibrium coverage may have been achieved that included almost entirely nanoparticles (some streptavidin molecules may have been "trapped" via steric effects).

As mentioned above, the second way in which the intense electromagnetic fields may affect the surface reaction between the analyte its targeting species it through absorption. There are a range of phenomena through which material on the surface may absorb or interact with light that lead to this material dissipating heat to its surroundings. We address some of these processes in earlier chapters, but as a brief review I will note that linear absorption, nonlinear absorption, two- and three-photon absorption, stimulated Raman scattering, and Brillouin scattering all introduce vibrational energy to a molecule that is converted locally into heat. Each process has a characteristic efficiency, and some of them are only relevant at extremely high optical powers. Regardless, the resonator itself as well as the surrounding medium (i.e., water) absorb sufficient light even at low coupled powers and moderate quality factors ($Q \gtrsim 10^5$) that nonlinearities occur during sensing experiments. This “thermal broadening" effect comes from the fact that power is increasingly coupled into the device during a sweep through wavelength space, warming the materials and inducing a concurrent resonance shift such that the sweep seems to be *chasing* the resonant wavelength and the dip trace acquired by the oscilloscope no longer has the symmetrical Lorentzian shape found in the absence of absorption.

The bulk warming provided by the the silica and water is enough to change the affinity of the analyte with its targeting species. The rate constant k_{rxn} used to describe a chemical reaction is a function of the temperature T, with most obeying an Arrhenius law where $k_{rxn} = Ae^{-\frac{E_a}{RT}}$ and A is a constant, E_a is the activation energy, and R is the gas constant. Warming a reaction typically drives it faster, although it is very difficult to determine *a priori* if the adsorption or the dissociation reaction will be affected more. Therefore, one can only say with certainty that the dissociation equilibrium coefficient K_D will be a function of temperature.

When species are present that absorb much more efficiently than their surrounding materials (i.e., water and silica), such as a an oligomeric protein, the pulses of heat may be sufficient for the molecule to breakdown either into its component pieces or at some weak bond. These events represent side reactions that may be irrelevant at standard laboratory temperatures that become significant when heat is injected locally and is unable to diffuse very quickly on the timescale of the pulse. Additionally, the specificity of the targeting species may change due to side reactions involving molecules structurally or chemically similar to the analyte that are present in the flow cell. What is certain, however, is that adding heat to the complex WGM sensing system can have any number of effects that must be taken into account when optimizing the application of this emerging tool.

Measuring the exact significance of these effects is difficult because they are coupled and would have overlapping effect. Increasing the coupled power to increase the optical gradient force would also increase the temperature of the materials. In order to observe the isolated importance of temperature, one could immobilize on the sensor (in addition to the targeting species) a species that absorbs very well at around

400-500 nm but does not exhibit any fluorescence. Most proteins absorb weakly at these wavelengths and therefore would not act as effective heat sources, so a specially designed fluorescence quencher molecule may be a good option. The trick would be to excite modes in the resonator with red *and* blue or green light simultaneously. The low-wavelength light would stimulate a heat source while the red light would be used to excite the resonance used for sensing. This is in lieu of using far-field illumination at the low wavelength because it would be difficult to get an exact measure of the amount of power actually getting to the quencher heat sources. Moreover, scanning the low-wavelength laser adds an additional variable which may be helpful to use while studying the effect of continuous or intermittent heating on the surface reaction. This experiment hinges upon the existence of a fiber-coupled laser at these wavelengths with moderate linewidth and the possibility of tuning. This should pose little challenge as New Focus is currently developing a Velocity$^{\mathrm{TM}}$ tunable laser with $< 500\,\mathrm{nm}$ wavelength.

Another interesting experiment to study the optical gradient force would be to vary the size of the nanoparticles at low coupled power in the under-coupled regime. By monitoring the frequency of dissociation events one may be able to establish a cutoff size at which optical gradient forces are relevant while minimizing variability in heat injected into the system via absorption. Alternatively, one could investigate the role of laser scan rate on optical gradient force and minimum particle size required for it to matter. Here it is helpful to remember that the optical gradient force is only applied while on or near resonance. As such, one critical threshold in this behavior may occur when the characteristic time it will take a particle to escape the evanescent field is equal to the time between pulses, or when

$$a \approx \frac{2k_BT(n_s^2 - n_m^2)}{3\lambda^2\nu\eta}, \tag{7.2}$$

where a is the particle radius, k_B is the Boltzmann constant, n_s is the sensor refractive index, n_m is the surrounding medium refractive index, ν is the frequency of scans (*not* the optical frequency), λ is the laser wavelength, and η is the viscosity of the medium through which the particle is moving. Using low coupled power and small scan scan frequencies (ν) assures that the heat may dissipate between scans and the effects can be attributed to the forces.

Improving Specificity Through Multi-Functional Sensors

Another interesting line of research would aim to improve the specificity of all immunoassay-based biosensors, including the WGM biosensor, by abandoning the paradigm of one antibody binding to one analyte. As noted in Chapter 2, antibodies are a very convenient targeting species because they are raised against a single target and can have K_D values as low as 10 pM. In neither commercial biochemical production methods nor in natural biology are antibodies typically selected for the ability to reject interactions with more than a few structural analogs of the analyte. An organism benefits from investing its energy into making antibodies that are sufficiently non-specific that they may be effectively useful more than one target. Additionally, even variation within a batch of a monoclonal antibody produced by a biochemical company will lead to a distribution of binding affinities for the intended antigen. This issue can be overcome to a small degree when a pharmaceutical company invests a great deal of research and care in the quality control of antibody-based therapeutic production, as required by FDA regulations. This level of care far surpasses that commonly found in non-therapeutic grade antibody, however.

It would be foolish to turn our backs on this convenient targeting species platform unless a simpler or less expensive one were already available. While there has been progress raising polymers capable of specific binding as well as designing hybrid architectures for combining targeting species with other materials to improve stability or affinity, these methods remain inadequate alternatives to the antibody-antigen specific sensing platform. Perhaps the most promising avenue for improving sensor specificity lies in the seemingly counterintuitive method of depositing a collection of targeting species, all with different affinities for any given analyte [158]. An array of sensors may then each present a different mixture (or at least mixtures with different constituent ratios) and much more information is available to identify the analyte or analytes present.

Such a mixture of targeting agents would present a signal identification challenge. No longer would the resonance shift of a given sensor be sufficient to determine the species, but rather the relative signal magnitudes from each sensor in the array. In essence, an analyte would interact with several different types of targeting species, but would generate a particular pattern of responses in the array that can serve as its fingerprint. This type of measurement is common for “artificial nose" sensors which often have far more limited specificity than the current immunoassay methods employed in WGM sensing. Of course, careful calibration must be done before any data can be extracted, and it may take a great deal of work to to establish a reliable platform based on a mixture of antibodies.

One way this surface-functionalization strategy might be simplified involves the use of hybridized, mutlivalent targeting species. It is well established that mutlivalency is a route to increasing the specificity of an interaction [158], as demonstrated by the frequency with which it occurs naturally on the cellular scale. Cholera toxin B, for example, is a hexamer where each of the five active subunits binds to an individual GM1 ganglioside in the cell membrane. The affinity of each of the five sequential binding interactions exceeds that of the last, such that the only way this protein can remain attached to the cell membrane long enough to undergo endocytosis (its goal) is if all subunits are bound. While an all-at-once, pentadentate binding event is exceedingly unlikely, it is assisted in part due to the freedom with which the gangliosides may diffuse in the cell membrane. The presence of “lipid rafts," or regions within the fluid cell membrane where mobility is locally decreased due to elevated concentrations of molecules like cholesterols, have been hypothesized to exist aid in multivalent interactions like this one by “herding" the receptors while still enabling them to diffuse locally.

The rational design of hybridized, multivalent targeting species as therapeutics has already been demonstrated [159, 160] and continues to be refined [161]. It remains to be seen whether one could create a multivalent molecule with different targeting species (of a controlled ratio) at each position, although such a molecule could serve as a precalibrated building block where using a mixture of different blocks could help tune specificity. Creating this heterogeneous multivalent targeting species requires a great deal of knowledge about the chemistry involved, but analysis of the data is well suited for a chemical engineer. This is especially true if the relative timescales of the various interactions between an analyte and the range of targeting species are dissimilar.

The concept of integrating an array of sensors, each with its own composition of targeting species, relies on two additional challenges being addressed. The first is that a multiplexed sensor must be fabricated, which has been demonstrated previously [162, 163, 164]. The current form of the WGM biosensor apparatus, in particular the use of a single, delicate tapered optical fiber waveguide for each resonator, precludes this kind of parallel scale-up. Devices with integrated waveguides must be developed for robustness and simplicity, and light used to excite WGMs must be split from a single laser source to make data processing more manageable.

Additionally, these devices must facilitate the second challenge, which is to fabricate a single microscale device with different regions (i.e., sensors) presenting different functionalities reliably. Unless identical distributions of targeting species can be deposited from one device to the next, prohibitively extensive calibration must be done for each. It would seem that laminar flow in a microfluidic channel (one channel for each device) may be used to deposit different surface chemistries in a suitable precise fashion (see Fig. 7.3), although the deposition of microdroplets of solution on individual sensors may also prove useful (assuming such a technique is possible through careful control of surface wettability)

Using flow or another mechanism to control the position of a surface reaction, characterizing that surface reaction as well as the one that occurs during specific sensing of biomolecules, and the rational design of reagents to enable parallel scale-up of a unit operation (sensor) represent challenges through which a chemical engineer may make significant contributions to the field of WGM sensing as well as sensing in general. I believe this work should begin with the two relatively simple steps of (i) functionalizing a chip, absent any sensors, wth different targeting species in different regions and (ii) covalently attaching a collection of antibodies raised against similar antigens in varying ratios to a WGM sensor to explore how the endpoint resonance shift may be used to surpass current specificity-related limitations.

Bridging Vapor- and Liquid-Phase Sensing Methods

The suggestions for future work I have already discussed add up to several doctoral theses worth of work, but one remains as a fascinating idea for the Flagan Lab, in particular, and merits inclusion here. Not only have WGM biosensors been demonstrated as tools useful for both liquid- and vapor-phase detection, but also

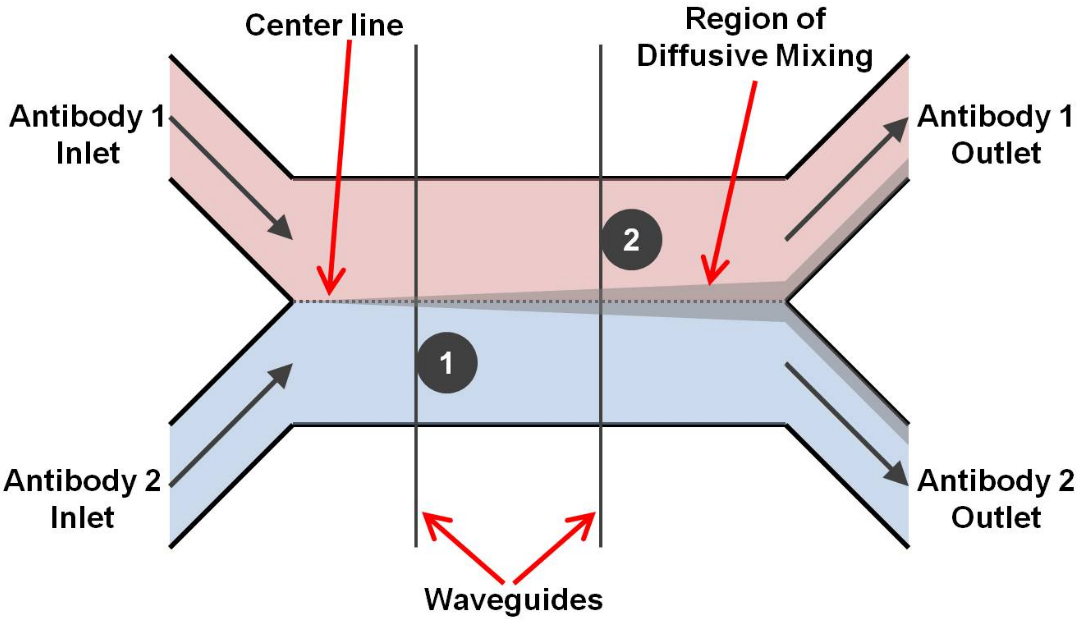

Figure 7.3: This microfluidic device diagram demonstrates how the laminar flow in such a device may be used to deposit different targeting species (referred to as *Antibody 1* and *Antibody 2*) on different sensors (labeled *1* and *2*) simultaneously. For sufficiently short channels, diffusive mixing between the adjacent flow paths will be limited to the small area indicated.

for aerosol sampling [96]. It is in this capacity that I believe WGM biosensors still have untapped potential. For the most part, aerosol particles are quite dilute in air and require filtration or impaction to capture and concentrate these particles for analysis. These techniques add additional steps to the process of isolating the aerosol species, which bring new opportunities for contamination. It would be preferable to just introduce the aerosol to the analytical tool directly, but it is difficult to get any information out of such a measurement due to the absence of a targeting species to isolate analytes of interest.

A new avenue of research into exacerbation of asthma by pollen has been to analyze the fragments of pollen that are present in the atmosphere that go unidentified using traditional pollen-count methods. It is believed that these species, much smaller than the whole pollen spores commonly considered, can make their way farther into the respiratory tract and, thus, interact with a part of the lungs that has been overlooked to date. Collaborators in Austria have successfully raised antibodies against some of these fragments and hope to apply these molecules to highly sensitive bioassays to quantify the level of pollen fragments in the air so that this data may be correlated to the instance of asthma attack. These fragments are present at sufficiently low concentrations that capturing them is only a part of the challenge; they must also be concentrated. However, WGM biosensors could be used, in conjunction with antibodies for specificity, to avoid these inefficient concentration steps if the fragments could be transferred from the air into liquid.

Other members of the Flagan Lab are already working on efficient means of vapor-liquid transfer for small aerosol particles, but a simple solution exists if only a single challenge could be overcome. One could imagine that a jet of ambient air impinging on a reservoir of liquid, within which resides a WGM biosensor, could transfer some of these particles directly into the effective “flow cell" surrounding the device. In order to minimize reservoir volume (increasing analyte concentration) and avoid evaporation of the liquid, measures must be taken to trap the liquid in the cell. I believe this may be accomplished by coating the devices with a hydrogel, a polymer structure often used as a biocompatible matrix known to serve this very purpose in tissue and biomoleculer engineering applications.

A hydrogel is usually cross-linked, with either a chemical or ultraviolet light serving as at the activator. A monomer may be spin-coated onto a chip of sensors, possibly functionalized as discussed above, and then cross-linked. The film thickness can be controlled through the spin-coating process and its chemical nature controlled through careful choice of monomer. In this way there will be a structure in place to keep a liquid layer surrounding the sensors even in the presence of impinging air, and this layer should still allow diffusion of analyte species now captured in liquid to diffuse to the sensors. An extra, sub-hydrogel reservoir of water or buffer may be necessary to ensure against drying, but this architecture would allow for a WGM biosensors strengths (specificity and sensitivity) to be exploited for the purpose of analyzing aerosol composition and concentration.

There also remains an issue to resolve concerning the observed kinetics and binding affinities between analyte and targeting molecule observed experimentally. As noted elsewhere, there exists an optical gradient force that acts to drive material toward regions of high electric field intensity [106]. This may be opposed or aided by Coulombic forces between surface charges on the resonator-bound targeting species, the resonator material itself, or because the analyte itself carries a charge in solution. This force has thus far only been observed in WGM sensors to affect large ($d_p > 100$ nm) nanoparticles, but its significance for protein-sized analytes ($d_p < 10$ nm) must still be determined. These forces can drastically affect the binding kinetics, as is clear in the limiting case where a purely attractive force on a protein both draws it toward the sensor more efficiently than diffusion and also keeps it from escaping if it dissociates from the analyte-target complex.

I consider these ideas as best suited for the engineering community to address, which is only beginning to work with WGM sensors. It is an entirely different (and exciting) game to imagine the purely scientific uses these tools may have. For example, I discuss during Chapter 5 how biophysical considerations may play a part in accurately describing heat transfer in the WGM sensing system. One could imagine looking at the role of hydrophobicity, both on the part of the analyte and the resonator surface, in creating a water environment that promotes or complicates energy transfer. Such an experiment could employ nanoparticles of varying surface chemistries or the use of established silane vapor deposition methods to control the sensor surface.

Additionally, one could explore the concept of molecular "heat" transfer by controlling the linkage between a nanoparticle tethered to the sensor surface. By varying the nature of the covalent linkage that tethers a nanopartcle to the resonator, the absorption coefficient of the nanoparticle material, and the WGM driving power, one may consider how vibrational energy is transmitted through different chemical structures. Along with the hydrophobicity experiments discussed above, this work would allow measurement of physical properties on a single-molecule level. Such quantities are masked during bulk, ensemble-averaged measurements, where distributions and variations in the property are lost.

Ultimately, my work contributes to an ongoing debate about the behavior of WGM sensors. Though the debate was, at times, less civilized than I would have imagined or hoped, I have enjoyed playing. There are many clever researchers already using WGM sensors, and I hope my work makes them more accessible and interesting to new ones.

Bibliography

[1] A. M. Armani, R. P. Kulkarni, S. E. Fraser, R. C. Flagan, and K. J. Vahala, Science **317**, 783 (2007).

[2] A. M. Armani, personal communication, personal communication, 2011.

[3] M. Janicka, A. Kot-Wasik, J. Kot, and J. Namiesnik, International Journal of Molecular Sciences **11**, 4631 (2010).

[4] D. Thevenot, K. Toth, R. Durst, and G. Wilson, Pure and Applied Chemistry **71**, 2333 (1999).

[5] F. Vollmer *et al.*, Applied Physics Letters **80**, 4057 (2002).

[6] S. Arnold, M. Khoshsima, I. Teraoka, S. Holler, and F. Vollmer, Optics Letters **28**, 272 (2003).

[7] D. C. Carter *et al.*, Science **244**, 1195 (1989).

[8] P. Harder, M. Grunze, R. Dahint, G. M. Whitesides, and P. E. Laibinis, The Journal of Physical Chemistry B **102**, 426 (1998).

[9] E. Ostuni, R. G. Chapman, R. E. Holmlin, S. Takayama, and G. M. Whitesides, Langmuir **17**, 5605 (2001).

[10] S. Choi and J. Chae, Journal of Micromechanics and Microengineering **20**, 075015 (2010).

[11] Z. Zhang, T. Chao, S. Chen, and S. Jiang, Langmuir **22**, 10072 (2006).

[12] H. Vaisocherová *et al.*, Analytical Chemistry **80**, 7894 (2008).

[13] N. D. Brault *et al.*, Biosensors and Bioelectronics **25**, 2276 (2010).

[14] K. A. Smith, Science **240**, 1169 (1988).

[15] L. He *et al.*, Journal of the American Chemical Society **122**, 9071 (2000).

[16] S. M. Nimjee, C. P. Rusconi, and B. A. Sullenger, Annual Review of Medicine **56**, 555 (2005).

[17] S. D. Jayasena, Clinical Chemistry **45**, 1628 (1999).

[18] S. Tombelli, A. Minunni, and A. Mascini, Biosensors & Bioelectronics **20**, 2424 (2005).

[19] R. Stoltenburg, C. Reinemann, and B. Strehlitz, Biomolecular Engineering **24**, 381 (2007).

[20] M. N. Win and C. D. Smolke, Proceedings of the National Academy of Sciences of the United States of America **104**, 14283 (2007).

[21] T. C. Chiu and C. C. Huang, Sensors **9**, 10356 (2009).

[22] N. Patel *et al.*, Langmuir **13**, 6485 (1997).

[23] N. K. Chaki and K. Vijayamohanan, Biosensors & Bioelectronics **17**, 1 (2002).

[24] H. K. Hunt, C. Soteropulos, and A. M. Armani, Sensors **10**, 9317 (2010).

[25] X. L. Sun, C. L. Stabler, C. S. Cazalis, and E. L. Chaikof, Bioconjugate Chemistry **17**, 52 (2006).

[26] J. Kalia and R. T. Raines, Current Organic Chemistry **14**, 138 (2010).

[27] A. Carrillo *et al.*, Nano Letters **3**, 1437 (2003).

[28] A. D. Stroock, R. S. Kane, M. Weck, S. J. Metallo, and G. M. Whitesides, Langmuir **19**, 2466 (2003).

[29] R. A. Vijayendran and D. E. Leckband, Analytical Chemistry **73**, 471 (2001).

[30] T. M. Squires and S. R. Quake, Rev. Mod. Phys. **77**, 977 (2005).

[31] H. Stone, A. Stroock, and A. Ajdari, Annual Review of Fluid Mechanics **36**, 381 (2004).

[32] H. Song and R. F. Ismagilov, Journal of the American Chemical Society **125**, 14613 (2003).

[33] F. Vollmer, S. Arnold, and D. Keng, Proceedings of the National Academy of Sciences of the United States of America **105**, 20701 (2008).

[34] D. Grieshaber, R. MacKenzie, J. Vörös, and E. Reimhult, Sensors **8**, 1400 (2008).

[35] K. Maehashi *et al.*, Analytical Chemistry **79**, 782 (2007).

[36] R. J. Chen *et al.*, Proceedings of the National Academy of Sciences of the United States of America **100**, 4984 (2003).

[37] A. Star, J.-C. P. Gabriel, K. Bradley, and G. Grüner, Nano Letters **3**, 459 (2003).

[38] J. Hahm and C. M. Lieber, Nano Letters **4**, 51 (2004).

[39] E. Stern *et al.*, Nature **445**, 519 (2007).

[40] F. Patolsky *et al.*, Proceedings of the National Academy of Sciences of the United States of America **101**, 14017 (2004).

[41] E. Stern *et al.*, Nano Letters **7**, 3405 (2007).

[42] E. Stern *et al.*, Nature Nanotechnology **5**, 138 (2010).

[43] C. Ziegler, Analytical and Bioanalytical Chemistry **379**, 946 (2004).

[44] G. Wu *et al.*, Nature Biotechnology **19**, 856 (2001).

[45] G. Shekhawat, S.-H. Tark, and V. P. Dravid, Science **311**, 1592 (2006).

[46] K. A. Marx, Biomacromolecules **4**, 1099 (2003).

[47] J. M. Perez, L. Josephson, T. O'Loughlin, D. Hogemann, and R. Weissleder, Nature Biotechnology **20**, 816 (2002).

[48] I. Koh and L. Josephson, Sensors **9**, 8130 (2009).

[49] D. R. Baselt *et al.*, Biosensors and Bioelectronics **13**, 731 (1998).

[50] D. L. Graham, H. A. Ferreira, and P. P. Freitas, Trends in Biotechnology **22**, 455 (2004).

[51] D. M. Jameson, J. C. Croney, and P. D. Moens, Fluorescence: Basic concepts, practical aspects, and some anecdotes, in *Biophotonics, Part A*, edited by I. P. Gerard Marriott, volume 360 of *Methods in Enzymology*, pp. 1 – 43, Academic Press, 2003.

[52] D. Axelrod, T. P. Burghardt, and N. L. Thompson, Annual Review of Biophysics and Bioengineering **13**, 247 (1984).

[53] D. A. Markov, K. Swinney, and D. J. Bornhop, Journal of the American Chemical Society **126**, 16659 (2004).

[54] D. J. Bornhop *et al.*, Science **317**, 1732 (2007).

[55] J. Homola, S. S. Yee, and G. Gauglitz, Sensors and Actuators B-Chemical **54**, 3 (1999).

[56] K. A. Willets and R. P. Van Duyne, Annual Review of Physical Chemistry **58**, 267 (2007).

[57] D. G. Myszka, X. He, M. Dembo, T. A. Morton, and B. Goldstein, Biophysical Journal **75**, 583 (1998).

[58] X. Yao *et al.*, Analytical Biochemistry **354**, 220 (2006).

[59] X. D. Fan *et al.*, Analytica Chimica Acta **620**, 8 (2008).

[60] A. B. Matsko and V. S. Ilchenko, IEEE Journal of Selected Topics in Quantum Electronics **12**, 3 (2006).

[61] V. S. Ilchenko and A. B. Matsko, IEEE Journal of Selected Topics in Quantum Electronics **12**, 15 (2006).

[62] S. H. Fan *et al.*, Physical Review B **59**, 15882 (1999).

[63] C. Manolatou *et al.*, IEEE Journal of Quantum Electronics **35**, 1322 (1999).

[64] V. S. Ilchenko *et al.*, Optics Communications **145**, 86 (1998).

[65] W. von Klitzing, R. Long, V. S. Ilchenko, J. Hare, and V. Lefevre-Seguin, Optics Letters **26**, 166 (2001).

[66] H. C. Tapalian, J. P. Laine, and P. A. Lane, Ieee Photonics Technology Letters **14**, 1118 (2002).

[67] C. G. Garrett, W. Kaiser, and W. Bond, Physical Review **124**, 1807 (1961).

[68] K. Srinivasan, P. E. Barclay, M. Borselli, and O. Painter, Physical Review B **70**, 081306 (2004).

[69] V. S. Ilchenko, A. A. Savchenkov, A. B. Matsko, and L. Maleki, Physical Review Letters **92**, 043903 (2004).

[70] D. W. Vernooy, A. Furusawa, N. P. Georgiades, V. S. Ilchenko, and H. J. Kimble, Physical Review A **57**, R2293 (1998).

[71] J. D. Suter, D. J. Howard, H. Shi, C. W. Caldwell, and X. Fan, Biosensors & Bioelectronics **26**, 1016 (2010).

[72] H. Zhu, P. S. Dale, C. W. Caldwell, and X. Fan, Analytical Chemistry **81**, 9858 (2009).

[73] J. T. Gohring and X. Fan, Sensors **10**, 5798 (2010).

[74] J. T. Gohring, P. S. Dale, and X. Fan, Sensors and Actuators B-Chemical **146**, 226 (2010).

[75] Rayleigh, Philosophical Magazine **20**, 1001 (1910).

[76] G. Mie, Annals of Physics **25**, 377 (1908).

[77] P. Debye, Annals of Physics **30**, 57 (1909).

[78] S. Spillane, *Fiber-coupled Ultra-high-Q MIcroresonators for Nonlinear and Quantum Optics*, PhD thesis, California Institute of Technology, 2004.

[79] B. Min, *Ultrahigh-Q Microtoroid On-Chip Resonators for Low Threshold Microlasers*, PhD thesis, California Institute of Technology, 2006.

[80] B. Min, L. Yang, and K. Vahala, Physical Review A **76** (2007).

[81] F. Vollmer and S. Arnold, Nature Methods **5**, 591 (2008).

[82] D. K. Armani, T. J. Kippenberg, S. M. Spillane, and K. J. Vahala, Nature **421**, 925 (2003).

[83] M. Gorodetsky, A. Savchenkov, and V. Ilchenko, Optics Letters **21**, 453 (1996).

[84] A. M. Armani, D. K. Armani, B. Min, K. J. Vahala, and S. M. Spillane, Applied Physics Letters **87** (2005).

[85] S. Arnold, R. Ramjit, D. Keng, V. Kolchenko, and I. Teraoka, Faraday Discussions **137**, 65 (2008).

[86] J. C. Knight, G. Cheung, F. Jacques, and T. A. Birks, Optics Letters **22**, 1129 (1997).

[87] V. S. Ilchenko, X. S. Yao, and L. Maleki, Optics Letters **24**, 723 (1999).

[88] M. Cai, O. Painter, and K. J. Vahala, Physical Review Letters **85**, 74 (2000).

[89] C. Bohren and D. Huffman, *Absorption and Scattering of Light by Small Particles* (WILEY-VCH, 2004).

[90] A. M. Armani, *Biological and Chemical Sensing with Ultra-High-Q Microcavities*, PhD thesis, California Institute of Technology, 2006.

[91] I. S. Grudinin, V. S. Ilchenko, and L. Maleki, Physical Review A **74** (2006).

[92] M. Hossein-Zadeh and K. J. Vahala, Optics Letters **32**, 1611 (2007).

[93] T. J. Kippenberg and K. J. Vahala, Optics Express **15**, 17172 (2007).

[94] T. J. Kippenberg and K. J. Vahala, Science **321**, 1172 (2008).

[95] I. Teraoka and S. Arnold, Journal of the Optical Society of America B-Optical Physics **26**, 1321 (2009).

[96] J. G. Zhu *et al.*, Nature Photonics **4**, 46 (2010).

[97] S. Arnold, S. I. Shopova, and S. Holler, Optics Express **18**, 281 (2010).

[98] T. M. Squires, R. J. Messinger, and S. R. Manalis, Nature Biotechnology **26**, 417 (2008).

[99] I. M. White, H. Oveys, and X. Fan, Opt. Lett. **31**, 1319 (2006).

[100] P. E. Sheehan and L. J. Whitman, Nano Letters **5**, 803 (2005).

[101] S. Friedlander, *Smoke, Dust and Haze* (John Wiley & Sons, 1977).

[102] V. G. Levich, *Physicochemical Hydrodynamics* (Prentice Hall, Inc., 1962).

[103] M. Oxborrow, IEEE Transactions on Microwave Theory and Techniques **55**, 1209 (2007).

[104] I. Lang, M. Scholz, and R. Peters, Journal of Cell Biology **102**, 1183 (1986).

[105] F. Vollmer and S. Arnold, Optical microcavities: Single virus detection and nanoparticle trapping, in *Proc. SPIE*, edited by R. M. and M. H., volume 7397 of *Biosensing II*, pp. 739702–1, 2009.

[106] S. Arnold *et al.*, Optics Express **17**, 6230 (2009).

[107] T. Lu *et al.*, Proceedings of the National Academy of Sciences of the United States of America **108**, 5976 (2011).

[108] A. Armani, *Photonic Microresonator Research and Applications*volume 156 of *Springer Series in Optical Sciences* (Springer, New York, 2010), chap. 11, p. 530.

[109] J. Zhu, c. S. K. Özdemir, L. He, D.-R. Chen, and L. Yang, Optics Express **19**, 16195 (2011).

[110] X. M. Zhang, H. S. Choi, and A. M. Armani, Applied Physics Letters **96**, 153304 (2010).

[111] I. Teraoka, S. Arnold, and F. Vollmer, Journal of the Optical Society of America B-Optical Physics **20**, 1937 (2003).

[112] J. M. Gamba and R. C. Flagan, Appl. Phys. Lett. **99**, 253705 (2011).

[113] V. S. Il'chenko and M. L. Gorodetskii, Laser Physics **2**, 1004 (1992).

[114] A. Gaiduk, M. Yorulmaz, P. V. Ruijgrok, and M. Orrit, Science **330**, 353 (2010).

[115] P. Kukura, M. Celebrano, A. Renn, and V. Sandoghdar, J. Phys. Chem. Lett. **1**, 3323 (2010).

[116] T. Carmon, L. Yang, and K. J. Vahala, Optics Express **12**, 4742 (2004).

[117] C. Liu, T. Kaiser, S. Lange, and G. Schweiger, Optics Communications **117**, 521 (1995).

[118] J. Jackson, *Classical Electrodynamics*, 2nd ed. (John Wiley & Sons, 1975).

[119] A. H. Zewail, Journal of Physical Chemistry A **104**, 5660 (2000).

[120] V. Sandoghdar *et al.*, Physical Review A **54**, R1777 (1996).

[121] B. Min *et al.*, Phys. Rev. A **70**, 033803 (2004).

[122] H.-S. Hsu, C. Cai, and A. M. Armani, Optics Express **17**, 23265 (2009).

[123] J. W. Perry *et al.*, Science **273**, 1533 (1996).

[124] G. de la Torre, P. Vázquez, F. Agulló-López, and T. Torres, Chemical Reviews **104**, 3723 (2004).

[125] B. LutherDavies and M. Samoc, Current Opinion In Solid State & Materials Science **2**, 213 (1997).

[126] P. Ormos *et al.*, Applied Physics Letters **80**, 4060 (2002).

[127] Y. Shen, Annual Review of Physical Chemistry **40**, 327 (1989).

[128] J. L. Dominguez-Juarez, G. Kozyreff, and J. Martorell, Nature Communications **2**, 254 (2011).

[129] H. Rokhsari and K. J. Vahala, Optics Letters **30**, 427 (2005).

[130] S. Sarupria and S. Garde, Phys. Rev. Lett. **103**, 037803 (2009).

[131] D. G. Cahill *et al.*, Journal of Applied Physics **93**, 793 (2003).

[132] C. Schmidt *et al.*, Applied Physics B: Lasers and Optics **104**, 503 (2011).

[133] C. Schmidt *et al.*, Optics Express **16**, 6285 (2008).

[134] H. Rokhsari, S. M. Spillane, and K. J. Vahala, Applied Physics Letters **85**, 3029 (2004).

[135] G. Abbate, U. Bernini, E. Ragozzino, and F. Somma, Journal of Physics D-Applied Physics **11**, 1167 (1978).

[136] T. Le, A. Savchenkov, N. Yu, L. Maleki, and W. H. Steier, Applied Optics **48**, 458 (2009).

[137] Comsol multiphysics 4.2 materials library, 2011.

[138] R. Pope and E. Fry, Appl. Opt. **36**, 8710 (1997).

[139] F-sv fiber specifications, newport corporation, 2011.

[140] G. Hale and M. Querry, Appl. Opt. **12**, 555 (1973).

[141] P. Montuschi, Therapeutic Advances in Respiratory Disease **1**, 5 (2007).

[142] S. Kazani and E. Israel, Journal of Breath Research **4**, 047001 (2010).

[143] P. Montuschi and P. J. Barnes, Journal of Allergy and Clinical Immunology **109**, 615 (2002).

[144] Z. Csoma *et al.*, American Journal of Respiratory and Critical Care Medicine **166**, 1345 (2002).

[145] S. Zanconato *et al.*, Journal of Allergy and Clinical Immunology **113**, 257 (2004).

[146] S. Balanza *et al.*, Journal of Investigational Allergology & Clinical Immunology **20**, 363 (2010).

[147] G. L. Milne, H. Yin, and J. D. Morrow, Journal of Biological Chemistry **283**, 15533 (2008).

[148] P. Montuschi *et al.*, American Journal of Respiratory and Critical Care Medicine **160**, 216 (1999).

[149] P. Montuschi *et al.*, Thorax **55**, 205 (2000).

[150] G. E. Carpagnano *et al.*, Chest **124**, 1386 (2003).

[151] M. Dietrich *et al.*, Cancer Epidemiology Biomarkers & Prevention **11**, 7 (2002).

[152] I. M. White, N. M. Hanumegowda, and X. D. Fan, Optics Letters **30**, 3189 (2005).

[153] E. Bucchioni, S. A. Kharitonov, L. Allegra, and P. J. Barnes, Respiratory Medicine **97**, 1299 (2003).

[154] N. Satyan, A. Vasilyev, G. Rakuljic, V. Leyva, and A. Yariv, Optics Express **17**, 15991 (2009).

[155] E. S. Hosseini, S. Yegnanarayanan, A. H. Atabaki, M. Soltani, and A. Adibi, Optics Express **17**, 14543 (2009).

[156] E. S. Hosseini, S. Yegnanarayanan, A. H. Atabaki, M. Soltani, and A. Adibi, Optics Express **18**, 2127 (2010).

[157] D. G. Grier, Nature **424**, 810 (2003).

[158] D. Vance, J. Martin, S. Patke, and R. S. Kane, Advanced Drug Delivery Reviews **61**, 931 (2009).

[159] A. Joshi, D. Vance, P. Rai, A. Thiyagarajan, and R. S. Kane, Chemistry-a European Journal **14**, 7738 (2008).

[160] A. Joshi *et al.*, Biomacromolecules **12**, 791 (2011).

[161] R. S. Kane, Langmuir **26**, 8636 (2010).

[162] G. F. Zheng, F. Patolsky, Y. Cui, W. U. Wang, and C. M. Lieber, Nature Biotechnology **23**, 1294 (2005).

[163] I. M. White, H. Oveys, X. Fan, T. L. Smith, and J. Y. Zhang, Applied Physics Letters **89** (2006).

[164] R. Fan *et al.*, Nature Biotechnology **26**, 1373 (2008).